Department of Electrical Engineering

Methodologies for development of series-hybrid powertrains to non-road mobile machineries

Matti Liukkonen

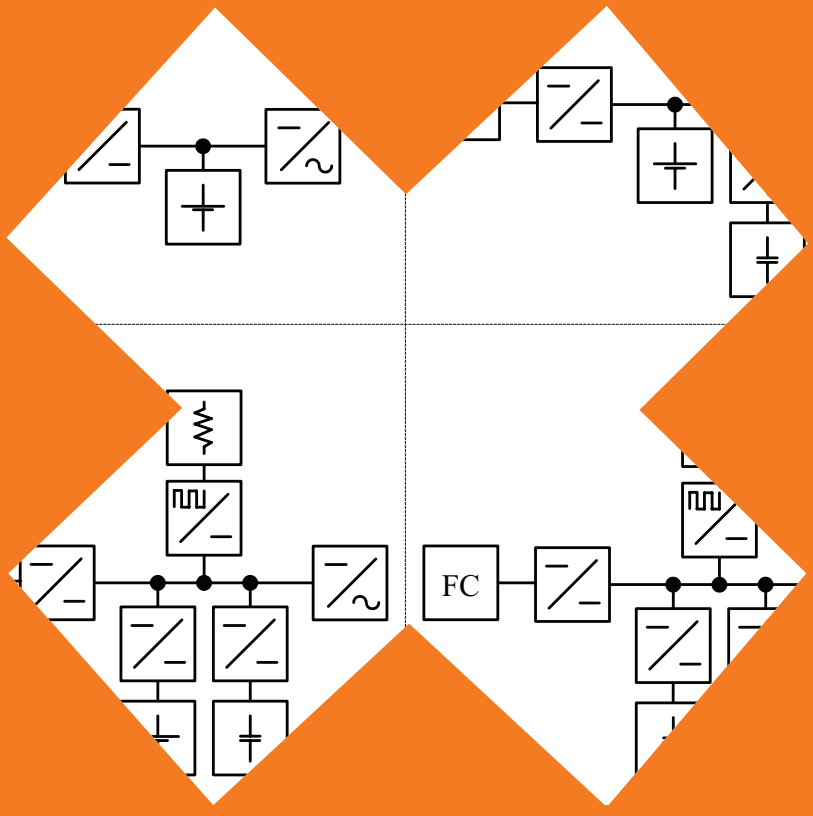

Aalto University

DOCTORAL DISSERTATIONS

Aalto University publication series
DOCTORAL DISSERTATIONS 157/2013

Methodologies for development of series-hybrid powertrains to non-road mobile machineries

Matti Liukkonen

A doctoral dissertation completed for the degree of Doctor of Science (Technology) to be defended, with the permission of the Aalto University School of Electrical Engineering, at a public examination held at the lecture hall S4 of the school on 13th of December 2013 at 12.30 o'clock.

Aalto University
School of Electrical Engineering
Department of Electrical Engineering

Supervising professor
Prof. Seppo J. Ovaska

Thesis advisor
Prof. (fixed term) Jussi Suomela

Preliminary examiners
Prof. Alain Bouscayrol, University Lille1, Villeneuve d'Ascq, France
Prof. Regan A. Zane, Utah State University, Logan, UT, United States

Opponent
Prof. Fei Wang, University of Tennessee, Knoxville, TN, United States

Aalto University publication series
DOCTORAL DISSERTATIONS 157/2013

ISBN 978-952-60-5366-0
ISBN 978-952-60-5365-3 (pdf)
ISSN-L 1799-4934
ISSN 1799-4934 (printed)
ISSN 1799-4942 (pdf)
http://urn.fi/URN:ISBN:978-952-60-5365-3

http://lib.tkk.fi/Diss/

Unigrafia Oy
Helsinki 2013

Finland

441 697
Printed matter

Author
Matti Liukkonen

Name of the doctoral dissertation
Methodologies for development of series-hybrid powertrains to non-road mobile machineries

Publisher School of Electrical Engineering

Unit Department of Electrical Engineering

Series Aalto University publication series DOCTORAL DISSERTATIONS 157/2013

Field of research Industrial Electronics and Electric Drives

Manuscript submitted 4 June 2013 **Date of the defence** 13 December 2013

Permission to publish granted (date) 11 September 2013 **Language** English

☐ **Monograph** ☒ **Article dissertation (summary + original articles)**

Abstract

This dissertation is about the assessment and development methodologies of series-hybrid powertrains to non-road mobile machineries. The development and optimization of alternative powertrains require computational methodologies for different fidelity levels in order to maintain manageability and effectiveness of analyses. This dissertation uses a multi-stage modeling approach for a large-signal analysis of system-level designs. A small-signal approach is proposed for the stability assessments of DC-buses in power-electronics systems.

The multi-stage modeling approach is used systematically for assessments of the diesel-electric powertrain with the power buffering by the active ultracapacitor. These assessments include design and validation of energy management algorithms for the powertrain. This energy management is described as the indirect power buffering, due to low-level controls of converters. The partial differential equations and the Monte Carlo method are used for error and sensitivity analyses of these assessments. Knowledge of achievable accuracies and restrictions of the multi-stage approach have been attained with experiments and assessments.

The multi-stage modeling approach is used for evaluations of feasibilities and features of powertrain options in a non-road mobile machinery case. Mutual relations of the features of powertrain options, such as size, weight, cost, and efficiency, are concluded. This knowledge is a base for the choice between powertrain options, and enables optimization of the powertrain with respect to a single feature. The significance of this approach is on the management of the complex entity, i.e., the design of complete series-hybrid powertrains.

A systematic approach for the dynamic modeling of DC-buses in power-electronics systems is introduced. This approach facilitates designs of load and source converter controllers in such a system. It can be used to derive the maximum lengths of the DC-bus cabling, as well as the minimum values and distribution of the DC-bus capacitances.

Keywords DC-bus systems, diesel electric, energy buffering, fuel cell, mobile work machine, modeling, powertrain design, series hybrid, ultracapacitor

ISBN (printed) 978-952-60-5366-0 **ISBN (pdf)** 978-952-60-5365-3

ISSN-L 1799-4934 **ISSN (printed)** 1799-4934 **ISSN (pdf)** 1799-4942

Location of publisher Espoo **Location of printing** Helsinki **Year** 2013

Pages 210 **urn** http://urn.fi/URN:ISBN:978-952-60-5365-3

Aalto-yliopisto

Tiivistelmä

Aalto-yliopisto, PL 11000, 00076 Aalto www.aalto.fi

Tekijä
Matti Liukkonen

Väitöskirjan nimi
Sarjahybridivoimansiirron kehittämismenetelmiä liikkuviin työkoneisiin

Julkaisija Sähkötekniikan korkeakoulu

Yksikkö Sähkötekniikan laitos

Sarja Aalto University publication series DOCTORAL DISSERTATIONS 157/2013

Tutkimusala Teollisuuselektroniikka ja sähkökäytöt

Käsikirjoituksen pvm 04.06.2013 **Väitöspäivä** 13.12.2013

Julkaisuluvan myöntämispäivä 11.09.2013 **Kieli** Englanti

☐ **Monografia** ☒ **Yhdistelmäväitöskirja (yhteenveto-osa + erillisartikkelit)**

Tiivistelmä

Tämä väitöskirja käsittelee liikkuvien työkoneiden sarjahybridivoimansiirron analysointi- ja kehittämismenetelmiä. Eritasoisia laskentamenetelmiä tarvitaan vaihtoehtoisten voimansiirtojen kehittämiseen ja optimointiin, jotta laskennan hallittavuus ja tehokkuus säilyisivät. Tämä väitöskirja esittelee moniasteisen mallinnusmenetelmän sarjahybridivoimansiirron järjestelmätason vaihtoehtojen analysointia ja kehittämistä varten, sekä hyödyntää menetelmää systemaattisesti. Lisäksi tässä väitöskirjassa ehdotetaan systemaattista lähestymistapaa tehoelektroniikkajärjestelmissä käytettyjen tasajänniteväylien stabiiliustarkasteluun.

Moniasteista mallinnusmenetelmää käytetään systemaattisesti aktiivisella ultrakondensaattorilla puskuroidun dieselsähköisen voimansiirron tarkasteluihin. Nämä tarkastelut koostuvat energianhallinta-algoritmien suunnittelusta ja toiminnan oikeellisuuden varmentamisesta mittauksilla. Laitetason säädinten valinnasta johtuen kyseistä energianhallintaa kuvataan tehon epäsuoraksi puskuroinniksi. Näiden tarkastelujen virhe- ja herkkyysarviointeihin käytetään osittaisdifferentiaaliyhtälöitä ja Monte Carlo -menetelmää, joilla analysoidaan teoreettisesti mallinnusmenetelmän tarkkuutta. Lisäksi vertailumittaukset lisäävät ymmärrystä mallinnusmenetelmän tarkkuudesta ja rajoitteista.

Väitöskirjassa käytetään moniasteista mallinnusmenetelmää myös liikkuvan työkoneen vaihtoehtoisten sarjahybridivoimansiirtojen ominaisuuksien määrittämiseksi. Keskinäiset suhteet eri voimansiirtoratkaisujen koolle, painolle, hinnalle ja hyötysuhteelle esitetään erään liikkuvan työkoneen tapauksessa. Tarkastelulla saavutettu tieto mahdollistaa valinnan eri voimansiirtoratkaisujen välillä ja siten myös voimansiirron yksittäisen ominaisuuden optimoinnin. Esitelty mallinnusmenetelmä auttaa monimutkaisen järjestelmän suunnittelussa.

Dynaaminen mallintaminen on oleellinen osa järjestelmien suunnittelussa. Sen vuoksi tässä väitöskirjassa ehdotetaan systemaattista lähestymistapaa tehoelektroniikkajärjestelmissä käytettyjen tasajänniteväylien stabiiliustarkasteluun. Kyseinen lähestymistapa helpottaa järjestelmän suuntaajien säädinten suunnittelua. Lähestymistapaa voidaan käyttää tasajänniteväylän kaapeleiden maksimipituuksien ja kapasitanssin suuruuden sekä jakautumisen määrittämiseksi.

Avainsanat dieselsähköinen, energian puskurointi, liikkuva työkone, mallintaminen, polttokenno, sarjahybridi, tasajänniteväylä, ultrakondensaattori, voimansiirron suunnittelu

ISBN (painettu) 978-952-60-5366-0 **ISBN (pdf)** 978-952-60-5365-3

ISSN-L 1799-4934 **ISSN (painettu)** 1799-4934 **ISSN (pdf)** 1799-4942

Julkaisupaikka Espoo **Painopaikka** Helsinki **Vuosi** 2013

Sivumäärä 210 **urn** http://urn.fi/URN:ISBN:978-952-60-5365-3

Preface

The series-hybrid electric vehicle powertrain research at Aalto University facilities started in the year 2002, with the demonstrator for the interest of industrial partners. My contribution to the topic started in the mid-2007, when the work continued with the development of the series-hybrid Hardware-in-the-Loop test environment. My research with powertrain components efficiency measurements, power control experiments, and modeling of system components, progressed from 2008 to 2009. Later on, my work focused on analyses of results, case studies, dynamic modeling, as well as introduction of my approaches to powertrain design.

I am truly grateful to Prof. Jorma Kyyrä for an opportunity to write my master's thesis in a hybridization project between 2007 and 2008, to Prof. Jussi Suomela for instructions and project leading between 2008 and 2012, and to Prof. Seppo J. Ovaska for guidance while finalizing this dissertation. I want to thank Prof. Marko Hinkkanen, Ari Hentunen, and Antti Lajunen for their contributions to my work as second authors, and special thanks to Jukka Halme for his interest in research in the same extensive topic. I would like to express my deep appreciation to Prof. Alain Bouscayrol and Prof. Regan A. Zane for their insightful comments and constructive criticism.

This dissertation is part of a bigger multi-disciplinary entity in hybridization projects of mobile machineries, and therefore the presented work would not be possible without help of various people. I thank my project colleagues Panu Sainio, Teemu Lehmuspelto, Antti Leivo, Matti Heiska, Perttu Heikkilä, Lauri Hintsala, Jarno Kukkola, and Ilkka Hanhivaara for their support and laboratory expertises. In addition, thanks to my office colleagues Tuomo Malkamäki, Seppo Saarakkala, Toni Tuovinen, Mikaela Ranta, and Zengcai Qu for the good working atmosphere.

This dissertation has been written during the 4-year position in the Doc-

toral Program of Electrical Energy Engineering (DPEEE) that is the principal sponsor of my work. Furthermore, part of the salary was obtained from the projects HybDrive, TopDrive, and ECV/Tubridi, and the Aalto ELEC Energy Programme. The major financiers for the projects were the Finnish Funding Agency for Technology and Innovations (Tekes), and the Multidisciplinary Institute of Digitalisation and Energy (MIDE) of Aalto University. In addition, grants given by the Fortum, Henry Ford, and Kansallis-Osake-Pankki foundations supported the research for this dissertation.

After all, writing of this dissertation would not have been possible without the support of my beloved wife Sara.

Espoo, October 2, 2013,

Matti Liukkonen

Contents

Preface vii

Contents ix

List of Publications xi

Author's Contribution xiii

List of Figures xvii

List of Tables xxi

Symbols and Abbreviations xxiii

1. Introduction 1

1.1 History 5

1.2 State of the Research 9

2. Modeling 29

2.1 Multi-stage Modeling of Series-Hybrid Powertrains 30

2.1.1 Test Setups 31

2.1.2 Basis of Plant Models 34

2.1.3 Electric Drive Plant Model 36

2.1.4 DC-DC Converter Plant Model 39

2.1.5 Ultracapacitor Pack Plant Model 43

2.1.6 Battery Pack Plant Model 45

2.1.7 Active Front-end Converter and Generator Plant Model 47

2.1.8 Diesel Engine Plant Model 49

2.1.9 Fuel Cell Source Plant Model 52

2.1.10 Brake Resistor and Chopper Plant Model 53

2.1.11 Energy Management Algorithm for the Hybrid Control Mode 54
2.2 Dynamic Modeling of Series-Hybrid Powertrains 59
2.2.1 Load and Source Models 59
2.2.2 Dynamic Ultracapacitor Models 61
2.2.3 Dynamic Battery Models 63
2.3 Error Analysis 66
2.3.1 Maximum Measurement Error 66
2.3.2 Monte Carlo Method 79
2.3.3 Monte Carlo Simulation 80
2.3.4 Global Sensitivity Indices 82
2.3.5 Results of Sensitivity Analysis 83

3. Summary of Publications **91**
3.1 Publication I 91
3.2 Publication II 92
3.3 Publication III 93
3.4 Publication IV 93
3.5 Publication V 94
3.6 Publication VI 94
3.7 Publication VII 95

4. Conclusions **97**
4.1 Main Results 97
4.2 Scientific Importance of Author's Work 99
4.3 Proposals for Future Work 101

Bibliography **103**

Errata **109**

Publications **111**

List of Publications

This thesis consists of an overview and of the following publications which are referred to in the text by their Roman numerals.

I J. Halme, M. Liukkonen, M. Heiska, and J. Suomela. Power bus control for series hybrid heavy-duty vehicles. *World Electric Vehicle J.*, 3(1), May 2009.

II M. Liukkonen, A. Hentunen, J. Suomela, and J. Kyyrä. Low-pass filtered power-flow control in series hybrid electric vehicle. In *Proc. 24th Elect. Veh. Symp.*, Stavanger, Norway, May 2009.

III M. Liukkonen, A. Hentunen, and J. Suomela. Validation of quasi-static series hybrid electric vehicle simulation model. In *Proc. IEEE Veh. Power and Propulsion Conf.'10*, Lille, France, Sept. 2010.

IV M. Liukkonen, A. Hentunen, and J. Suomela. Analysis of the ultracapacitor module in power buffering. In *Proc. 4th European Symp. on Super Capacitors and Applicat.*, Bordeaux, France, Oct. 2010.

V M. Liukkonen, A. Lajunen, and J. Suomela. Feasibility study of fuel cell-hybrid powertrains in non-road mobile machineries. *Automation in Construction*, 35(1):296-305, Nov. 2013.

VI M. Liukkonen and J. Suomela. Design of an energy management scheme for a series-hybrid powertrain. In *Proc. IEEE Transportation Electrification Conf. and Expo*, Dearborn, MI, June 2012.

VII M. Liukkonen, M. Hinkkanen, J. Kyyrä, and S. J. Ovaska. Modeling of multiport DC busses in power-electronic systems. In *Proc. IEEE Int. Conf. on Ind. Tech.*, pp. 740–745, Cape Town, South Africa, Feb. 2013.

Author's Contribution

Publication I: "Power bus control for series hybrid heavy-duty vehicles"

The first author Jukka Halme is the main contributor to this article. The work bases on a simulation environment developed by the second author Matti Liukkonen with contributions given to reactive control methods of the device layer, such as the combined voltage and load power control. Otherwise, this article is a result of the first and co-authors contributions to the HybDrive research project.

Publication II: "Low-pass filtered power-flow control in series hybrid electric vehicle"

The author developed plant models for an active ultracapacitor buffered diesel-electric series-hybrid powertrain, and based on these plant models he proposed an energy management for a charge-sustaining operation of the powertrain. The operation of the proposed energy management has been illustrated with time-domain simulations. The author compared effects of different configurations of an ultracapacitor energy storage to sizing of an engine and energy losses of energy storage. Co-authors Hentunen, Dr. Jussi Suomela, and Prof. Jorma Kyyrä have given their important feedback during the work and publishing phases of this paper.

Publication III: "Validation of quasi-static series hybrid electric vehicle simulation model"

The author implemented applicable parts of the designed energy management, in Publication II, to a Hardware-in-the-Loop environment that was configured to represent the active ultracapacitor buffered diesel-electric series-hybrid powertrain. The author performed all measurements and compared them to simulations, reviewed the energy management algorithm, and concluded that this algorithm is capable of all required operation modes of a series-hybrid powertrain. The author received help for measurements from laboratory assistants Lauri Hintsala and Perttu Heikkilä. The second and third authors, Ari Hentunen and Dr. Jussi Suomela, have given their important feedback during the work and publishing phases of this paper.

Publication IV: "Analysis of the ultracapacitor module in power buffering"

The paper is author's original idea to make a case study for two different energy management algorithms to illustrate their effect on the powertrain operation. The energy management algorithms were experimented in a common DC bus system with help of laboratory assistants Lauri Hintsala and Perttu Heikkilä. Furthermore, the author did efficiency measurements of an energy storage system, and derived efficiency maps for this system. The author is the only contributor of the case studies with the time-domain and operation area simulations. The second and third authors, Ari Hentunen and Dr. Jussi Suomela, have given their important feedback during the work and publishing phases of this paper.

Publication V: "Feasibility study of fuel cell-hybrid powertrains in non-road mobile machineries"

The feasibility case study based for the most part on contributions of the author. Case examples, as starting points, and objectives of this work were defined by the author with substantial help of the second and third authors, Antti Lajunen and Prof. Jussi Suomela. Furthermore, the second and third authors gave valuable advises in illustration and analysis of the results in a short and concise way.

Publication VI: "Design of an energy management scheme for a series-hybrid powertrain"

The paper is author's original idea to concentrate on a specific series-hybrid powertrain case, assessed in Publication V, in sense of the representation of an energy management and dimensioning of a powertrain with time-domain simulations. The paper solely bases on contributions of the author. The second author Prof. Jussi Suomela has given valuable feedback during the work and publishing phases of this paper.

Publication VII: "Modeling of multiport DC busses in power-electronic systems"

The author is the main contributor of this paper. The second author Prof. Marko Hinkkanen has given substantial help by providing his profound insight into dynamic modeling of electrical systems. Furthermore, Prof. Marko Hinkkanen provided dynamic modeling tools for assessments of this paper. The presented results base on the work done by the first and second authors. The third and fourth authors, Prof. Jorma Kyyrä and Prof. Seppo J. Ovaska, have given their valuable feedback during the work and publishing phases.

List of Figures

1.1 Different non-road mobile machineries; (a) harbor straddle carrier, (b) mine loader, and (c) forwarder. 1
1.2 Component options for different series-hybrid electric vehicle powertrains. 5
1.3 Powertrain with an engine generator-set, active rectifier, and passive battery pack. 11
1.4 Powertrain with an engine generator-set, active rectifier, and active battery pack. 12
1.5 Powertrain with an engine generator-set, active rectifier, and active ultracapacitor pack. 13
1.6 Powertrain with an engine generator-set, active rectifier, passive battery, and active ultracapacitor pack. 14
1.7 Powertrain with an engine generator-set, passive rectifier, and active ultracapacitor pack. 15
1.8 Different fuel cell source powertrain cases; (a) the powertrain with a passively coupled FC source and passive ES, (b) the powertrain with a passively coupled FC source and active ES, and (c) the powertrain with an actively coupled FC source and active ES. 16
1.9 (a) Powertrain with an actively coupled FC source, active battery, and active UC, (b) the powertrain with a passively coupled FC source, and active ESs in two different DC-buses, and (c) the powertrain with a passively coupled FC source, active battery, and active UC. For the sake of simplicity, possible brake units have been left out of the Figure. 20

2.1 Active UC buffered diesel-electric powertrain. Powertrain variables and principles of plant models. 30

2.2 Active battery and UC pack buffered powertrain with the fuel cell source. Powertrain variables. The abbreviation *Eqs.* within the battery pack refers to equations 2.23...2.24. 31
2.3 Test setup for the DC-DC converter and ultracapacitor module identification. 31
2.4 Test setup for identification of the plant model of the variable speed diesel generator-set. 32
2.5 Hardware-in-the-Loop test setup for validations of plant models of the DC-DC converter and ultracapacitor module. . . . 33
2.6 Validation tests; (a) i_{uc} of a DC-DC converter model, and (b) u_{uc} of UC models. 33
2.7 Full Hardware-in-the-Loop test setup for an active UC buffered diesel-electric powertrain 34
2.8 Interfaces of main blocks of a multi-stage series-hybrid powertrain simulation environment. ED = electric drive, C = capacitance of a DC bus, DC/DC = DC-DC converter, UC = ultracapacitor, BAT = battery, AFE = active front-end, VSDG = variable speed diesel generator-set, FC = fuel cell, BRK = braking-unit. Variables are explained in following sections. 36
2.9 Top level of a multi-stage modeling approach for the powertrain with an engine generator-set, active rectifier, and active ultracapacitor pack. A point of common coupling is referred with PCC. Variables are explained in following sections. 37
2.10 Combined measured efficiency map of Siemens *ELFA 1PV51-35-4WS28* traction electric machine and *G650 D44/170/170 M7-1* inverter. 37
2.11 Efficiency map of a DC-DC converter in the charge operation. 40
2.12 Comparison of the first-order response behavior to the PI-controlled response. 41
2.13 AFE converter PI-regulator sign changes if i_{ES} is overcompensated. 43
2.14 Simple ultracapacitor model with either: (a) constant; or (b) variable capacitance and constant series resistance. 44
2.15 Two-quadrant efficiency map of ESS consisting of a DC-DC converter and UC module. 45

2.16 Torque data as a mapping of fuel quantity and speed of the engine. 51
2.17 Energy management hierarchy of the series-hybrid powertrain with the ultracapacitor pack for power buffering. . . . 54
2.18 Static ES system current reference $i_{\mathrm{ES}'}$ space presented in five piecewise charts with all inputs. 56
2.19 Operation points of an engine in the variable speed use on the fuel consumption map. Operation points are marked with stars, and the maximum power limit with a wide line. 57
2.20 Operation principle of an engine with the proposed rule-based speed control. 58
2.21 (a) Simple series-RC model, (b) impedance model, (c) parallel-RC branches model, (d) RC-transmission line model. 62
2.22 (a) Thevenin, (b) impedance-based electric circuit battery models. 64
2.23 Error paths of the model-based design for the diesel-electric powertrain with an active UC buffering. 73
2.24 Normal distribution where each band has width of the standard deviation. The midpoint of the x-axis is on the mean of a variable. 82
2.25 Illustration of the deviations in the power variables depending on an operation point of the powertrain with random changes in input parameters. 87
2.26 Illustration of the deviations in the current variables depending on an operation point of the powertrain with random changes in input parameters. 88
2.27 Illustration of the deviations in the miscellaneous variables depending on an operation point of the powertrain with random changes in input parameters. Variables beginning from the top: u_{DC}, τ_{load}, u_{uc}, n_{VSDG}, and $\dot{m}_{\mathrm{VSDG}}$. 88

List of Tables

2.1 Parameters for the comparison of responses. 40
2.2 Coefficients for the surface polynomial function of torque data 52
2.3 Voltage measurement maximum errors in different operation points. 67
2.4 Efficiency measurement maximum errors in different operation points. 67
2.5 Polynomial fittings for the efficiency surface within u_{ratio} of 0.07 ... 0.59. 68
2.6 Polynomial fittings for the efficiency surface within u_{ratio} of 0.3 ... 0.59. 69
2.7 Measurement sensor accuracies for the efficiency mapping of an electric drive. 70
2.8 Efficiency mapping accuracies of an electric drive with low and high speeds, and motoring and regenerative powers. . . 71
2.9 Accuracy of p_{LOAD} when the starting point of modeling is mechanical power. 72
2.10 Accuracies of the energy storage current. 76
2.11 Energy storage system current Δi_{ES} and AFE converter current Δi_{AFE} accuracies on the intermediate circuit. 76
2.12 Efficiency mapping accuracies of the generator electric drive in considered operations points. 78
2.13 Deterministic parameters for realization of the sensitivity analysis. 84
2.14 Sensitivity analysis results for powers. Standard deviations and first order Sobol indices. 85
2.15 Sensitivity analysis results for currents. Standard deviations and first order Sobol indices. 85

2.16 Sensitivity analysis results for miscellaneous variables. Standard deviations and first order Sobol indices. 86

Symbols and Abbreviations

Symbols

In general, the electrical variables with subscripts written in upper case refer to the quantities on the DC-link voltage potential and subscripts written with lower case refer to the quantities on voltage potential of the energy storage, respectively.

A	Battery exponential voltage
B	Battery exponential capacity
C	Battery nominal current
C_{DC}	Constant capacitance of a DC link
C_{uc}	Constant capacitance of an ultracapacitor pack
$\mathbf{C}_{\mathrm{uc}}$	Variable capacitance map of an ultracapacitor pack
D	Current direction for a DC-DC converter
e_{n}	Speed error term of a proportional-integral controller
e_{u}	Voltage error term of a proportional-integral controller
E_{bat}	Battery pack energy content
$E_{\mathrm{losses\_}i}$	Energy losses of a component i
E_{uc}	Ultracapacitor pack energy content
i_{AFE}	Direct current of an active front-end converter
i_{bat}	Battery current
i_{BRK}	Brake unit current

i_{es}	Energy storage current
i_{ES}	Energy storage current on potential of the DC-link voltage
$i_{\mathrm{ES}'}$	Energy storage system current reference on potential of the DC-link voltage
i_{fc}	Fuel cell current
i_{LOAD}	Load current on a DC link
i_{ref}	Current reference
$i_{\mathrm{ref}'}$	Current reference before limitations
$i_{\lvert\mathrm{ref}\rvert}$	Absolute current reference
it	Battery extracted capacity
i_{uc}	Ultracapacitor pack current
i^*	Battery low-frequency current dynamics
$i_{\sum \mathrm{PCC}}$	Sum current on a point of common coupling
I_{max}	Maximum current of a DC-DC converter
I_{min}	Minimum current of a DC-DC converter
J_{tot}	Total inertia on engine shaft
K_{I}	Integral coefficient of a proportional-integral controller
K_{P}	Proportional coefficient of a proportional-integral controller
$\dot{m}$	Engine fuel quantity in milligrams per stroke
n_{EM}	Electric machine speed
$n_{\mathrm{e\_ref}}$	Engine speed reference
n_{G}	Generator speed
n_{VSDG}	Engine speed
p_{ij}	Surface polynomial coefficient
p_{LOAD}	Load power, electrical
p_{mech}	Load power, mechanical
p_{ref}	Load power reference
P_{MAX}	Tuning parameter of an energy management algorithm
Q	Battery maximum capacity
R_{bat}	Battery resistance
R_{DC}	Equivalent series resistance of DC-link capacitors

R_{uc}	Equivalent series resistance of an ultracapacitor pack
t_{k}	Discrete-time sample with an index k
u_{bat}	Battery nonlinear output voltage
u_{DC}	DC-link voltage
$u_{\mathrm{DC\_ref}}$	DC-link voltage reference
u_{es}	Energy storage voltage
u_{fc}	Fuel cell source output voltage
u_{ratio}	Voltage conversion ratio, the energy storage voltage in contrast to the DC-link voltage
u_{uc}	Ultracapacitor pack voltage
U_0	Maximum voltage value of a battery in the linear area
U_{max}	Ultracapacitor maximum voltage
U_{nom}	Minimum voltage value of a battery in the linear area
$\bar{y}$ or μ	Mean of a variable
$\eta(i_{\mathrm{es}}, u_{\mathrm{ratio}})$	Efficiency map of a DC-DC converter
$\eta(n_{\mathrm{G}}, \boldsymbol{\tau_{\mathrm{req}}})$	Combined efficiency map of an active front-end converter and generator
η_{boost}	Efficiency map of a DC-DC converter in a discharge operation mode
η_{buck}	Efficiency map of a DC-DC converter in a charge operation mode
$\eta_{\mathrm{ED}}(n_{\mathrm{EM}}, \boldsymbol{\tau_{\mathrm{EM}}})$	Efficiency map of an electric drive
τ_{AFE}	Control delay time-constant of an active front-end converter
$\tau_{\mathrm{DC/DC}}$	Control delay time-constant of a DC-DC converter
τ_{e}	Control delay time-constant of a diesel engine
$\boldsymbol{\tau_{\mathrm{e}}}$	Output torque of a diesel engine
$\boldsymbol{\tau_{\mathrm{EM}}}$	Torque of an electric machine
$\boldsymbol{\tau_{\mathrm{load}}}$	Load torque of a diesel engine
$\boldsymbol{\tau_{\mathrm{map}}}$	Torque data mapping of a diesel engine
$\boldsymbol{\tau_{\mathrm{req}}}$	Generator requested torque
ω_{G}	Generator angular speed
ω_{VSDG}	Engine angular speed

Abbreviations

AC/DC	AC to DC rectifier
AFE	Active Front-End converter
AOC	Adaptive Optimal-Control
CO_2	Carbon dioxide
DC/AC	DC to AC inverter
DC/DC	DC to DC converter
ED	Electric Drive
EM	Electric Machine
EMS	Energy Management Strategy
ES	Energy Storage
ESS	Energy Storage System
EUT	Equipment Under Test
FC	Fuel Cell
G	Generator
HE	High Energy
HP	High Power
ICE	Internal Combustion Engine
IGBT	Insulated Gate Bipolar Transistor
MABX	dSpace MicroAutoBox
MPC	Model Predictive Control
NRMM	Non-Road Mobile Machinery
OEM	Original Equipment Manufacturer
PE	Power Electronics
PEM	Polymer Electrolyte Membrane or Proton Exchange Membrane fuel cell
PI	Proportional-Integral controller
QSS	Quasi-Static Simulation
SHEV	Series Hybrid Electric Vehicle
UC	Ultracapacitor
VSDG	Variable Speed Diesel Generator-set

1. Introduction

Non-road mobile machineries (NRMMs) are vehicles whose aim is to produce effective work in mobile positions. This category includes devices such as, harbor straddle carriers; mine loaders; forest work machineries, for instance, harvesters and forwarders; and military vehicles. Complementary terms for an NRMM are an off-road heavy vehicle [Chan et al., 2010; Ehsani et al., 2007], or even a heavy-duty vehicle [v. Walwijk, 2009]. The powertrain, which is the focus of this research, functions as a part of NRMMs.

Thus, a powertrain refers to the part of a vehicle that generates power and provides a path for power from the source to its load. In general, a powertrain may consist of various different components, due to the diverse purposes of NRMMs as illustrated in example Fig. 1.1. A harbor straddle carrier is used to lift, move, and descend containers in a harbor area. An underground mining loader charges a bucket at the end of an underground mine and hauls ore to a point from where an underground truck carries ore the rest of the way up. A forwarder collects logs with a boom and delivers logs next to the road from where a truck is able to pick up logs for road transportation.

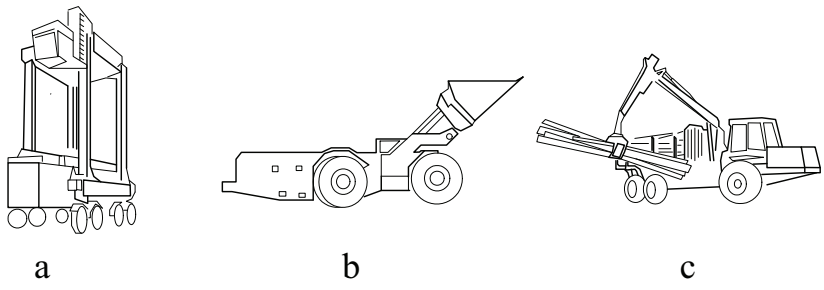

Figure 1.1. Different non-road mobile machineries; (a) harbor straddle carrier, (b) mine loader, and (c) forwarder.

The powertrain, for instance in a passenger car, consists of an internal

combustion engine (ICE), a gearbox, driveshafts, and differentials. In this vehicle, the ICE operates as a source, and the wheels operate as loads. Another example of powertrain design can be found in a diesel-electric train, which consists of an ICE, generator, rectifier, inverters, and traction machines. This type of a powertrain transforms rotational movement into an electric current and back to rotational movements. The third example of powertrain design is hydraulic, which is usually operated in hydrostatic means. In that powertrain, the ICE rotates a hydraulic generator that in turn is connected via hydraulic hoses to hydraulic motors. In such cases, the fluid pressure of the hoses is kept constant. Furthermore, this dissertation uses the word "powertrain" as described in the context of these three aforementioned examples. Synonyms are used to denote the powertrain [Chan et al., 2010; Ehsani et al., 2007], such as drivetrain [Ehsani et al., 2007; v. Walwijk, 2009; Chan, 2007], driveline, and transmission.

In the conventional car powertrain, the ICE operates as a source, and the wheels to the environment contacts operate as loads. Thus, a two-wheel drive has two bodies that create a load for the ICE, and a four-wheel drive has four. The ICE usually couples mechanically to loads and, thus, always operates at a speed defined by a vehicle speed and a gear ratio. In practice, loads define the torque and speed of the ICE and therefore, it cannot be operated in the best efficiency operation area. Moreover, the ICE cannot absorb more regenerative power than the parasitic loads on the ICE shaft consume, and therefore, during deceleration the kinetic energy from the vehicle body is consumed as heat in the brakes. On the other hand, some trains and ships have adopted the diesel-electric powertrain that relieves the ICE from the mechanical speed of a load. Furthermore, in trains the diesel-electric powertrain is needed if the railway line is lacking power lines. Such high cost high power applications as these have conventionally used electric powertrains. However, the diesel-electric powertrain cannot provide regenerative energy recuperation, although electric traction machines and inverters could provide such an operation. In practice, the diesel-electric powertrain only lacks a suitable energy storage system (ESS).

In comparison to cars, heavy-duty vehicle powertrains are more diverse. Besides the need for kinetic energy, heavy-duty vehicles often need linear movement for actuators, such as, buckets, hoists, and booms, which are usually operated with hydraulic cylinders. The movements and payloads of hydraulic actuators yield another load for the ICE, and may demand

high peak powers. Conventionally, hydraulic actuators have introduced partly or fully hydrostatic power transfer to the powertrain of a heavy-duty vehicle. The hydrostatic power transfer has traditionally had low overall energy efficiency that is in the range of less than 10 % due to partial loading of an ICE with high constant speed. Furthermore, in conventional designs, the hydraulic transmission has transferred power in only one direction, thus preventing regenerative energy recuperation.

Heavy-duty vehicles are a diverse group as described earlier. Trucks, cranes, tractors, bucket loaders, and trains among others can be included in this category. These vehicles are operated only on bounded sites, and thus called as non-road mobile machineries.[1] There is an enormous diversity and complexity in powertrains of NRMMs with respect to road vehicles. For instance, powertrains of NRMMs differ from road vehicles by their dimensions, power requirements, production amounts, emission regulations, and permanence of environmental conditions. Traditionally, NRMMs have been built with a mechanical, hydraulic, or diesel-electric powertrain. The conventional designs of NRMM powertrains have not usually enabled regenerative energy recuperation, which is available in most NRMM work cycles as kinetic and potential energy forms. In the traditional design, regenerative energy has been converted into heat in mechanical brakes, hydraulic valves or in brake resistors. Moreover, system efficiency is low during engine idling, i.e. partial loading of an ICE. These reasons lead to low overall energy efficiency in a system. For instance, the corresponding system efficiency in a conventional passenger car application is in the range of 14...22 %, and with a hybridized system 29...30 %, respectively [Åhman, 2001]. Furthermore, through hybridization, low emission by-production in power generation, and lower or even locally zero-emission powertrains can be successfully achieved [v. Walwijk, 2009]. Therefore, different hybrid powertrain topologies are studied for the regenerative energy recuperation of the NRMM powertrain.

A hybrid vehicle powertrain can be realized in many different ways. In general, different combinations of mechanical, hydraulic and electrical power transfer components may come into question for the right choice

[1] According to Directive 97/68/EC. Non-road mobile machinery: any mobile machine, transportable industrial equipment or vehicle with or without body work, not intended for the use of passenger- or goods-transport on the road, in which an internal combustion engine is installed. [Online]. http://ec.europa.eu/enterprise/sectors/mechanical/non-road-mobile-machinery/index_en.htm (Last accessed on 23th of Sept. 2013)

of the drivetrain topology for a specific case. For example, series, parallel, series-parallel, and complex hybrid electric vehicle architectures have been defined in [Chan, 2007]. However, feasible powertrain topology choices are predefined based on the application field, and thus, the study for hybridizing a powertrain in the NRMM concentrates on the series-hybrid electric vehicle (SHEV) topology [Chan et al., 2010; Ehsani et al., 2007].

This series-hybrid electric powertrain can consist of several different energy sources and storages see Fig. 1.2. These energy sources usually are engine and fuel cell, whereas the usual energy storage options are battery, ultracapacitor, and flywheel [Burke, 2007]. Additionally, the driveline demands controllable electric power conversions with power electronics devices. Such devices change the form of the current from alternate to direct, and vice versa, for the use of generator and electric machine. DC-DC converters control electric power through different voltage levels in the driveline, for the utilization of energy storage full capacity [Lai and Nelson, 2007]. The amount of options for the design of a hybrid driveline makes it an undoubtedly complex process. The degrees of freedom in design arise because of several energy storage options and their combinations, the sizing of energy sources and storages, the energy source and storage interface options, e.g. active or passive, and the control of active interfaces. Thus, feasibilities and design procedures of series hybrid powertrains are studied for the needs of NRMM manufacturer product development [Gao et al., 2007]. The importance of the study arises—specifically, due to the complexity of the subject, implementation of a new design, lack of already known design principles, and the education of new engineers. Therefore, efficient modeling principles for the NRMM powertrain design are considered in this research.

Thus, this study concentrates on the series-hybrid electric powertrain, which has all system loads connected to the common DC-bus. In other words, all system loads are treated as one load that is consumed from the common DC-bus. This simplification neglects the realization of the load, since this would lead to an overly diverse research area.

As a summary, the goal of this dissertation is to provide design knowledge, and tools for development of series-hybrid powertrains in NRMM applications. In some NRMM applications, conventional powertrains need to be re-designed due to low-energy efficiency, and lack of regenerative energy recuperation. As design options, there exist various types of pow-

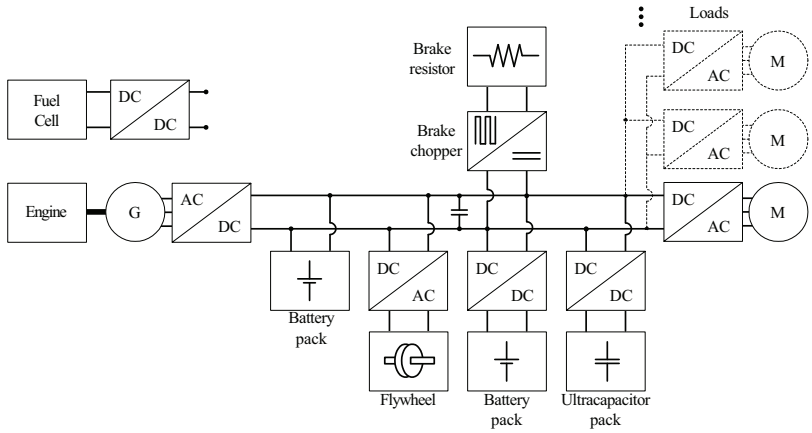

Figure 1.2. Component options for different series-hybrid electric vehicle powertrains.

ertrains, as different types of hybrids, and as different types of series-hybrids which are discussed in Section 1.2. In practice, the engineer should be capable of choosing the right powertrain for a specific application. Therefore, contributions have been made in order to reach previous common goals.

This dissertation is organized as follows: Chapter 1 defines the background and scope, and previews the history as well as the state of the research of the topic; Chapter 2 describes used modeling methods and assesses maximum measurement errors and parameter sensitivities with the Monte Carlo method; Chapter 3 summarizes publications; and Chapter 4 concludes this dissertation.

The publications included in this dissertation are reprinted at the end.

1.1 History

Development Milestones of an Early Electric Vehicle

The invention of the electric vehicle has been attributed to various people from the 1820s to 1900s. Named contributions began with Ányos Jedelik in 1828, who demonstrated an early type of electric motor. After several other contributions, in 1881, French inventor Gustave Trouvé demonstrated a working three-wheeled automobile at the International Exhibition of Electricity in Paris, which was powered by 0.1 horsepower DC motor and weighted 160 kg.

The 1890s was an era of rapid development of an electric vehicle. The first commercially successful electric car, able to carry six passengers at

16 km/h, was made in 1893 by Paul Pouchain. Later, Camille Jenatzy broke the 100 km/h speed barrier with an electric vehicle in 1899 for the first time. Development was rapid due to a series of competitions that promoted technical improvements.

The first hybrid vehicles reported were shown at the Paris Salon in 1899 with a presentation of parallel and series-hybrid concepts. The series-hybrid based on a pure electric vehicle, and built by the French firm Vendovelli and Priestly.

During 1900...1910, electric cars reached the height of their success, and manufacturing amounts peaked in the United States by 1912. While gasoline automobiles became more powerful, more flexible, and above all easier to handle—electric vehicles started to disappear. Their high cost, limited range and performance impaired them against the gasoline vehicles. In nearly 60 years, the only electric vehicles sold were forklifts, delivery vehicles, and golf carts. [Guarnieri, 2011a,b; Wakefield, 1994] and [Ehsani et al., 2005, pp. 13-19]

Fuel Cell

Sir William Grove, who discovered that it might be possible to generate electricity by reversing the electrolysis of water, made the first contributions for the fuel cell invention as early as 1839. It took until 1889 before the term "fuel cell" came into use while Charles Langer and Ludwig Mond tried to engineer the first practical fuel cell using air and coal gas.

It was remarkably later, in the 1950s, that Francis Bacon successfully produced the first practical alkaline fuel cell. In the 1960s, an alkaline fuel cell power plant was developed for the Apollo spacecraft. The plant provided both electricity (1.5 kW) as well as drinking water for the astronauts on their journey to the moon. A drawback in previous fuel cells was that carbon dioxide would react with the alkaline electrolyte, and thus reduced the overall efficiency of the fuel cell. Technologies with the non-alkaline electrolytes became more attractive for terrestrial applications, such as, solid oxide fuel cells, phosphoric acid fuel cells, molten carbonate fuel cells, and proton exchange membrane (PEM) fuel cells that were later considered the power source in vehicles.

Already in the early 1960s, Thomas Grubb and Leonard Niedrach developed the first PEM fuel cell while working in General Electric. The PEM fuel cell technology was interesting but not immediately adopted by National Aeronautics and Space Administration (NASA) space flights. The

era of PEM fuel cells on space flights started with Gemini 6 to 12, between 1965 and 1966. Then in 1979, the company Ballard Power Systems was established, and it has since grown to become a significant player in the PEM fuel cell technology. [Ehsani et al., 2005, pp. 13-19] [Cook, 2002]

Evolvement of a Diesel-Electric Powertrain in Heavy Vehicles

The diesel-electric powertrain has long been used in some applications, such as in locomotives [Teago, 1937], and ships [Harvey and Thau, 1925]. In the 1900s, electric propulsion was introduced to ships. In those days, electrical systems were various kinds of AC or DC systems, and a power source in the beginning was a turbine, and later on diesel engines were utilized [Harvey and Thau, 1925]. In about 1925, the diesel-electric traction began to compete with other propulsion systems in locomotives [Teago, 1937]. Some decades later, in 1947, a braking resistor system was proposed for a locomotive to prevent the need for brake shoe maintenance, wheel wear, and to increase faster schedules for operation [Weiser, 1947].

Concerns about the environment triggered more research on electric vehicles between 1955-1965, and as a result, a new thyristor inverter technology with advantages, including the use of asynchronous motors, was adopted to traction motor considerations [Wakefield, 1994]. Simultaneously, an earth-moving DC electric drive vehicle, the 100-ton with 1100-horsepower ore truck, was in commercial use. In those days, an ore truck powertrain consisted of a gas turbine as a power source, DC generators and motors. The motors were integrated in wheels with gearings [Kusko, 1968].

Research continued to adopt “commutator-less” AC-drives for locomotives, military vehicles, battery powered electric vehicles, and other types of NRMMs. In the middle of the century, NRMM powertrains were realized by diesel engines with gear-shift and torque-converter transmissions [Kusko, 1968]. By 1973, the new converter technology with asynchronous traction motors had been introduced to diesel-electric locomotives. At that time, a diesel-electric powertrain consisted of a diesel generator-set with a passive diode rectifier, DC intermediate circuit with a braking resistor, and thyristor-based inverters operating asynchronous traction motors [Brenneisen et al., 1973].

Rise of New Interest in Electric Vehicles

In the 1970s, the period of energy crises increased the interest of vehicle manufacturers towards electric vehicle research. The energy crisis

was a period in which the major industrial countries of the world faced substantial shortages of petroleum. The two worst crises of this period were the 1973 oil crisis, and the 1979 energy crisis. Oil prices first rose in the early 1970s, and then declined during the late 1970s, thus leaving electric vehicle research interest dependent on its environmental impacts [Rajashekara, 1994].

In the beginning of the 20th century, battery capacities were around 0.02-0.07 kWh/kg, and by 1988, it was understood that theoretical battery capacities would stay under 0.3-2.8 kWh/kg [Ehsani et al., 2005, pp. 13-19] and [Wakefield, 1994]. On the contrary, gasoline and diesel energy densities are in the range of 12 kWh/kg. Thus, it was agreed that electric vehicles could never compete with gasoline automobiles in the driving range. The automobile industry begun to concentrate on research of hybrid and fuel cell vehicles for long-range vehicular purposes [Ehsani et al., 2005, pp. 13-19]. Furthermore, energy densities of batteries are currently still within 0.05-0.15 kWh/kg [Thounthong and Raël, 2009].

In the 1960s, General Motors (GM) resurrected its research (since the 1910s) on electric and hybrid vehicles. For instance, in 1966, the first fuel cell van was demonstrated. At that time, the fuel cell system was reported to be too expensive and complicated.

In 1968, an electrically powered six-wheel military vehicle was demonstrated with ICE, AC generator, inverters, and wheel motors. That same year a series-hybrid powertrain, with the Stirling engine providing power to a passive battery pack, was tested in a small size passenger car [Rajashekara, 1994]. Thus, by 1983, research for hybridizing vehicle powertrains had already a long history. Meantime, development of a parallel hybrid test vehicle was reported in [Trummel, 1983].

By the 1990s, automobile manufacturers became interested in hybrid and fuel cell applications. Several demonstrations were made for both in the 1990s. Commercial markets of hybrid vehicles were initiated in 1997 by Toyota Prius [Chan, 2007], and the commercialization of the fuel cell vehicle is still waiting to begin. Fuel cell vehicles currently exist for all modes of transport. The most prevalent fuel cell vehicles are forklifts and material handling vehicles. However, there are currently no fuel cell cars available for commercial sale. The major challenges for fuel cell technology commercialization are on lowering the cost of volume production, and increasing reliability as well as permanence. [v. Helmolt and Eberle, 2007]

1.2 State of the Research

The previous section states the long history of electric, hybrid and fuel cell powertrains. Despite this lengthy history, the field of hybrid powertrain research is in a relatively early phase. An increase in publicly available publications related to the topic began in the late 1990s. However, this section concentrates on recent proceedings on the field, thus covering the early 2000s.

By the year 2007, Terminal Systems Inc. reported completion of the preliminary testing of their first ECO Crane with a diesel/battery hybrid powertrain [Stark, 2007]. The application is similar as in Fig. 1.1 (a), and studied in Publications I and V. Other proceedings relating to a comparable system have been reported in [Baalbergen et al., 2009] and [Kim and Sul, 2006].

Publication [Baalbergen et al., 2009] reviews six different energy management strategies (EMS) for a diesel-electric system with energy storage. Furthermore, that publication focuses on providing design rules for different series-hybrid powertrains with a passive high power (HP) battery pack or an active ultracapacitor pack as possible energy storage. The research proposes methods with which to compare different EMS strategies, and compares the HP battery powertrain topology cost sensitivities with different EMSs, but will not proceed to conclusions on the supremacy of either an active ultracapacitor buffering or an HP battery buffering. Furthermore, the study neglects weights and sizes of different powertrain options; moreover, the proposed methods for design are simple and superficial.

Publication [Kim and Sul, 2006] presents power control for a powertrain with diesel engine, separately excited generator with a diode rectifier, and DC-DC converter between a low capacitance intermediate circuit and UC energy storage. Tuning variables for power control in the system-level are generator excitation and intermediate voltage reference of a DC-DC converter.

In 2007, the journal *Proceedings of the IEEE* published a special issue related to the hybridization of vehicles, which reviewed the State-of-the-Art of the field. Therefore, it is publicly known that for vehicles driven on fixed routes and with a cyclic pattern, i.e. stop-and-go means, the fuel saving potential is an average of 50 % or more, with either parallel or series-hybrid powertrains [Chan, 2007]. Furthermore, it is self-explanatory that

for many vehicles, including hybrids, the most energy efficient path from fuel conversion to vehicle propulsion is the most direct path. For combustion engine driven vehicles, this means mechanical coupling; for fuel cell vehicles, this means directly through an intermediate bus without passing through an energy storage media, because every energy conversion generates losses [Lai and Nelson, 2007]. Therefore, general considerations are made to choose either a mechanical or a hybridized powertrain for each vehicle applications.

The following review classifies different powertrains with the control possibility of power electronics converters. In this context, a converter or energy storage (ES) coupling is termed passive, if it allows no controllability provided by e.g. hard switching of semi-conductors or due to direct coupling of a component. On the other hand, they are defined as active, if controllable semi-conductor technology is utilized. Furthermore, the fuel cell (FC) or the ICE primary source is another basis of classification for powertrains. Based on the categorizing, recently studied different series-hybrid powertrains are described in the following paragraphs. Reviews of Hardware-in-the-Loop environments, different modeling methods and tools, as well as general design considerations follow the classification of powertrains, and the final paragraph locates this dissertation to the State-of-the-Art context.

Powertrain with an engine generator-set, active rectifier, and passive battery pack

The powertrain topology presented in Fig. 1.3 and earlier covered in [Chan et al., 2010], [Chan, 2007], [Ehsani et al., 2005, pp. 13-19], [Baalbergen et al., 2009], [Bogosyan et al., 2007], and [Emadi et al., 2005]; is the first step forward from diesel-electric powertrains which are commonly utilized in trains and heavy high power ore trucks. The powertrain provides engine operation steadily on the chosen operating point, with commands of operation speed ω, and torque τ, which together define power p to a battery pack in the intermediate circuit.

Furthermore, passive HP batteries are proposed—specifically for charge-sustaining operation of series-hybrid powertrains [Baalbergen et al., 2009].

Publication [Bogosyan et al., 2007] presents dynamic modeling which takes into account both electrical and mechanical phenomena in the powertrain with an actively loaded ICE and passive battery pack.

Publication [Emadi et al., 2005] reviews different hybrid powertrain topologies, including series-hybrid, as well as heavy-duty FC hybrid; and

states the need for high power-density batteries in hybrid vehicles.

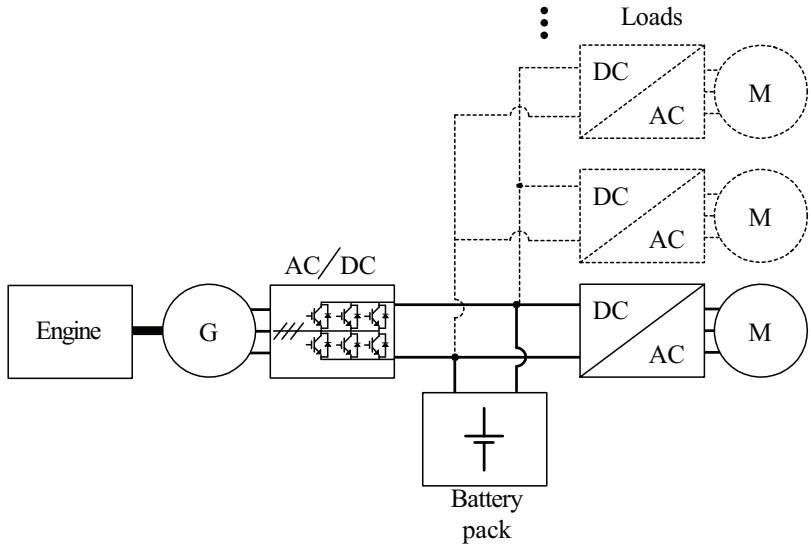

Figure 1.3. Powertrain with an engine generator-set, active rectifier, and passive battery pack.

Powertrain with an engine generator-set, active rectifier, and active battery pack

The powertrain topology presented in Fig. 1.4 is proposed in studies [Ehsani et al., 2007], [Chan, 2007], and [Gao and Ehsani, 2006]. The active battery pack refers to a battery that is controlled with a DC-DC converter.

In this topology, the powertrain control strategy becomes similar to the earlier powertrain case, if the DC-DC converter regulates voltage of a low capacitance intermediate circuit. However, there is another possibility for the powertrain control strategy that derives from the diesel-electric powertrain without energy storage. In such a case, voltage of the low capacitance intermediate circuit is regulated with the active rectifier, and the DC-DC converter primarily commands the current of energy storage.

Publication [Gao and Ehsani, 2006] states needed operation modes to control power flows in all relevant directions. Furthermore, a method is proposed for sizing of a traction motor, engine, and ESS. The sizing method is based on the maximum power needed from components of the powertrain. An energy-storage system design is discussed and the design of a hybrid energy storage explained, i.e. combined battery and UC. It is worth noticing that the hybrid energy storage has much less weight than a battery alone as the energy storage. In addition, both passive and active

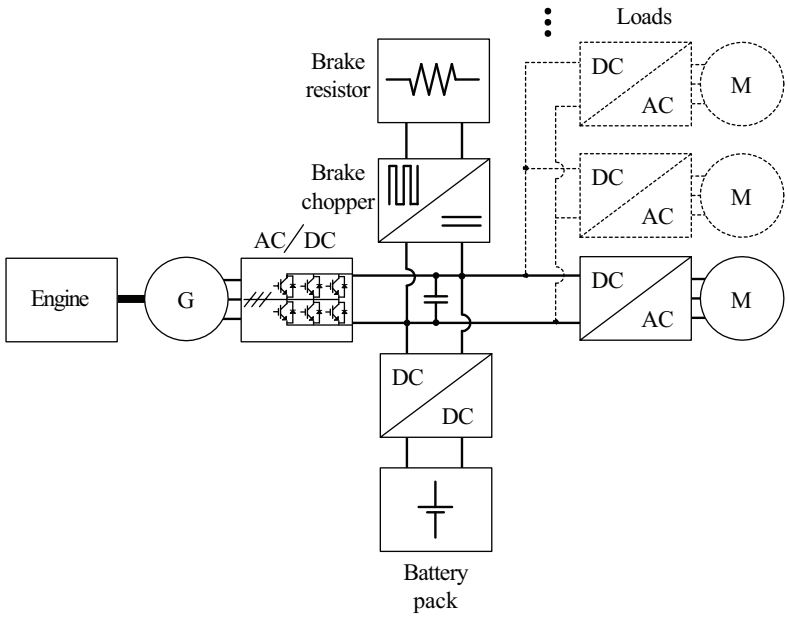

Figure 1.4. Powertrain with an engine generator-set, active rectifier, and active battery pack.

hybridizations of ESS are proposed.

Powertrain with an engine generator-set, active rectifier, and active UC pack

The powertrain with an engine and UC energy storage is shown in Fig. 1.5 and proposed in [Chan, 2007], [Baalbergen et al., 2009], [Lidozzi et al., 2010], and [Shibuya and Kondo, 2011]. Power control strategies in this case can include intermediate circuit voltage regulation features, the DC-DC converter regulation, and the active rectifier regulation. However, the voltage operation range of an UC pack delimits its control freedom in respect to the battery buffering case.

Publication [Baalbergen et al., 2009] proposes UC buffering for the crane application, suggests six different power management strategies and compares their costs. The study does not consider the sizes and weights of such systems.

Publication [Lidozzi et al., 2010] presents thoroughly the characteristics of the UC buffered powertrain with its parameters. In the case presented, the control strategy is such that the DC-DC converter regulates voltage of the low capacitance intermediate circuit; moreover, the active rectifier generates power flow from an engine depending on the state-of-charge (SOC) of UC, current derivative limitations, and the efficiency map of a

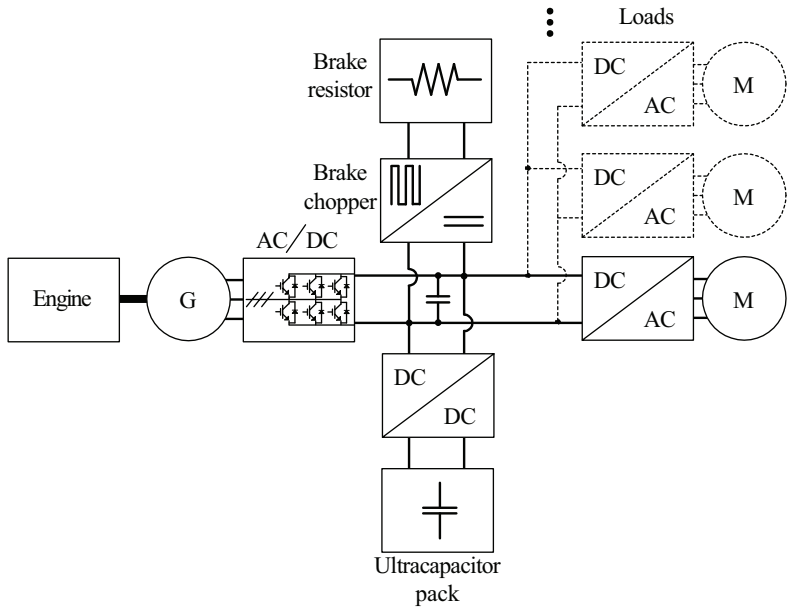

Figure 1.5. Powertrain with an engine generator-set, active rectifier, and active ultracapacitor pack.

combined active rectifier generator unit.

Publication [Shibuya and Kondo, 2011] proposes an energy management strategy to save both the power losses in the hybrid system, and capacitance of the UC pack. The strategy is based on keeping the summation of the kinetic energy and the UC energy constant. It is proposed that the engine is controlled in three steps: maximum, optimum, and auxiliary power regions. Furthermore, the study proposes a method to design an appropriate capacitance for the UC buffered diesel-electric powertrain in local or express train applications.

Powertrain with an engine generator-set, active rectifier, passive battery, and active UC pack

The powertrain with an engine, a passive battery as an intermediate circuit, and an active UC ESS as a peak power unit is presented in Fig. 1.6 and studied in [Camara et al., 2008, 2010].

The objective of publication [Camara et al., 2008] is on the dynamic control strategy of the DC-DC converters for an energy management between the batteries and supercapacitors. The dynamic modeling describes phenomena occurring on the intermediate circuit, which has parallel smoothing capacitors (1.5 mF) and a lead-acid battery pack with current smoothing inductor (25 μH) in series. The circuit creates the same phenomenon

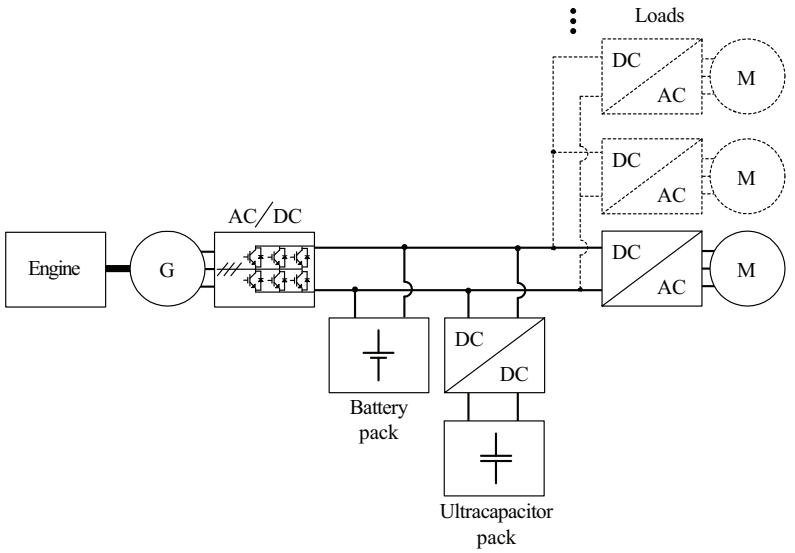

Figure 1.6. Powertrain with an engine generator-set, active rectifier, passive battery, and active ultracapacitor pack.

that can occur in the intermediate circuit with long cabling between different power electronics components, or between a power electronic component and a battery pack. This phenomenon has been assessed in Publication VII.

Publication [Camara et al., 2010] continues the research on the control laws of DC-DC converters in the energy management between battery and UC by polynomial control strategy, and by dynamic modeling of such systems. Both studies concentrate on optimizing the system by designing operation of the switching event time-scale.

Powertrain with an engine generator-set, passive rectifier, and active UC pack

The UC buffered diesel-electric powertrain with a passive rectifier is presented in Fig. 1.7 and studied in [Kim and Sul, 2006], and [Grbovic et al., 2011].

Publication [Kim and Sul, 2006] proposes improvements to EMS, which is based on both the DC-link voltage regulation and the engine generator-set droop frequency regulation. In EMS, the DC-link voltage regulation is used when primary power is fed by the active UC pack, thus, the DC-link voltage can be regulated to a value that does not allow the passive rectifier to conduct. Furthermore, while using regenerative braking, power transfers to the UC pack in the voltage control mode. In contrast, in the event of the UC pack being exhausted or the load too high, the engine

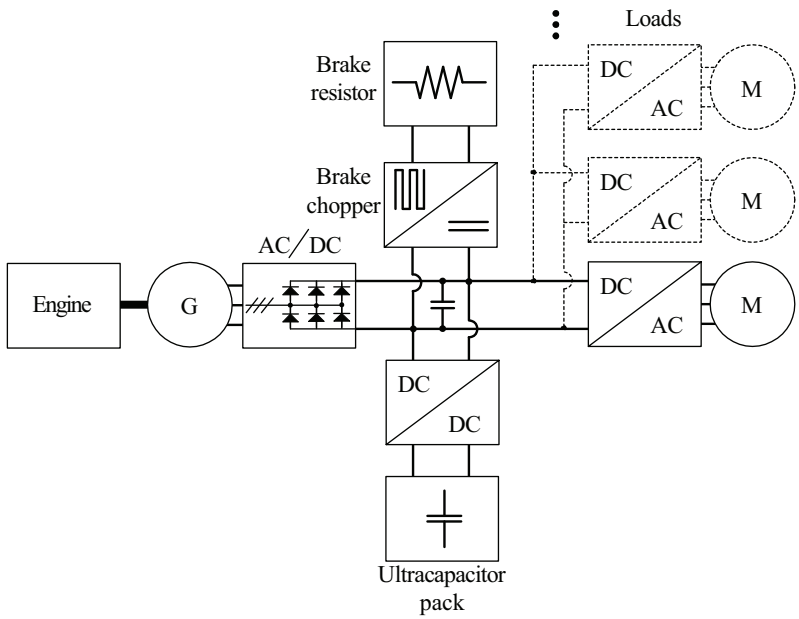

Figure 1.7. Powertrain with an engine generator-set, passive rectifier, and active ultracapacitor pack.

generator-set droop frequency regulation is chosen. Then, primary power is fed by the engine generator-set. If the droop frequency reference cannot be met, the UC pack assists the operation. The contribution of the study itself is on the estimator algorithm of the generator frequency for the operation of EMS. The study presents a hybrid powertrain with engine size decreased to one-third of the original. However, a drawback of the system is that the engine is used to charge the UC pack to ensure the operation.

Publication [Grbovic et al., 2011] concentrates accurately on electrical behaviors, and power electronics (PE) control in the system, thus neglecting system level operation issues outside the study. The paper proposes use of a bidirectional three-level DC-DC converter with energy storage, and a control algorithm for the converter to perform a power control that affects the system-level power flow. The proposed control algorithm seems to result in the ON-OFF operation of the two power sources. However, the contribution of the study is on the UC based energy storage design guidelines for such a system which has a ride-through capability against voltage sags (or dips, i.e., an instantaneous decrease in the RMS voltage with a range of 10...90 % and duration up to a minute) in the mains. Furthermore, the study is exact and systematic in its analysis, as well as discussing deeply issues relating to converter technology possibilities in such a system. The proposed power-flow control algorithm is based on

the DC-link voltage from which UC voltage and current references are calculated.

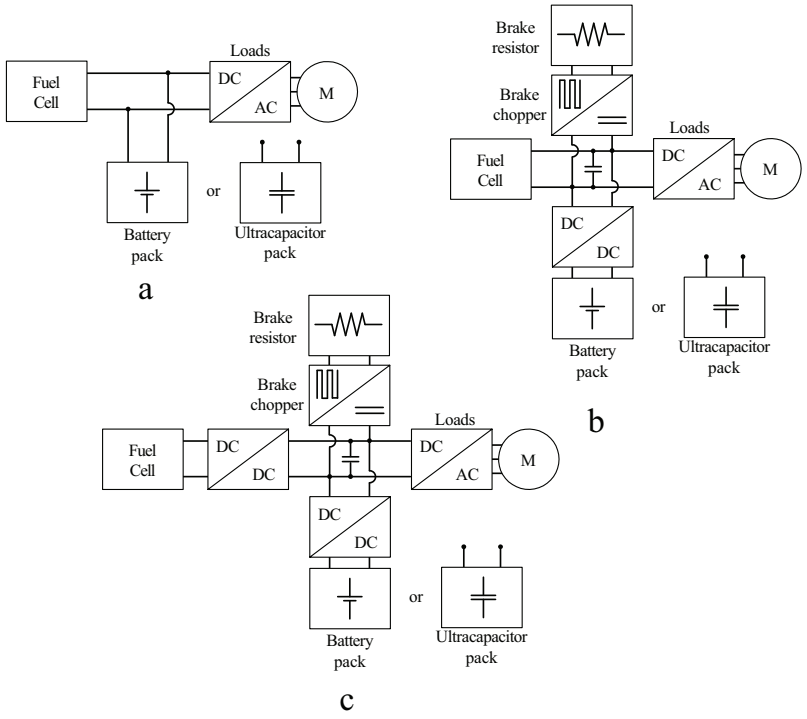

Figure 1.8. Different fuel cell source powertrain cases; (a) the powertrain with a passively coupled FC source and passive ES, (b) the powertrain with a passively coupled FC source and active ES, and (c) the powertrain with an actively coupled FC source and active ES.

Powertrain with passive or active coupling of a fuel cell source and a battery pack

Basic fuel cell source powertrain topologies with a battery buffering are illustrated in Figs. 1.8(a)...(c), and studied in [Lai and Nelson, 2007], [Thounthong and Raël, 2009], [Emadi et al., 2005], [Gauchia and Sanz, 2010], and [Gao, 2005].

Publication [Lai and Nelson, 2007] proposes FC powertrains with: passive coupling of FC and UC, cf. Fig. 1.8(a), passive coupling of FC and active coupling of battery pack, see Fig. 1.8(b), as well as active coupling of FC with ESS, cf. Fig. 1.8 (c). In the study, the passive coupling of the FC source is justified by fewer losses on the primary power path, and the active coupling of the FC source is justified only by a matching of the intermediate circuit voltage. Thus, the efficiency of the FC-converter is extremely important due to its direct effect on the vehicle fuel consump-

tion.

Publication [Thounthong and Raël, 2009] investigates a modern tramway as a hybridization target. In such a system the powertrain is doubled, the tram is equipped with both, a generator sized based on the peak load power, as well as overhead lines for supply and regenerative power. By hybridization, overhead lines can be removed and generator size decreased to supply only average power, which in this case is less than a third of the peak load power. The average power operated generator is reversible with the FC source, and thus, an actively coupled FC with passive battery pack is proposed as well as an actively coupled FC with active UC. The energy management algorithm for the active FC and passive battery pack case is based on the battery SOC that is maintained with control of the FC source. Additionally, the algorithm consists of battery current limitations, and current slope limitations for the FC source. The energy management for the active FC and active UC powertrain is realized with the DC-link voltage regulation (PI-controlled) by the UC-converter, while the FC-converter is controlled to maintain the UC state-of-charge (P-controlled). Both controller outputs are limited to ensure usage within safe operation areas of the sources. Design examples of both energy storages are presented, and algorithm operations are verified by experiments.

Publication [Emadi et al., 2005] reviews schematics of fuel cell based powertrains for passenger cars and heavy-duty transit buses.

Gauchia and Sanz [2010] present a reduced scale Hardware-in-the-Loop test system for a powertrain with a passive FC coupling, and passive battery pack. The study proposes a low-cost, effective, and easy to adapt design environment that combines parts of real hardware, and parts replaced by emulating tools.

Publication [Gao, 2005] compares three powertrain cases, a passively coupled FC with an active battery pack, a passively coupled FC with an active UC pack, and a passively coupled FC with both active battery and active UC packs. This publication concludes that the case with both battery and UC packs is the most promising powertrain topology for passenger car applications. The conclusion is affected by the fact that calculation parameters for a battery are based on the lead-acid technology instead of other types of batteries with higher specific power. The profitability of the combined active high-energy (HE) battery and active UC buffering with respect to battery or UC only topologies was also concluded in Publication V. Furthermore, in some applications, the combined battery-UC pack ES

is replaceable with the proper design of an HP battery. However, features of these powertrain cases are dissimilar due to different amounts of energy in the ES system, and thus, they might become suitable for different applications.

FC powertrain with an UC pack buffering

The FC powertrain with an UC buffering, cf. Fig. 1.8, is considered in studies [Lai and Nelson, 2007], [Thounthong and Raël, 2009], [Gao, 2005; Greenwell and Vahidi, 2005; Feroldi et al., 2009; Bernard et al., 2009; Lin and Zheng, 2011; Moreno et al., 2006; Miller et al., 2006]; and buffering with a flywheel in [Miller et al., 2006]. Issues discussed in publications [Lai and Nelson, 2007], [Thounthong and Raël, 2009], and [Gao, 2005]; were reviewed in the previous section.

Publication [Greenwell and Vahidi, 2005] compares two different EMSs for a powertrain with an actively coupled FC source and active UC pack. Compared EMSs are a rule-based method and a model predictive control (MPC) method. Both EMS cases are based on a low-level control strategy in which the DC-bus voltage is regulated with the FC-converter, and the UC-converter is controlled with the current reference. In both cases, the low-level control strategies are the same as those proposed for the diesel-electric series-hybrid powertrain in Section 2.1.11, and in Publications II, III, and IV; i.e., the DC-bus voltage regulation with the primary source converter, and the current controlled UC pack. The rule-based EMS relies on a high-pass filtering of the load current, which defines the UC current reference with compensation of power losses and change of voltage potential. Furthermore, the FC source is targeted to be operated near the optimal operation point. The MPC approach utilizes a model of the system to project the future response as a function of control inputs and known disturbances. The designs of both controllers are briefly explained, and the behaviors of design examples compared. Conclusions between behaviors are drawn, but no real differences on performances were comprehensively reported.

Publication [Feroldi et al., 2009] presents an approach for the design and analysis of FC-UC hybrid systems oriented to automotive applications. The design issues of the powertrain with an actively coupled FC and active UC are discussed, and then a presentation is made of the powertrain design approach based on drive cycle parameters resulting in the proper sizing of FC and UC. The study concludes that the most suitable

hybridization degree of the FC-UC powertrain for an automotive application is 79 % that is a suitable value for urban driving cycles, as stated in publication [Bernard et al., 2009]. The proposed result in [Feroldi et al., 2009] is based on calculations with different driving cycles. The hybridization degree (HD) is defined, as

$$\mathrm{HD} = \frac{P_{\mathrm{ess,max}}}{P_{\mathrm{fcs,max}} + P_{\mathrm{ess,max}}} \cdot 100[\%], \tag{1.1}$$

where $P_{\mathrm{ess,max}}$ is the maximum ESS power, and $P_{\mathrm{fcs,max}}$ is the maximum fuel-cell system power, respectively.

Publication [Bernard et al., 2009] studies proper sizings for FC-battery and FC-UC topologies (considering the degree of hybridization), and discusses approvable design domains, as in [Baalbergen et al., 2009]. Furthermore, publication [Bernard et al., 2009] concludes different hybridization degrees for powertrains depending on a driving cycle. In both powertrain cases, the hybridization degree varies in 20...80-%, depending on whether the driving cycle represents sub-urban or urban driving, respectively.

Publication [Lin and Zheng, 2011] proposes an adaptive optimal-control (AOC) method as EMS for the powertrain with an actively coupled FC and active UC pack. The design and learning routine of the neural network based AOC method is presented, and comparison against a fuzzy logic based EMS has been assessed. Conclusions favor the AOC-EMS method in respect to the fuzzy logic based method designed by an expert. The tuned AOC algorithm takes load power and SOC as inputs, and gives the fuel cell power reference as output to a low-level control algorithm. The idea of the AOC-EMS is similar as in the EMS designed in Publications II, III, IV, and presented in Section 2.1.11.

Publication [Moreno et al., 2006] is an earlier study of neural networks usage (in respect to publication [Lin and Zheng, 2011]) for EMS of the powertrain buffered with the active UC pack. The study proposes a more complex neural network with eight inputs, and with one output as the UC pack current reference. Moreover, the study neglects operating points of a primary energy source, since it concentrates on the active UC buffering in general.

Publication [Miller et al., 2006] reviews feasibilities of a hybrid powertrain in different train applications. It is noted that a hybrid powertrain is not advantageous in all train application cases, such as in locomotives for high-speed, heavy freight, and switcher applications. The reasons for previous cases are either extended periods of maximum power (high-speed,

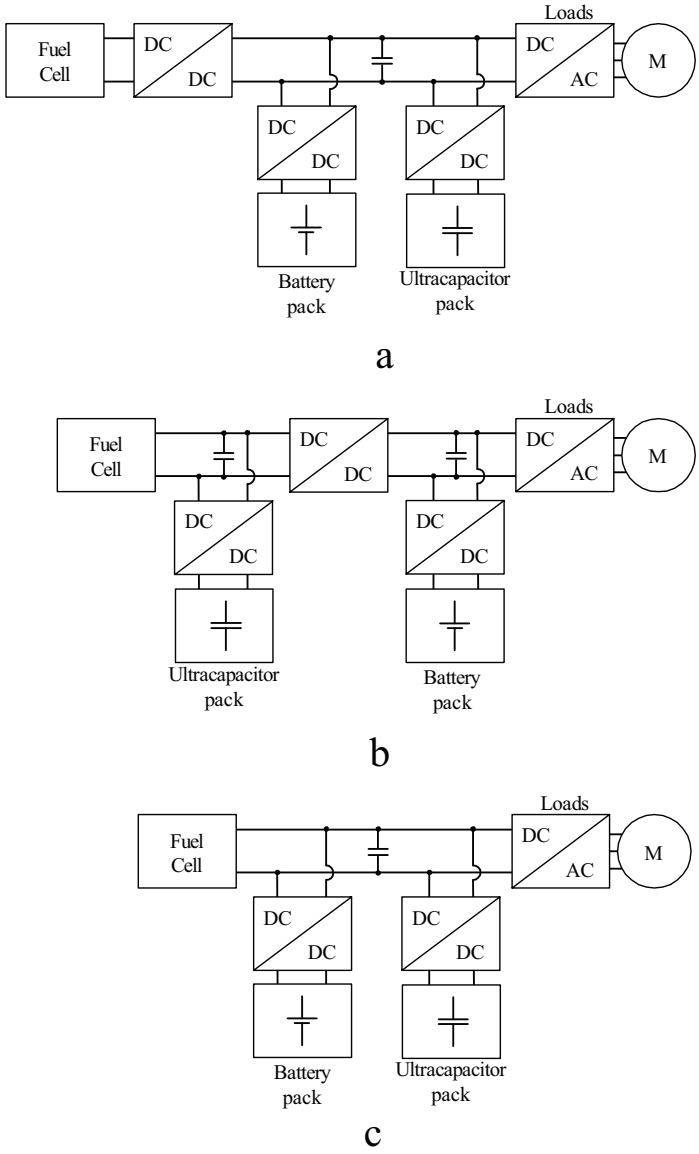

Figure 1.9. (a) Powertrain with an actively coupled FC source, active battery, and active UC, (b) the powertrain with a passively coupled FC source, and active ESs in two different DC-buses, and (c) the powertrain with a passively coupled FC source, active battery, and active UC. For the sake of simplicity, possible brake units have been left out of the Figure.

heavy freight), or low-speed (switcher) operations where power provided by the powertrain is less of an issue due to the limitations of wheel adhesion. On the other hand, a hybrid powertrain may be beneficial in subways, mass transit, commuter, and intercity rail applications.

FC powertrain with a combined battery and UC buffering

As the last group of introduced topologies, a FC powertrain with two energy storages has been investigated in [Woonki et al., 2011; Zandi et al., 2011; Wang and Li, 2010; Yu et al., 2011; Zhang et al., 2008]. Different methods exist to realize a FC powertrain with two energy storages, as shown in Fig. 1.9.

Publication [Woonki et al., 2011] presents predictive controllers for different converters in the powertrain with a FC source, active battery, and active UC packs, cf. Fig. 1.9(a). The proposed predictive controllers are for low-level controls, and they are proposed to replace classical PI-regulators from each converter. Predictive controllers have been demonstrated to be faster with simulations and validation measurements in a reduced scale test bed. Use of predictive controllers in each converter low-level control results in faster dynamic system responses.

Publication [Zandi et al., 2011] presents an energy management strategy based on the flatness control technique and the fuzzy logic control. The studied EMS is proposed for the generic battery and UC buffered topology, but the study presents a design example for a powertrain with two DC buses from which one connects to a FC source and active UC pack, and via other DC-DC converter to a higher voltage DC bus, and to loads, and to an active battery pack, see Fig. 1.9(b). The main property of the proposed EMS is that, power flow of the system in different operating modes is managed with the same control algorithm without any algorithm commutation or prediction of the system behavior. Furthermore, the flatness control is utilized to divide load power between the FC source and the ES system, and the fuzzy logic control is used to divide the ES system current between the battery and UC packs.

Publication [Wang and Li, 2010] studies a powertrain with a passively coupled FC source, active battery, and active UC pack, which, actually is in the control point of view as Fig. 1.9(c). The study proposes use of a three-port isolated triple-half-bridge DC-DC converter for ESs, and proposes two different EMSs for the powertrain. Furthermore, a design routine is provided to size the battery and UC in order to achieve the lightest mass at the 95-% efficiency. The study concludes that the constant operation of the FC source leads to higher system efficiency in the studied case than the ON-OFF operation of the FC source.

Publication [Yu et al., 2011] proposes a dynamic power distribution between the FC source, battery, and UC, see Fig. 1.9(a). The powers between

the FC source and ES system, as well as active battery and active UC are individually controlled; and a proposal made for a global optimization controller with real-time capability. Simulations have been used to prove the feasibility of the proposed control against common thermostatic controls. Results suggest a great benefit over urban driving, and lesser benefit to sub-urban driving. Furthermore, the study presents cost functions for optimization of both controllers.

Publication [Zhang et al., 2008] presents the design of an energy management based on a wavelet transform for a powertrain with an actively coupled FC source, active battery, and active UC packs. The proposed wavelet-transform algorithm is capable of identifying the high-frequency transient and real-time power demand of the HEV, and allocating power components with different frequency contents to corresponding sources. Simulations of the proposed control were presented, and experimental data for verification and validation of results have been created with a reduced scale test bed.

Hardware-in-the-Loop environments

State of the research in the design of different powertrains has been presented in previous paragraphs. Furthermore, different approaches for Hardware-in-the-Loop environments for supporting research have been presented in publications [Gauchia and Sanz, 2010], [Hentunen et al., 2010], and [Oh, 2005].

The ideas of publication [Gauchia and Sanz, 2010] were discussed in an earlier section. A full-scale Hardware-in-the-Loop environment that is used for research in this dissertation is presented in publication [Hentunen et al., 2010]. In addition, useful test setups regarding performed research and relating to publication [Hentunen et al., 2010] are presented in Section 2.1.1.

Publication [Oh, 2005] presents an idea of two reverse-coupled electric machines emulating a driving cycle for use of the traction unit testing in different hybrid powertrains. In such a system, one of the electric machines is controlled with speed, and the other with torque command based on driving cycle and vehicle parameters.

Different modeling methods

According to Chan et al. [2010], different modeling methods can be used for different objectives of the study. For instance, the objective may be such as component design, topology analysis, energy or pollution assess-

ment, or energy management. Especially, for the energy management of new vehicles, models have been developed for two different uses: 1) local control of the subsystems and 2) supervision of the entire vehicle. However, it should be highlighted that some developers use today the same model for different objectives.

In order to avoid confusions, definition of some terms and concepts are needed. This dissertation and its definitions have been written in accordance with Chan et al. [2010], as well as Guzzella and Sciarretta [2007].

- *Static model* or a part of a model refers to experimental data of subsystem behavior that is implemented, e.g., with look-up tables.

- *Quasi-static model* is used when a model uses a static model with some dynamics description.

- *Dynamic model* use is two-fold. In the multi-stage approach it is used when a sub-model has some dynamics description, and has influence on the upstream of the power-flow calculation direction. In the dynamic modeling of the DC bus of the series-hybrid powertrains its use is self-explanatory due to natural aim to forward and causal models that are targeted to the control and stability analysis.

- *Functional model* is used when a model primarily imitates operation of a targeted device. It is made of interconnected mathematical functions that may have both causal and non-causal features.

- *Forward model* is also called the engine-to-wheel or the rear-to-front model. In the case of a sub-model, the term highlights that the model has influence to the upstream of the power-flow calculation direction. In the case of a system model, the action is required before the re-action, thus in the all-inclusive vehicle model case “Driver model”, “Environmental model”, “Tire interface model”, and “Traction control algorithms” are needed.

- *Backward model* is also called the wheel-to-engine or the front-to-rear model. In the case of a sub-model, the term highlights that the model has influence only to the downstream of the power-flow calculation direction. However, in the case of a system model, the term highlights the

power-flow calculation direction from loads to sources.

- *Multi-stage modeling approach* is used to describe a system model that consists of segments of previously defined modeling methods.

- *Causal model* uses the normal relation for the cause and effect.

- *Non-causal model* brakes causality by calculating the cause for the desired effect.

Different modeling tools

- *ADVISOR* is designed for rapid analyses of the performance and fuel economy of conventional, electric, and hybrid vehicles. It is an empirical model, using a backward/forward approach, intended for analyses and not for design.[2]

  It emphasizes more on the backward-facing calculation side than the multi-stage approach used in this dissertation, thus allowing relatively long simulation time-steps and faster simulations.

  A weakness of ADVISOR for use in the design of series-hybrid powertrains with conceivable DC buses is that interfaces of electrical components are realized with power, and not in current and voltage. This weakness omits controller interactions between electrical components, especially, if coupled with a DC bus.

- *Autonomie* and its predessor the *Powertrain System Analysis Toolkit* exploit forward models [Chan et al., 2010] that enable wide-ranging use for various purposes of the model based design.

- *Bond Graphs* were developed in the 1960s. It is a method for graphical formalism to organize models of complex multiphysical systems. In this method, elements of a multiphysical system are linked by bonds that have two properties, flow and effort [Chan et al., 2010].

- *Dymola* and *Matlab* provide structural models focused on the design and analysis of different systems. A structural model has interfaces according to its physical structure, and thus in some cases introduce

[2] ADVISOR Documentation. [Online]. http://bigladdersoftware.com/advisor/docs/advisor_doc.html (Last accessed on 19th of Sept. 2013)

non-causalities to models. They use powerful solvers to enable efficient simulation of complex systems [Chan et al., 2010].

- *Causal Ordering Graphs* (COG) and *Energetic Macroscopic Representation* (EMR) technique were developed from the 1990s to 2000s. They are methods for graphical formalism of complex multiphysical systems that require physical causality of models. Due to the physical causality, control schemes can systematically be deduced from the process graph. COG uses flow and effort as two different connections between elements, whereas EMR uses the action-reaction principle between elements, as well as highlights the energy properties of these elements by macro pictograms [Chan et al., 2010].

- *Quasi-Static Simulation*, i.e. QSS toolbox, is intended for the optimization of the fuel consumption of vehicles under various control strategies, since its approach results to fast computing times of one driving cycle. It is not intended for the capture of dynamic phenomena.[3]

  As ADVISOR, the approach of QSS also emphasizes more on the backward-facing calculation side than the multi-stage approach. It has similar weakness as ADVISOR, the control of the power flow is assumed to be ideal. As already mentioned, this weakness omits controller interactions of electrical components, especially, if coupled with a DC bus.

Discussions of different modeling methods and tools

The multi-stage approach in this dissertation is unique in the way of its emphasis on the design of series-hybrid powertrains with conceivable DC buses. This multi-stage approach is particularly tailored for the design of powertrains of NRMMs that differ from road vehicles by their dimensions, power requirements, production amounts, emission regulations, and permanence of environmental conditions. A multiform application field with different characteristics enable use of various series-hybrid powertrains. Due to diversity and complexity of powertrain options, fidelity of modeling approach is increased with respect to ADVISOR and QSS, which require smaller modeling time-steps and longer computing times.

The definition of the multi-stage approach is used in this dissertation due to difficulties to categorize the system model within a group of terms.

[3]The QSS toolbox manual. [Online]. http://www.idsc.ethz.ch/Downloads/DownloadFiles/qss (Last accessed on 19th of Sept. 2013)

Modeling approaches such as in ADVISOR, or QSS may as well be described as multi-stage approaches. However, they are tailored for the different level of abstraction since both approaches use a power interface between sub-models and not the current-voltage interface, thus losing causality of current and voltage. ADVISOR and QSS are more emphasized towards the backward-facing calculation than the multi-stage approach. COG and EMR can be categorized, according to their definition, as causal models for complex systems.

On the other hand, the dynamic forward map-based modeling represents a more complete vehicle powertrain system-model, contradictory to the proposed multi-stage modeling approach that concentrates only on the powertrain design beginning from the tractive effort or the drive cycle.

The dynamic forward system models for some series-hybrid and power-split powertrains have been presented and validated in publications [Bogosyan et al., 2007; Syed et al., 2006].

Forward and backward, as well as dynamic and quasi-static modeling approaches are widely discussed in [Chan et al., 2010], [Oh, 2005], and [Guzzella and Sciarretta, 2007].

In the modeling approach framework, this dissertation concentrates on how to combine different modeling methods—specifically for the design of different series-hybrid powertrains of NRMMs.

General design considerations

In low-capacitance intermediate circuit powertrains, a conspicuous issue is a value of the required minimum capacitance to guarantee stability of the DC link. As stated in Pietiläinen et al. [2006], the minimum capacitance for traction drives is much higher than for grid-connected drives. Pietiläinen et al. [2006] derives example values for the minimum capacitances to be $C/P_{\mathrm{nom}} > 195$ μF/kW for traction drives, and $C/P_{\mathrm{nom}} > 23$ μF/kW for grid-connected drives.

Sudhoff et al. [1998]; Pietiläinen et al. [2006] propose a method for an active stabilization of the DC bus based on the manipulation of the current reference component that produces torque. As an alternative, Hinkkanen et al. [2007] suggests a method for the stabilization based on the manipulation of the stator voltage reference. The latter approach becomes beneficial when the bandwidth of the current control loop is less than the resonance frequency in the intermediate circuit.

Harnefors and Nee [1998] recommends as a rule of thumb for the control of AC machines that the sampling frequency of the current controller should be selected at least ten times higher than the bandwidth of the current control loop. With two samples per a switching cycle, i.e., the angular switching frequency ω_{sw} should be higher than five times the bandwidth of the current control loop α_{c}, i.e. $\omega_{\mathrm{sw}} \geq 5\alpha_{\mathrm{c}}$ [Pietiläinen et al., 2006].

Lidozzi and Crescimbini [2012] presents an adaptive direct tuning for the DC-link voltage PI-controller parameters of an AC-DC converter. The idea is to ensure the desired DC-link voltage control performance disregarding output power fluctuations. Furthermore, a DC-link current feedforward technique is proposed to improve the control stiffness of the DC-link voltage. Both methods are illustrated to improve load step behaviors.

Framework of this study in the State-of-the-Art context

The framework of this study is on the guidelines of systematic and effective series-hybrid NRMM powertrain modeling for designing powertrain hardware dimensions and software algorithms. Modeling of the series-hybrid powertrain is separated into two approaches such as the multi-stage and dynamic modeling methods due to the manageability and computing time, although some developers use the same model for different objectives. Contributions are given, in Publication I, to categorize control methods to the reactive and predictive methods, and to the local as well as the supervisory reactive methods.

In the early phase of the research, the focus was on realization of multi-stage plant models and in validation of those models. Then, concentration was changed to local reactive control methods in different series-hybrid powertrains. Special emphasis was given to the UC buffered diesel-electric series-hybrid powertrain with an indirect primary source power buffering. The multi-stage modeling approach with specific reactive energy management methods was used for comparison case studies which included comparisons of different energy management algorithms to powertrain operation in Publication IV, comparison of properties between different FC series-hybrid powertrains in Publication V, and dimensioning of a powertrain with time-domain simulations in Publication VI. Finally, an approach of dynamic modeling for stability assessments of multiport DC buses in power-electronic systems are introduced in Publication VII, and example assessments given for one powertrain case.

2. Modeling

Nowadays, calculation and modeling methods are well developed for solving various electrical engineering problems. Accurate approaches for modeling of a single apparatus or phenomenon are usually available. Furthermore, design rules of apparatuses are increasingly found in the literature.

However, difficulties arise when exhaustive amount of information is combined to a specific use. System level engineering combines apparatuses to exploit benefit of increasingly controllable systems, which undoubtedly creates systems that are more complex. In order to avoid exhaustive complexity in system models, alternative modeling approaches with different fidelities and purposes of use are needed.

This Chapter introduces modeling in two perspectives. First, Section 2.1 introduces the multi-stage modeling approach for system level design of an energy management, dimensioning of a powertrain, and comparisons of system level designs. This approach is used in Publications I...VI. Similar combined backward and forward-facing approaches are used e.g. in ADVISOR [Markel et al., 2002], and Quasi-static simulation (QSS) [Guzzella and Sciarretta, 2007] that, however, are tailored for analyses of powertrains of road vehicles, and they emphasize more on the direction of the backward-facing calculation. Section 2.2 introduces dynamic modeling of powertrain components for the control and stability analyses of different powertrain options. This section reviews relevant background information for the approach in Publication VII. The final section of this Chapter reviews error analysis approaches such as the maximum error via the partial differential equation, and the Monte-Carlo method.

2.1 Multi-stage Modeling of Series-Hybrid Powertrains

An introduction to the studied series-hybrid drivelines, their variables, and principles of multi-stage plant models are presented in Figs. 2.1 and 2.2.

The basis of plant models are control delays of sub-systems and mappings of quantities, such as efficiency and fuel consumption. The control delays are either constant or variable. In this study, the control delays τ_{AFE} and $\tau_{\mathrm{DC/DC}}$ are constant, whereas τ_{e} is dependent on speed, and fuel quantity controlled by a speed PI-regulator.

The power conversion losses are considered with efficiency mappings. Efficiency affects the magnitude of a variable on the unregulated side of a sub-system component. For example, the active front-end (AFE) converter-generator combination efficiency mapping $\eta(n_{\mathrm{G}}, \boldsymbol{\tau}_{\mathrm{req}})$ is a function of the generator speed n_{G} and requested torque $\boldsymbol{\tau}_{\mathrm{req}}$. Furthermore, the DC-DC converter efficiency mapping $\eta(i_{\mathrm{es}}, u_{\mathrm{ratio}})$ is a function of the energy storage current i_{es} and the voltage conversion ratio u_{ratio}.

In Fig. 2.1, the primary control signal for the variable speed diesel generator-set (VSDG) is speed value (n_{VSDG}), which speed regulator gives fuel quantity ($\dot{m}$) as an output. The AFE converter is controlled with the DC-link voltage reference, which voltage regulator gives i_{AFE} as an output. The DC-DC converter is controlled with the current (i_{uc}) reference.

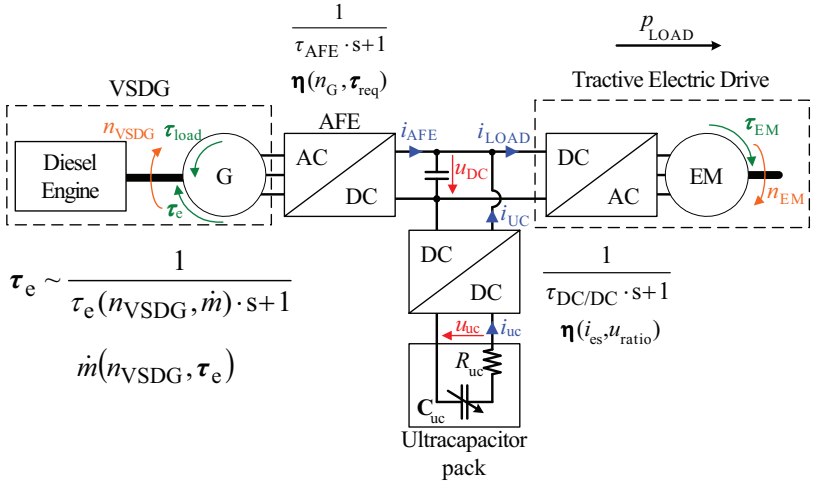

Figure 2.1. Active UC buffered diesel-electric powertrain. Powertrain variables and principles of plant models.

In addition, Fig. 2.1 presents a plant model for the ultracapacitor pack. It consists of either constant (C_{uc}) or variable capacitance ($\mathbf{C}_{\mathrm{uc}}$) value, and the equivalent series resistance R_{uc}.

The existence of the tractive electric drive plant model is dependent on the starting point of the simulation, mechanical or electrical load, p_{mech} or p_{LOAD}, respectively.

An example of the fuel-cell series-hybrid powertrain is presented in Fig. 2.2. It introduces a battery pack and fuel cell source plant models, as well as their variables. This figure presents the active battery and UC pack buffered powertrain.

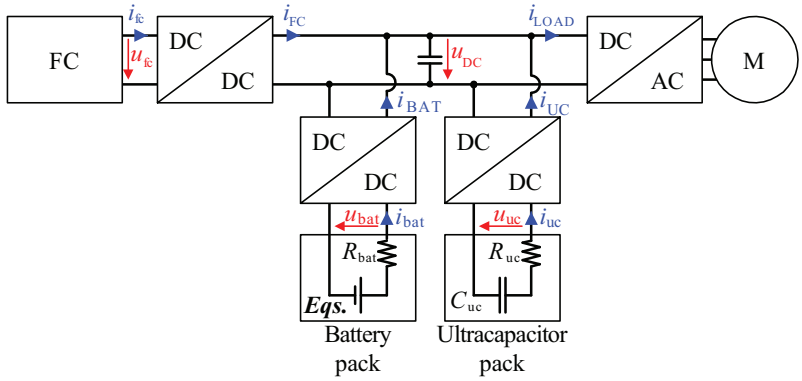

Figure 2.2. Active battery and UC pack buffered powertrain with the fuel cell source. Powertrain variables. The abbreviation *Eqs.* within the battery pack refers to equations 2.23. . . 2.24.

2.1.1 Test Setups for Experimental Identifications and Validations of the Sub-system Models

The identification of the DC-DC converter and the UC module plant models can be performed with the test setup presented in Fig. 2.3. The test setup consists of the AFE converter connected to the mains, the DC-DC converter connected between the AFE converter and the UC module, as well as measuring and data-acquisition systems.

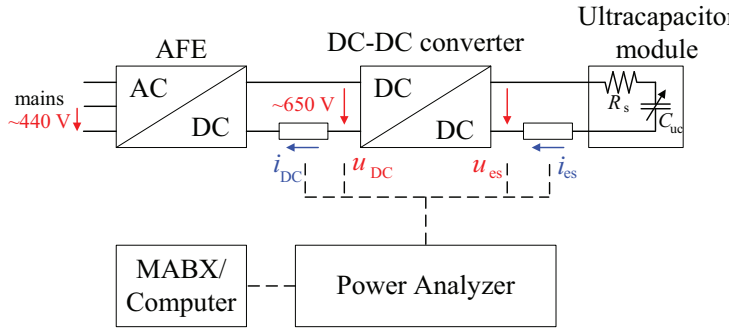

Figure 2.3. Test setup for the DC-DC converter and ultracapacitor module identification.

The devices in the test setup were *NXA_0460 5* (Vacon Plc.) for AC/DC conversion, *MSc200DCDC750* (MSc Electronics Plc.) for DC-DC conversion, *BMOD0018 P390* (17.8 F, 390 V, Maxwell Technologies Inc.) as the UC module, *Norma D6100* (LEM) as the measuring device with current shunts for 6...300 A, and dSpace *MicroAutoBox 1401/1501/1507* (MABX) as the data-acquisition and control hardware.

The identification of speed control responses of the VSDG plant model can be performed with the test setup presented in Fig. 2.4. The test setup consists of VSDG, diode rectifier, DC-DC converter, and load resistor with parallel capacitors. VSDG in the test setup was *49 DTAG* (AGCO Corporation Plc.) with the custom-made axial flux permanent magnet machine *PMG120-2000* (Axco-Motors Plc.) as a generator.

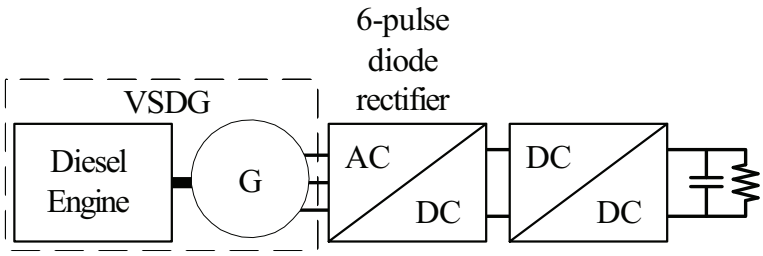

Figure 2.4. Test setup for identification of the plant model of the variable speed diesel generator-set.

The validation test setup for the DC-DC converter and the UC plant models, and for the supervisory control algorithms is presented in Fig. 2.5. Validation tests for the plant model of the DC-DC converter with supervisory algorithms, and for UC models are shown in Fig. 2.6(a)...(b). The tractive electric drive in the test setup consisted of Siemens *ELFA 1PV5135-4WS28* traction electric machine and *G650 D44/170/170 M7-1* inverter. The braking electric drive consisted of the same asynchronous machine model, and an industrial frequency converter (Vacon Plc.) with a braking resistor. The AFE converter *NXA_0460 5* (Vacon Plc.) regulated the DC-link voltage around 650 V and supplied the primary source current i_{AFE}. The DC-DC converter between the DC link and the UC module had the continuous i_{es} current of 120 A, the maximum current of 200 A, and the minimum current of 20 A in the ES voltage level. Fig. 2.7 presents the test setup of the full series-hybrid powertrain system.

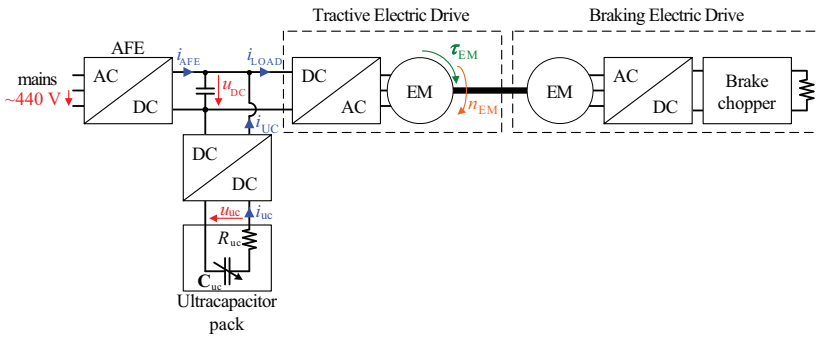

Figure 2.5. Hardware-in-the-Loop test setup for validations of plant models of the DC-DC converter and ultracapacitor module.

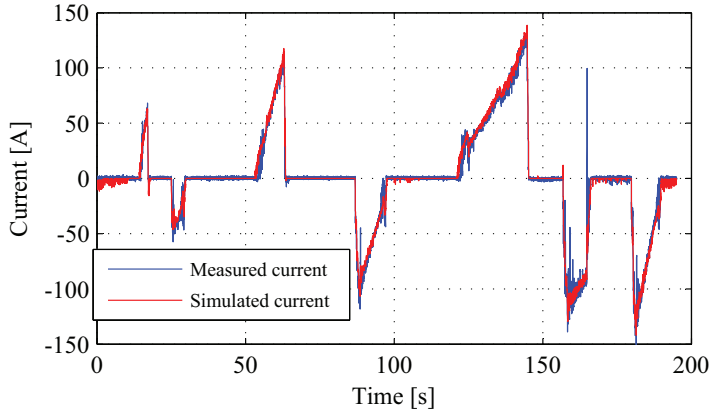

(a)

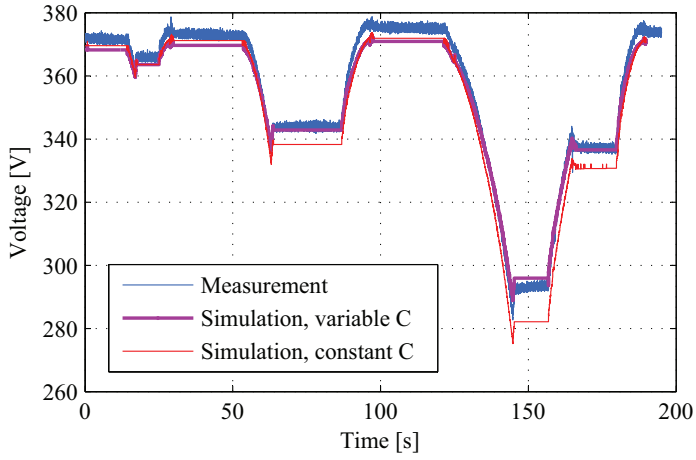

(b)

Figure 2.6. Validation tests; (a) i_{uc} of a DC-DC converter model, and (b) u_{uc} of UC models.

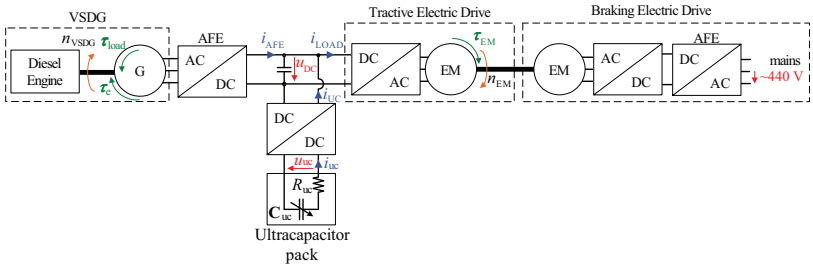

Figure 2.7. Full Hardware-in-the-Loop test setup for an active UC buffered diesel-electric powertrain .

2.1.2 Basis of Plant Models

The target of the plant models is to envisage mean values of powertrain variables with approximately the 20-Hz bandwidth. The targeted bandwidth is in the range of a DC-link voltage controller, whereas a chosen time-step for simulator is in the range of current-controllers within such a system. Furthermore, the designed sub-system models should be 'fast' to provide efficient rapid control prototyping of an energy management [Broy et al., 2007]. In this context, the word 'fast' refers to system models that finish a whole driving cycle in a time-period of several minutes rather than within several hours. This approach enables modeling of local reactive controllers for power electronic devices in a system.

The backward-facing approach enables time-steps approximately of one second as stated by Markel et al. [2002], and such simulators exists, for instance the Quasi-static modeling toolbox developed by Guzzella and Sciarretta [2007]. Such relatively large time-steps result to simulation times in the range of few seconds for driving cycles. However, the backward facing and modeling approach of Guzzella and Sciarretta [2007] have their assumptions as, in some cases, there is no influence on upstream direction, or faster phenomena than one Hz-bandwidth are not even tried to be modeled [Katrašnik et al., 2007]. In such a case, only functionality of reactive controllers for power electronic devices can be modeled.

The backward functional modeling from the imposed load cycle towards the primary energy sources power delivery is appropriate, which is computationally lighter, for example, than the forward modeling method. The backward model approach is also known as the wheel-to-engine and the front-to-rear modeling [Chan et al., 2010]. The differences to the forward modeling are that the backward model lacks "Driver model", "Environmental model", "Tire interface model", and "Traction control algorithms",

as the starting point of the proposed model is the load cycle of the existing NRMM.

In the proposed modeling approach, different descriptions for plant models are used, such as static, quasi-static, dynamic, and functional. In this context, the static model or a part of a model refers to one- or two-dimensional mappings of sub-system behavior. Thus, efficiency mapping of an electric drive or FC output voltage behavior, e.g. as $u_{\mathrm{fc}} = \mathrm{f}(i_{\mathrm{fc}})$, are considered as static models. The quasi-static definition is used when a model uses a static mapping with some dynamics description, but does not influence the up-stream of the calculation direction, i.e., a quasi-static model assumes backward calculation and a dynamic model forward calculation, respectively [Guzzella and Sciarretta, 2007, p. 70]. In the proposed approach, there are quasi-static characteristics in several sub-system models, such as in load power, fuel consumption, and energy losses calculations. The dynamic definition is used when the model influences the up-stream of the calculation direction, and thus, is considered as a sub-model of the forward calculation [Guzzella and Sciarretta, 2007, p. 70]. This is the case, for instance, with a DC-DC converter model, since it defines an energy-storage current, whereas the ES state affects its operation. In this context, the dynamic definition does not consider the accuracy of transients. Eventually, the functional definition is used when a plant model primarily imitates operation of a sub-model, as when EM is controllable with an inverter.

The system-level simulation speed depends much on the chosen simulation time-step. The time-step of simulations is determined by the fastest dynamically modeled variable, such that the time-step should be smaller than the time-constant of such variable. In this study, the shortest modeled time-constant is τ_{AFE}, which refers to the AFE converter current response time. Therefore, the length of the simulation time-step, i.e. $t_{\mathrm{k}} - t_{\mathrm{k}-1}$, is chosen as 1 ms, where t_{k} refers to the discrete-time sample with an index k. Furthermore, the time-step should be a multiple of one in order to operate with both even and odd time-step long discrete operations, and thus the next possible option for the time-step is 10 ms, which is already too long. In addition, the time-step selection gives space for the modeling of functional characteristics of plant models, and is in the range of the computation delay of the control hardware.

It is worth noticing that according to Katrašnik et al. [2007] the accurate transient modeling of ICE needs time-steps between $1 \ldots 5 \cdot 10^{-5}$ s, which

would lead to a forward-facing model of ICE.

Fig. 2.8 shows interfaces for main elements of the proposed multi-stage modeling approach. Different powertrain structures, as presented in Section 1.2, can be built with these basic blocks. An example powertrain model that uses this modeling approach is presented in Fig. 2.9.

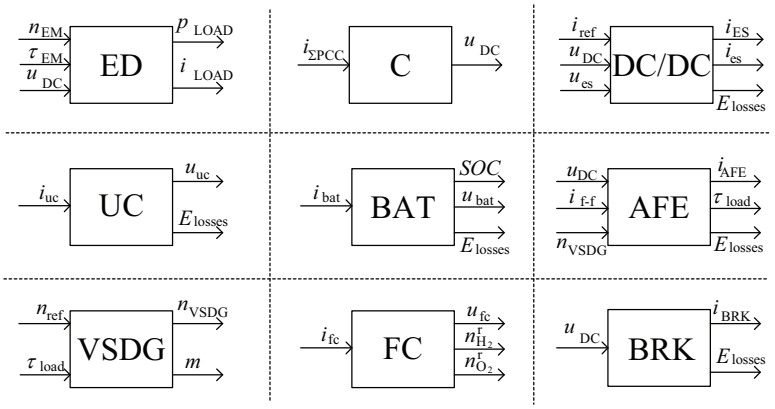

Figure 2.8. Interfaces of main blocks of a multi-stage series-hybrid powertrain simulation environment. ED = electric drive, C = capacitance of a DC bus, DC/DC = DC-DC converter, UC = ultracapacitor, BAT = battery, AFE = active front-end, VSDG = variable speed diesel generator-set, FC = fuel cell, BRK = braking-unit. Variables are explained in following sections.

2.1.3 Electric Drive Plant Model

In the presented modeling approach, the static electric drive plant model is used if the starting point for simulations is the mechanical load p_{mech}. Conversely, it is not used if the starting point is the electrical load p_{LOAD}.

Fig. 2.10 presents a measured one-quadrant efficiency map of an electric drive [Hentunen et al., 2010] for the proposed static electric drive plant model. A measured efficiency map is used to scale mechanical load to electrical. The efficiency map describes the input and output power relation of an electric drive as functions of speed and torque. This figure illustrates that the combined efficiency of an inverter and traction electric machine, in this case, reaches the 92-% efficiency in a certain operation region.

Realization of the load power scaling can be expressed, as

$$p_{\mathrm{LOAD}} = \begin{cases} p_{\mathrm{mech}} \Big/ \eta_{\mathrm{ED}}(n_{\mathrm{EM}}, \tau_{\mathrm{EM}}), & \text{if} \quad p_{\mathrm{mech}} > 0, \\ p_{\mathrm{mech}} \cdot \eta_{\mathrm{ED}}(n_{\mathrm{EM}}, \tau_{\mathrm{EM}}), & \text{if} \quad p_{\mathrm{mech}} < 0, \end{cases} \tag{2.1}$$

where power is defined as positive towards the load.

However, the presented one-quadrant efficiency map is well defined only

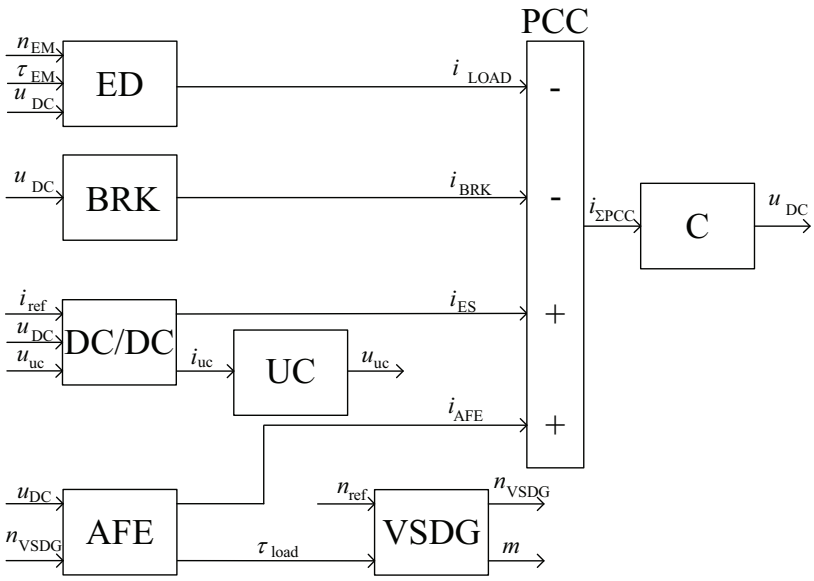

Figure 2.9. Top level of a multi-stage modeling approach for the powertrain with an engine generator-set, active rectifier, and active ultracapacitor pack. A point of common coupling is referred with PCC. Variables are explained in following sections.

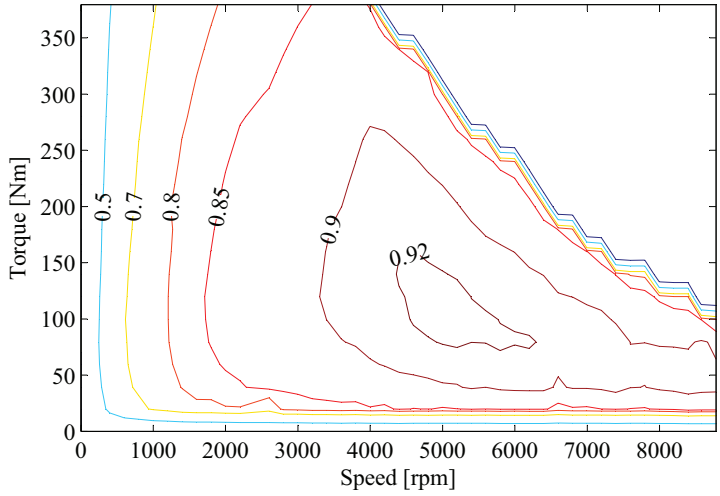

Figure 2.10. Combined measured efficiency map of Siemens *ELFA 1PV5135-4WS28* traction electric machine and *G650 D44 / 170 / 170 M7-1* inverter.

for the motoring mode operation, and mirroring the efficiency map to the generator mode operation affects the load scaling accuracy [Guzzella and Sciarretta, 2007, p. 75]. Thus, a two-quadrant efficiency mapping of an electric drive is a more convenient choice for the static ED plant model.

Furthermore, energy losses on the electric drive ($E_{\text{losses\_ED}}$) can be expressed, as

$$E_{\text{losses\_ED}} = \int_0^t (1 - \eta_{\text{ED}}) \cdot p_{\text{mech}} \cdot \mathrm{d}t. \tag{2.2}$$

In the dynamic modeling approach [Powell et al., 1998], an electric drive plant model is realized with the inverter efficiency mapping, and the dynamic equations of a specific traction motor. However, the dynamic modeling of a traction motor is not essential, if the powertrain design concentrates on power transfer from a source to loads, and does not concentrate on the traction control. Furthermore, the dynamic modeling of different electric motor types has been introduced in [Guzzella and Sciarretta, 2007, pp. 76-90].

Functionalities of the Electric Drive Plant Model

It is known that the active load can behave as the negative resistance. This behavior, in a large-signal meaning, may cause the DC-link voltage to collapse if the load power is not derated. The collapse of the DC-link voltage occurs due to saturated power transfer from energy sources or storages via DC-DC converters to the DC link. The effect can be avoided with the load power deration, which can be expressed, as

$$p_{\text{act}}(t_{\text{k}}) = \begin{cases} p_{\text{ref}}(t_{\text{k}}), & \text{if} \quad u_{\text{DC}}(t_{\text{k}-1}) \geq U_{\text{DC}}^{\text{low}}, \\ p_{\text{ref}}(t_{\text{k}}) \cdot f(u_{\text{DC}}(t_{\text{k}-1})), & \text{if} \quad U_{\text{DC}}^{\text{low}} > u_{\text{DC}}(t_{\text{k}-1}) > U_{\text{DC}}^{\text{min}}, \\ 0, & \text{if} \quad U_{\text{DC}}^{\text{min}} \geq u_{\text{DC}}(t_{\text{k}-1}). \end{cases} \tag{2.3}$$

In Eq. 2.3, p_{act} is the actual load power, and p_{ref} is the load power reference. In addition, $U_{\text{DC}}^{\text{low}}$ and $U_{\text{DC}}^{\text{min}}$ refer to a region where $f(u_{\text{DC}})$ changes, e.g., linearly from 1 to 0. That deration function can be expressed, as

$$f(u_{\text{DC}}) = \min\left[1, \max\left(0, \left(u_{\text{DC}} - U_{\text{DC}}^{\text{min}}\right) \Big/ \left(U_{\text{DC}}^{\text{low}} - U_{\text{DC}}^{\text{min}}\right)\right)\right]. \tag{2.4}$$

It is worth noticing that utilization of the proposed functionality in the ED sub-system, changes the approach from static to functional quasi-static in sense of the sub-system input interface and behavior. [Guzzella and Sciarretta, 2007, pp. 70-76]

2.1.4 DC-DC Converter Plant Model

This section proposes a modeling approach for a non-isolated multiphase interleaved bi-directional DC-DC converter, as in [Lai and Nelson, 2007], and [Hentunen et al., 2010].

The power electronic converters typically achieve very high efficiency values in their best operation area. In this context, a very high efficiency refers to a power conversion with efficiency in the range of 97...98-%. On the contrary, the efficiency of the PE converter may decrease remarkably to between 50...90-%, if an inappropriate operation area is used. The DC-DC converter modeling approach uses efficiency mapping and functional description, due to the limitations of the chosen simulation time-step (1 ms), and the need for exact full-system efficiency comparisons. The chosen simulation time-step restricts power semiconductor switching events, since modeling of the shortest semiconductor switching periods would decrease the simulation time-step to the range of 10 μs. Furthermore, a shorter time-step would make a system model unnecessarily complex, and would lead to slower full driving cycle simulation times whose total real-time lengths are in the range of 100 s to several 1000 s.

The efficiency of the DC-DC converter depends on the energy storage current i_{es}, and the voltage conversion ratio u_{ratio} that is defined, as

$$u_{\mathrm{ratio}} = u_{\mathrm{es}} / u_{\mathrm{DC}}. \tag{2.5}$$

Fig. 2.11 shows an example of the efficiency mapping of the DC-DC converter during the charge mode as functions of ES current and voltage ratio while $u_{\mathrm{DC}} = 650$ V.

The first-order function is proposed to approximate the response of the DC-DC converter current control loop. A comparison of the first-order response behavior to a PI-controlled response is presented in Eq. 2.6 and in Fig. 2.12. Furthermore, a PI-controller tuning method and parameters for the comparison are given in Eqs. 2.7...2.9, and in Table 2.1.

$$\frac{i_{\mathrm{es}}}{i_{\mathrm{es,ref}}} = \frac{1}{\tau_{\mathrm{DC/DC}} \cdot \mathrm{s} + 1} \approx \frac{K_{\mathrm{P}} \cdot \mathrm{s} + K_{\mathrm{I}}}{L \cdot \mathrm{s}^2 + (K_{\mathrm{P}} + r_{\mathrm{L}} + r_{\mathrm{es}}) \cdot \mathrm{s} + K_{\mathrm{I}}}. \tag{2.6}$$

In Eq. 2.6, K_{P} is the proportional coefficient and K_{I} is the integral coefficient of the current PI-controller. In addition, L is the choke inductance and r_{L} is the choke resistance of the DC-DC converter, and r_{es} is the ES resistance, respectively.

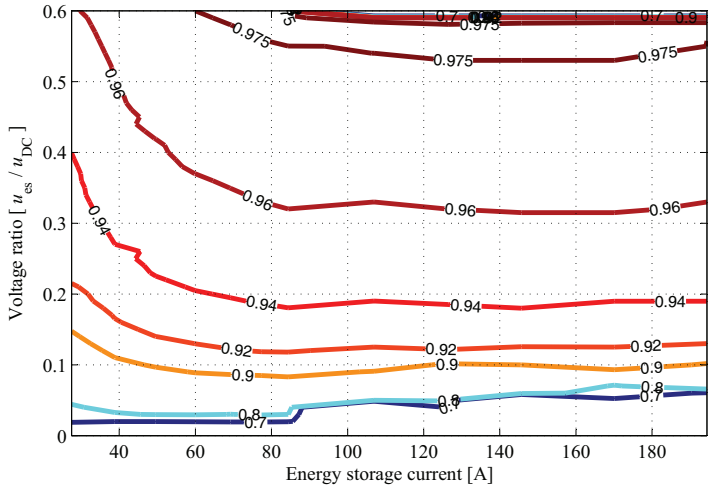

Figure 2.11. Efficiency map of a DC-DC converter in the charge operation.

In the comparison the PI-controller parameters are defined, as

$$K_{\mathrm{P}} = \alpha_{\mathrm{c}} \cdot L, \tag{2.7}$$

$$K_{\mathrm{I}} = \alpha_{\mathrm{c}}^2 \cdot L, \tag{2.8}$$

where

$$\alpha_{\mathrm{c}} = 2 \cdot \pi \cdot f_{\mathrm{c}}. \tag{2.9}$$

In Eqs. 2.7…2.9, α_{c} is the current-controller bandwidth in angular frequency [rad/s], and f_{c} is the bandwidth in frequency [1/s].

Table 2.1. Parameters for the comparison of responses.

$\tau_{\mathrm{DC/DC}}$	f_{c}	L	r_{L}	r_{es}
[ms]	[1/s]	[mH]	[mΩ]	[mΩ]
10.0	20.0	1.0	13.5[a]	70.0[b]

[a] An approximate for a choke in low-frequencies. [b] Bases on 1.1 Ω/F for UCs, 500 V potential, and to the datasheet of *BMOD0063 P125* (Maxwell Technologies Inc.). Notice that r_{es} varies depending on the type of UC, as presented by Burke and Miller [2011].

Fig. 2.12 illustrates differences between the first-order response and the PI-controlled response. The integral error (e_{Σ}) between the first-order response and the PI-controlled case is in the range of 0.5 A·s for the 100 A current transient. For example, such an error in a transient occurring once in a time-period t would cause a total error to energy transfer, as

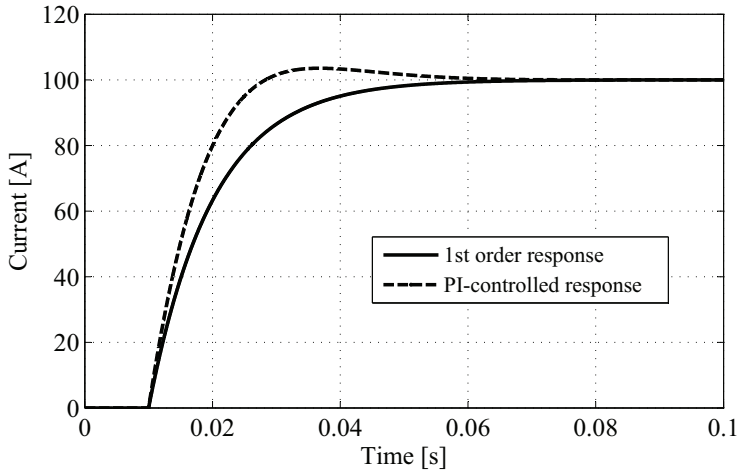

Figure 2.12. Comparison of the first-order response behavior to the PI-controlled response.

$$\frac{\Delta E_{\mathrm{es}}}{E_{\mathrm{es}}} \approx \frac{e_{\Sigma}}{i_{\mathrm{es}} \cdot t} \cdot 100\ [\%]. \tag{2.10}$$

Eq. 2.10 results to the total error value between 0.05 % to 5.0 % when t is changed from 0.1 s to 10 s. Thus, the usage of the DC-DC converter substantially affects the energy transfer accuracy of the proposed modeling method, in other words, an insignificant error occurs when a converter controls continuously constant powers. Conversely, a significant error occurs if the converter transfers transient loads. However, system integrators do not always know internal controller parameters, and therefore a practical approximation can be made with the described possible existence of an inaccuracy.

Other essential functionalities of the plant model are the minimum and maximum current limits (I_{min}, I_{max}), sub-system level proportional voltage controller, and conduction event of an upper anti-parallel diode.

The proposed approach for the DC-DC converter plant model can be expressed, as

$$i_{\mathrm{ref}} = D \cdot i_{|\mathrm{ref}|}, \qquad \text{when} \quad I_{\mathrm{min}} \leq |D| \cdot i_{|\mathrm{ref}|} \leq I_{\mathrm{max}}, \tag{2.11}$$

$$i_{\mathrm{es}} = i_{\mathrm{bat}} = i_{\mathrm{uc}} = i_{\mathrm{fc}} = i_{\mathrm{ref}}/(\tau_{\mathrm{DC/DC}} \cdot \mathrm{s} + 1), \tag{2.12}$$

$$i_{\mathrm{ES}}(t_{\mathrm{k}}) = \begin{cases} \text{while discharging, as} \\ \quad i_{\mathrm{es}}(t_{\mathrm{k}}) \cdot \eta_{\mathrm{boost}}(i_{\mathrm{es}}(t_{\mathrm{k}-1}), u_{\mathrm{ratio}}(t_{\mathrm{k}-1})) \cdot u_{\mathrm{ratio}}(t_{\mathrm{k}-1}), \\ \text{and while charging, as} \\ \quad i_{\mathrm{es}}(t_{\mathrm{k}})/\eta_{\mathrm{buck}}(i_{\mathrm{es}}(t_{\mathrm{k}-1}), u_{\mathrm{ratio}}(t_{\mathrm{k}-1})) \cdot u_{\mathrm{ratio}}(t_{\mathrm{k}-1}). \end{cases} \tag{2.13}$$

In Eq. 2.11, D (+1, 0, or -1) is the current direction of the DC-DC converter. It should be noticed that $(t_{\mathrm{k}} - t_{\mathrm{k}-1}) << \tau_{\mathrm{DC/DC}}$.

The modeling approach neglects the exact behavior of converter dynamics, and therefore, it is unclear whether "dynamic model" or "quasi-static model" should be used. However, as described by Guzzella and Sciarretta [2007, p. 70] the proposed approach fulfills the dynamic description in sense of the interface and influence on adjacent components in the system level modeling.

Furthermore, energy losses on the DC-DC converter ($E_{\mathrm{losses\_DC/DC}}$) can be expressed, as

$$E_{\mathrm{losses\_DC/DC}} = \int_0^t (1 - \eta_{\mathrm{DC/DC}}) \cdot u_{\mathrm{es}} \cdot i_{\mathrm{es}} \cdot \mathrm{d}t. \tag{2.14}$$

Control Interface of the DC-DC Converter Plant Model

The objective of the DC-DC converter is to control the current to the DC link i_{ES}. However, energy storages have operation restrictions such as a charge for ultracapacitors and batteries, and speed for flywheels.

Specifically for ultracapacitors, there is a need for the maximum and minimum voltage operation limits to avoid the over-voltage, operation in unsuitable efficiency, and limited power areas. Therefore, a deration is introduced as a limitation for a system control to prevent prohibited operations. The UC voltage deration $\alpha_{u_{\mathrm{uc}}}$ to the DC-DC converter current reference can be expressed, as

$$i_{|\mathrm{ref}|} = i_{|\mathrm{ref}'|} \cdot \alpha_{u_{\mathrm{uc}}} \tag{2.15}$$

where $\alpha_{u_{\mathrm{uc}}}$ is a piecewise defined function, for instance, while discharging and charging, as

$$\alpha_{u_{\mathrm{uc}}} = \begin{cases} \min\Big[1, \max\Big(0, \big(u_{\mathrm{uc}} - U_{\mathrm{uc}}^{\mathrm{min}}\big) \Big/ \big(U_{\mathrm{uc}}^{\mathrm{low}} - U_{\mathrm{uc}}^{\mathrm{min}}\big)\Big)\Big], \\ \min\Big[1, \max\Big(0, \big(U_{\mathrm{uc}}^{\mathrm{max}} - u_{\mathrm{uc}}\big) \Big/ \Big(U_{\mathrm{uc}}^{\mathrm{max}} - U_{\mathrm{uc}}^{\mathrm{high}}\Big)\Big)\Big]. \end{cases} \tag{2.16}$$

In Eq. 2.16, $U_{\mathrm{uc}}^{\mathrm{max}}$ and $U_{\mathrm{uc}}^{\mathrm{min}}$ are the maximum and minimum voltages of the UC pack, $U_{\mathrm{uc}}^{\mathrm{high}}$ and $U_{\mathrm{uc}}^{\mathrm{low}}$ are the ES current limitation threshold high and low voltages, respectively.

Furthermore, a static inversion of the DC-DC converter is needed in order to achieve the objective to control the DC-link current reference $i_{\mathrm{ES}'}$. The static inversion can be expressed, as

$$i_{|\mathrm{ref}'|} = \begin{cases} |i_{\mathrm{ES}'}|/(u_{\mathrm{ratio}} \cdot \eta(i_{|\mathrm{ref}|}, u_{\mathrm{ratio}})), & \text{while} \quad \text{discharging}, \\ |i_{\mathrm{ES}'}| \cdot \eta(i_{|\mathrm{ref}|}, u_{\mathrm{ratio}})/u_{\mathrm{ratio}}, & \text{while} \quad \text{charging}. \end{cases} \tag{2.17}$$

Eventually, the current control direction D can be concluded based on the sign of the $i_{\mathrm{ES}'}$.

However, the static inversion is not necessarily suitable for the low capacitance intermediate circuits due to the risk of overcompensation. That is the case−specifically, in the proposed indirect primary source power buffering in Section 2.1.11, since the overcompensation confuses the DC-link voltage PI-regulator of the AFE converter. Fig. 2.13 illustrates the cause for the problem. For instance, when i_{ES} is overcompensated, then u_{DC} becomes higher than its reference, and the AFE converter PI-regulator tries to compensate u_{DC} by transferring power to the primary source.

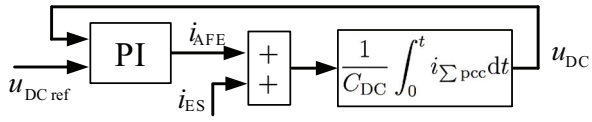

Figure 2.13. AFE converter PI-regulator sign changes if i_{ES} is overcompensated.

2.1.5 Ultracapacitor Pack Plant Model

Basic approaches are proposed for the ultracapacitor pack in the multi-stage modeling of series-hybrid powertrains.

In the basic approaches, the UC pack can be modeled with either constant or variable capacitance, and equivalent series resistance, Fig. 2.14, as

$$u_{\mathrm{uc}} = \frac{1}{C_{\mathrm{uc}}} \int_0^t i_{\mathrm{uc}} \mathrm{d}t - R_{\mathrm{uc}} i_{\mathrm{uc}} + U_{\mathrm{uc\_initial}}. \tag{2.18}$$

The mapping of a variable capacitance, as functions of current and voltage, can be expressed by a fitted polynomial function, as

$$\mathbf{C}_{\mathrm{uc}}(i_{\mathrm{uc}}, u_{\mathrm{uc}}) = p_{00} + p_{10} i_{\mathrm{uc}} + p_{01} u_{\mathrm{uc}}. \tag{2.19}$$

Usually, R_{uc} is considered as a constant quantity, although it is dependent on temperature and voltage whose effects to the resistance can be augmented to the model if data is available [Shi and Crow, 2008]. The polynomial fitting of a capacitance introduces the mean RMS error of 0.34

F with coefficients: $p_{00} = 14.42$, $p_{10} = -0.006072$, and $p_{01} = 0.01938$, for a *BMOD0018 P390* (17.8 F, 390 V, Maxwell Technologies Inc.) UC module.

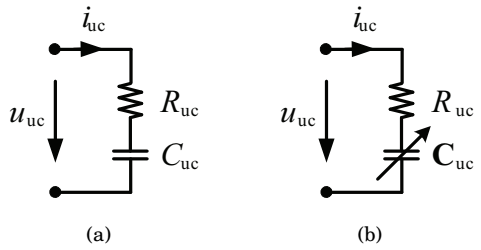

Figure 2.14. Simple ultracapacitor model with either: (a) constant; or (b) variable capacitance and constant series resistance.

The energy losses on the UC pack can be expressed, as

$$E_{\text{losses\_uc}} = R_{\text{uc}} \int_0^t i_{\text{uc}}^2 \mathrm{d}t. \tag{2.20}$$

The energy content for the weight, size, and cost calculations of the UC pack is calculated as,

$$E_{\text{uc}} = \frac{C_{\text{uc}} \cdot U_{\text{max}}^2}{2}, \tag{2.21}$$

where U_{max} is the maximum voltage of the ultracapacitor pack.

The advantage of these basic approaches is on the computational simplicity [Shi and Crow, 2008]. Eq. 2.18 is considered as dynamic in system level models, or forward models, due to its influence to the upstream of the power-flow calculation direction [Guzzella and Sciarretta, 2007]. It should be understood that the term dynamic does not refer to transient responses for which the UC has different modeling approaches. Such dynamic models are covered in Section 2.2.2.

Fig. 2.15 shows the local efficiency of ESS for the static modeling of the UC based systems. Such a static model can be implemented, e.g., with a look-up table, for a backward-facing calculation. Section 2.1.1 describes equipment under test.

Capacitor Plant Model

The low-capacitance intermediate circuit voltage, i.e. the DC-link voltage, can be expressed, as

$$u_{\text{DC}} = \frac{1}{C_{\text{DC}}} \int_0^t i_{\sum \text{PCC}} \mathrm{d}t - R_{\text{DC}} i_{\sum \text{PCC}} + U_{\text{DC\_initial}}, \tag{2.22}$$

where C_{DC} is the DC-link capacitance, $i_{\sum \text{PCC}}$ is the sum current on a point of common coupling, and R_{DC} is the equivalent series resistance of

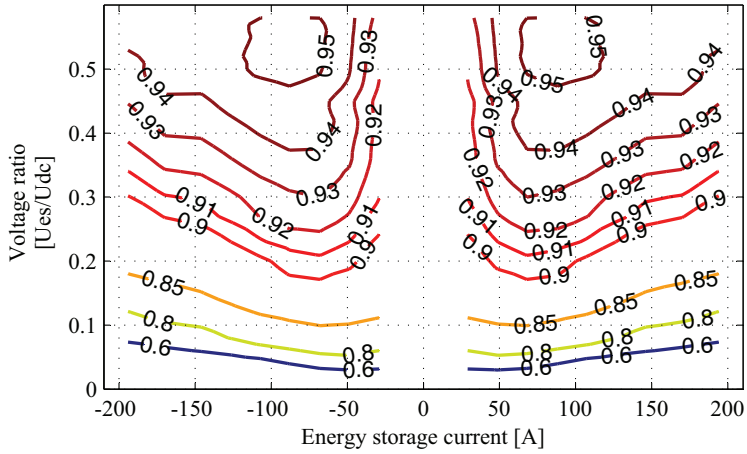

Figure 2.15. Two-quadrant efficiency map of ESS consisting of a DC-DC converter and UC module.

DC-link capacitors. The DC-link resistance might be excluded due to its minor importance.

2.1.6 Battery Pack Plant Model

Various types of battery models can be found in the literature. At least, names of black box, electric circuit, electrochemical, experimental, mathematical, and stochastic models are used to describe battery models [Chen and Rincón-Mora, 2006; Dong et al., 2011; Einhorn et al., 2013; Tremblay et al., 2007]. Descriptions are partly overlapping due to a good reason, i.e., models are often some kind of combinations of different approaches.

Many authors [Chen and Rincón-Mora, 2006; Dong et al., 2011; Einhorn et al., 2013] claim that electric circuit models are the most useful to represent electrical characteristics of batteries in vehicles. These models can be mainly classified to three main categories: Thevenin, Impedance, and Runtime-based models. Chen and Rincón-Mora [2006] categorizes these models and proposes a blended version of the Thevenin and Runtime-based models.

Next, this section proposes the Shepherd model for use in the multi-stage modeling of series-hybrid powertrains. The dynamic battery models, Thevenin- and Impedance-based models are introduced in Section 2.2.3.

Shepherd Model

The goal of this model is to help determination of the minimum weight or volume for batteries. The model was originally introduced by Shep-

herd [1965] and developed by Tremblay et al. [2007] for use in Mathworks [2013] products to represent charge/discharge curves of different battery chemistries. The model is adaptable to a wide range of charge/discharge data.

According to Dong et al. [2011], the Shepherd model is a black box model which, in Mathworks [2013], is implemented to the Thevenin circuit. In this context, the black-box model refers to exclusion of the underlying physiochemical processes. On the contrary, gray-box models refer to electrical circuit models. This model is not recommended, according to Dong et al. [2011], for alternative energy storage, electric, and hybrid vehicle applications which are not usually operated at quasi-stationary conditions.

The main feature of the Shepherd model is that parameters can be extracted from a discharge curve. Thus, the model has several assumptions in its form introduced by Tremblay et al. [2007]. The internal resistance is supposed to be constant, charge characteristics are assumed to be the same as for discharge, capacity of the battery is not dependent on the amplitude of current, i.e. no Peukert effect, temperature has no effect, no self-discharge, and no memory effect. A natural conclusion is that this model has a value only in the early phase of the design process.

In this approach, discharge characteristics, i.e. when $i^* > 0$, of the Li-ion battery pack is modeled, as

$$u_{\mathrm{bat}}(it, i^*, i_{\mathrm{bat}}) = U_0 - K\frac{Q}{Q - it}i^* - K\frac{Q}{Q - it}it + Ae^{-B \cdot it} - R_{\mathrm{bat}} \cdot i_{\mathrm{bat}}, \quad (2.23)$$

and charge characteristics, i.e. when $i^* < 0$, as

$$u_{\mathrm{bat}}(it, i^*, i_{\mathrm{bat}}) = U_0 - K\frac{Q}{it + 0.1 \cdot Q}i^* \ldots$$

$$\ldots - K\frac{Q}{Q - it}it + Ae^{-B \cdot it} - R_{\mathrm{bat}} \cdot i_{\mathrm{bat}}. \quad (2.24)$$

In Eqs. 2.23 and 2.24, u_{bat} is the nonlinear output voltage, $it = \int_0^t i^* \mathrm{d}t$ is the extracted capacity where $i^* = H(s) \cdot i_{\mathrm{bat}}$ is the low-frequency current dynamics and the first-order low-pass filter $H(s)$ represents the battery voltage dynamics, i_{bat} is the battery current, U_0 is the maximum voltage value of the linear area, K is the polarization constant, Q is the maximum battery capacity, A is the exponential voltage, B is the exponential capacity, and R_{bat} is the battery resistance.

The battery resistance depends on several factors, such as temperature, state-of-charge, and age of the battery. Thus, manufacturer data-sheets

do not always give any value for battery resistances. For such cases Tremblay et al. [2007] propose use of an experiment based estimate value for the battery resistance. The proposed resistance is constant and represents the correct resistance in only the measured operation point, and thus includes an error in every other operation point. The battery resistance can be calculated as,

$$R_{\mathrm{bat}} = (1 - \eta_{\mathrm{bat}}) \frac{U_{\mathrm{nom}}}{\mathrm{C}}, \tag{2.25}$$

where η_{bat} is the battery efficiency with the nominal battery current C, and U_{nom} is the minimum voltage of the battery pack in the linear area.

One approach is to use the 99-% efficiency estimate for batteries [Mathworks, 2013], or even 99.5 % [Tremblay et al., 2007], which are moderate assumptions for resistive losses as can be noticed from the article by Burke and Miller [2011]. In other words, these estimates mean the $0.5 \ldots 1$ % power losses on the battery pack with the 1C value for the both charge and discharge conditions. While applying this approach to a high-power battery one should use the continuous current, e.g. 4C, instead of the nominal current 1C. This assumes thermal conduct of power losses for the high-power battery pack to be equal with the high-energy battery pack.

It is worth noticing that, according to Einhorn et al. [2013], a look-up table parametrization with respect to a linear parameter of the resistance has only a minor impact to the accuracy of voltage in battery models, although this model can be augmented with the varying resistance if data as given by Burke and Miller [2011] is available.

The energy losses on the battery pack can be expressed, as

$$E_{\mathrm{losses\_bat}} = R_{\mathrm{bat}} \int_0^t i_{\mathrm{bat}}^2 \mathrm{d}t. \tag{2.26}$$

The energy content E_{bat} for the weight, size, and cost calculations of the battery pack is calculated, as

$$E_{\mathrm{bat}} = \frac{U_0 + U_{\mathrm{nom}}}{2} Q. \tag{2.27}$$

2.1.7 Active Front-end Converter and Generator Plant Model

This section proposes a functional quasi-static approach for a plant model of an active front-end converter and generator combination—specifically, for series-hybrid powertrains with a low-capacitance intermediate circuit. A different type of modeling approach comes into question depending on

the topology of the hybrid system. For instance, Powell et al. [1998] proposed a functional method in which the converter output current is empirically defined based on speed, field current, and output voltage of a generator, and by the field current first-order dynamics, for a hybrid powertrain with a passive battery in an intermediate circuit.

The active-front-end converter, i.e., an inverter in the voltage control mode, and generator sub-system model can be realized with the efficiency mapping in the torque-speed plane, and with the DC-link voltage PI-regulator that controls the DC current to the intermediate circuit. The energy losses of power conversion from the DC link to the engine shaft are taken into account as in Eqs. 2.1 and 2.2, and Fig. 2.10 presents. The DC-link voltage regulator type, and parameter values, affect the realization of power transfer from the primary source.

In general, the plant model contains the DC-link voltage PI-regulator, and the feed-forward value $i_{\mathrm{f-f}}$ that is the difference between the load current and ESS current, as $i_{\mathrm{f-f}} = i_{\mathrm{LOAD}} - i_{\mathrm{ES}}$. The impact of $i_{\mathrm{f-f}}$ was assessed by Lidozzi and Crescimbini [2012]. Furthermore, the error term e_{u} for the PI-regulator is defined, as $e_{\mathrm{u}} = u_{\mathrm{DCref}} - u_{\mathrm{DC}}$.

The current reference before the limitations is defined, as

$$i_{\mathrm{ref}'}(t_{\mathrm{k}}) = i_{\mathrm{f-f}} + K_{\mathrm{P}} e_{\mathrm{u}} + K_{\mathrm{I}} \int_0^t \left[e_{\mathrm{u}} + K_{\mathrm{aw}} (i_{\mathrm{ref}}(t_{\mathrm{k}-1}) - i_{\mathrm{ref}'}(t_{\mathrm{k}-1})) \right] \mathrm{d}t, \quad (2.28)$$

where t_{k} is the time index, K_{P} and K_{I} are the PI-regulator coefficients, and K_{aw} is the anti-windup coefficient.

The current reference $i_{\mathrm{ref}'}$ must be limited to prevent stall and overspeed of the engine. Therefore, the current reference with the maximum and minimum limitations, is defined as

$$i_{\mathrm{ref}}(t_{\mathrm{k}}) = \begin{cases} i_{\mathrm{max}}(n_{\mathrm{G}}), & \text{if} \quad i_{\mathrm{ref}'}(t_{\mathrm{k}}) \geq i_{\mathrm{max}}(n_{\mathrm{G}}), \\ i_{\mathrm{ref}'}(t_{\mathrm{k}}), & \text{if} \quad i_{\mathrm{max}}(n_{\mathrm{G}}) > i_{\mathrm{ref}'}(t_{\mathrm{k}}) > i_{\mathrm{min}}(n_{\mathrm{G}}), \\ i_{\mathrm{min}}(n_{\mathrm{G}}), & \text{if} \quad i_{\mathrm{min}}(n_{\mathrm{G}}) \geq i_{\mathrm{ref}'}(t_{\mathrm{k}}), \end{cases} \quad (2.29)$$

where $i_{\mathrm{max}}(n_{\mathrm{G}})$ is the dynamic maximum current limit, and $i_{\mathrm{min}}(n_{\mathrm{G}})$ is the dynamic minimum current limit, respectively.

The dynamic maximum current limit can be described, as

$$i_{\mathrm{max}}(n_{\mathrm{G}}) = \vec{I}_{\mathrm{max}}(n_{\mathrm{G}}) - P(n_{\mathrm{G_{ref}}} - n_{\mathrm{G}}), \quad (2.30)$$

where the static maximum DC current vector $\vec{I}_{\mathrm{max}}(n_{\mathrm{G}})$ is derived from the maximum power limit $P_{\mathrm{e}}(n_{\mathrm{e}})$ of the engine. The load limitation decreases proportionally if the generator speed n_{G} fails to meet the reference $n_{\mathrm{G_{ref}}}$.

The purpose of the dynamic maximum current limit is to prevent stalling of the engine.

The dynamic minimum current limit can be described, as

$$i_{\min}(n_{\mathrm{G}}) = P(n_{\mathrm{G}} - n_{\mathrm{G_{max}}}), \tag{2.31}$$

where $n_{\mathrm{G_{max}}}$ is the maximum allowed speed, and the P-regulator limits the regenerative load to the engine shaft, and thus, prevents overspeed. The dynamic minimum current limit can have a value between zero to $I_{\min}$ which is a negative value, and derived based on the maximum parasitic shaft load. It is used to enable the regenerative braking to the engine shaft when the DC-link voltage arises over the reference, and the engine speed is low enough for the regenerative braking.

Eventually, the DC-link current of the AFE converter is defined, as

$$i_{\mathrm{AFE}} = i_{\mathrm{ref}}/(\tau_{\mathrm{AFE}} \cdot \mathrm{s} + 1), \tag{2.32}$$

where τ_{AFE} is the current control delay time-constant of the AFE-converter-generator combination. Therefore, the load torque $\boldsymbol{\tau}_{\mathrm{load}}$ for the engine can be derived from the DC-link current (i_{AFE}), as

$$\boldsymbol{\tau}_{\mathrm{load}} = \begin{cases} i_{\mathrm{AFE}} \cdot u_{\mathrm{DC}}/(\eta_{\mathrm{ED}}(n_{\mathrm{G}}, \boldsymbol{\tau}_{\mathrm{req}}) \cdot \omega_{\mathrm{G}}), & \text{if} \quad i_{\mathrm{AFE}} \geq 0, \\ i_{\mathrm{AFE}} \cdot u_{\mathrm{DC}} \cdot \eta_{\mathrm{ED}}(n_{\mathrm{G}}, \boldsymbol{\tau}_{\mathrm{req}})/\omega_{\mathrm{G}}, & \text{if} \quad 0 > i_{\mathrm{AFE}}. \end{cases} \tag{2.33}$$

In Eq. 2.33, $\eta_{\mathrm{ED}}(n_{\mathrm{G}}, \boldsymbol{\tau}_{\mathrm{req}})$ is the efficiency mapping of the electric drive, which consists of the permanent magnet machine and the AFE converter. ω_{G} is the generator angular speed, and $\boldsymbol{\tau}_{\mathrm{req}}$ is the requested torque, as $\boldsymbol{\tau}_{\mathrm{req}} = i_{\mathrm{AFE}} \cdot u_{\mathrm{DC}}/\omega_{\mathrm{G}}$.

Energy losses on the AFE-converter-generator combination can be calculated, as

$$E_{\mathrm{losses\_AFE\_gen}} = \int_0^t (1 - \eta_{\mathrm{ED}}) \cdot u_{\mathrm{DC}} \cdot i_{\mathrm{AFE}} \cdot \mathrm{d}t. \tag{2.34}$$

2.1.8 Diesel Engine Plant Model

The diesel engine modeling is an essential part of the powertrain design. The engine modeling can be very complicated due to the complexity and various subsystems of an engine [Powell et al., 1998]. However, more generalized fuel consumption mapping based engine models exist in order to decrease the amount of model parameters and their complexity.

Tsai and Goyal [1986] presented a fuel consumption mapping based quasi-linear dynamic diesel engine model, which is suitable for testing the adequacy of its controller under all operating conditions. Such a model is based on knowledge of output torque as functions of fuel injection and speed.

Although, the quasi-linear dynamic model is known and its construction is relatively simple, more simplified first and second-order torque response functions are proposed for modeling of diesel engine dynamics. In such cases, fuel consumption is derived based on experimental mapping of fuel consumption with different torque and speed [Syed et al., 2006]. The advantage of the latest model is that torque response and fuel consumption mapping can be experimentally tested for any engine, with no knowledge needed of fuel injection dependency to output torque.

In general, the diesel engine plant model includes Newton's second law for rotational dynamics, as

$$\omega_{\mathrm{VSDG}} = \frac{1}{J_{\mathrm{tot}}} \int_0^t (\boldsymbol{\tau}_{\mathrm{e}} - \boldsymbol{\tau}_{\mathrm{load}}) \cdot \mathrm{d}t + \omega_{\mathrm{VSDG\_initial}}. \tag{2.35}$$

In Eq. 2.35, J_{tot} is the inertia of the VSDG shaft, which includes both the inertia of the diesel engine and generator. ω_{VSDG} is the angular speed of the variable speed diesel generator-set.

The VSDG is controlled with the speed reference and therefore, the subsystem PI-controller for speed is defined, as

$$e_{\mathrm{n}} = n_{\mathrm{VSDG\_ref}} - n_{\mathrm{VSDG}}, \tag{2.36}$$

$$\dot{m}' = K_{\mathrm{P}} \cdot e_{\mathrm{n}} + K_{\mathrm{I}} \int_0^t e_{\mathrm{n}} \cdot \mathrm{d}t, \tag{2.37}$$

$$\dot{m} = \begin{cases} \vec{M}_{\max}(n_{\mathrm{VSDG}}), & \text{if} \quad \dot{m}' \geq \vec{M}_{\max}(n_{\mathrm{VSDG}}), \\ \dot{m}', & \text{if} \quad \vec{M}_{\max}(n_{\mathrm{VSDG}}) > \dot{m}' > 0, \\ 0, & \text{if} \quad 0 \geq \dot{m}'. \end{cases} \tag{2.38}$$

In Eqs. 2.36…2.38, e_{n} is the error term of the speed reference and the actual value, $\dot{m}'$ is the unlimited fuel injection output value of the speed PI-controller, and $\vec{M}_{\max}(n_{\mathrm{VSDG}})$ is the maximum fuel quantity vector as a function of the VSDG speed. The $\vec{M}_{\max}(n_{\mathrm{VSDG}})$ defines the maximum torque curve for the diesel engine. The output $\dot{m}$ is the actual fuel quantity value [mg/stroke]. Furthermore, the model uses the change rate limiter for the speed reference.

The fuel consumption *m* of the engine can be expressed, as

$$m = K \int_0^t n_{\mathrm{VSDG}} \cdot \dot{m} \cdot \mathrm{d}t, \tag{2.39}$$

where the coefficient K is *piston amount / stroke cycle*.

The engine torque follows a nonlinear torque function of injected fuel and engine speed with a time delay that varies in length by the time between successive engine firings. The torque response delay for the four-stroke cycle, the six-cylinder high speed engine, can be expressed, as

$$\boldsymbol{\tau}_{\mathrm{e}} = \frac{\boldsymbol{\tau}_{\mathrm{map}}}{0.65 \cdot \tau_{\mathrm{e}} \cdot \mathrm{s} + 1}, \tag{2.40}$$

where the time-constant τ_{e} is given, as

$$\tau_{\mathrm{e}} = 20/n_{\mathrm{VSDG}}. \tag{2.41}$$

Fig. 2.16 presents the torque data $\boldsymbol{\tau}_{\mathrm{map}}$ for the turbocharged diesel engine as a mapping of speed, and fuel quantity per stroke. The torque mapping presented in this figure refers to the brake torque which is the indicated torque minus the parasitic losses of the water pump, fuel pump, oil pump, valve train, air filter, muffler, piston rings, and crank bearings [Tsai and Goyal, 1986].

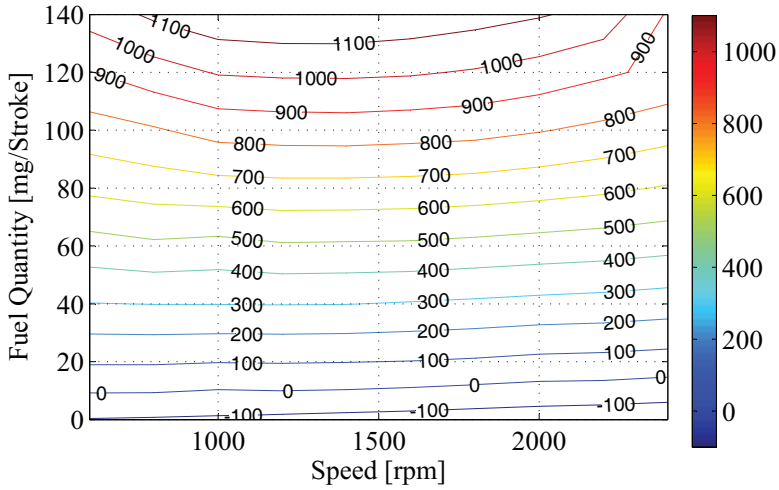

Figure 2.16. Torque data as a mapping of fuel quantity and speed of the engine.

The torque mapping can be expressed with a polynomial function of speed and fuel quantity. The surface fitting can be done with a surface fitting tool to achieve coefficients for the surface function, as

$$\begin{aligned} \boldsymbol{\tau}_{\mathrm{map}}(n_{\mathrm{VSDG}}, \dot{m}) \;=\; & p_{00} + p_{10} \cdot n_{\mathrm{VSDG}} + p_{01} \cdot \dot{m} \\ & + p_{20} \cdot n_{\mathrm{VSDG}}^2 + p_{11} \cdot n_{\mathrm{VSDG}} \cdot \dot{m} + p_{02} \cdot \dot{m}^2 \\ & + p_{30} \cdot n_{\mathrm{VSDG}}^3 + p_{21} \cdot n_{\mathrm{VSDG}}^2 \cdot \dot{m} + p_{12} \cdot n_{\mathrm{VSDG}} \cdot \dot{m}^2. \end{aligned} \tag{2.42}$$

The coefficients of Eq. 2.42 are presented in Table 2.2. The RMS error of the surface function with respect to data is 13.4 Nm.

Table 2.2. Coefficients for the surface polynomial function of torque data .

Coefficients	Value
p_{00}	-39.28
p_{10}	-0.06109
p_{01}	6.34
p_{20}	$-1.092{\cdot}10^{-5}$
p_{11}	$5.736{\cdot}10^{-3}$
p_{02}	$-3.565{\cdot}10^{-3}$
p_{30}	$6.791{\cdot}10^{-9}$
p_{21}	$-1.602{\cdot}10^{-6}$
p_{12}	$-7.244{\cdot}10^{-6}$

2.1.9 Fuel Cell Source Plant Model

This study proposes use of a static *ui*-curve model for a FC-stack. The FC-stack is modeled as a current-dependent voltage source, hence $u_{\mathrm{fc}} = \mathrm{f}(i_{\mathrm{fc}})$, where u_{fc} is the output voltage of the FC-stack, and i_{fc} is the FC-stack current, as well as the low-voltage side current of the boost converter. The fuel cell stack *ui*-curve imitates the output voltage, i.e., the polarization curve of a typical commercial fuel cell stack, which is usually given by a FC manufacturer. The polarization curve can be imitated with a look-up table.

Furthermore, hydrogen and oxygen consumption calculations are needed for the powertrain design. The rates of conversion, i.e. utilizations, of hydrogen $u_{\mathrm{fH_2}}$ and oxygen $u_{\mathrm{fO_2}}$ are determined in [Mathworks, 2013], as

$$u_{\mathrm{fH_2}} = \frac{n^{\mathrm{r}}_{\mathrm{H_2}}}{n^{\mathrm{in}}_{\mathrm{H_2}}} = \frac{R \cdot T \cdot N \cdot i_{\mathrm{fc}}}{Z \cdot F \cdot P_{\mathrm{fuel}} \cdot V_{lpm(\mathrm{fuel})} \cdot x\%}, \tag{2.43}$$

$$u_{\mathrm{fO_2}} = \frac{n^{\mathrm{r}}_{\mathrm{O_2}}}{n^{\mathrm{in}}_{\mathrm{O_2}}} = \frac{R \cdot T \cdot N \cdot i_{\mathrm{fc}}}{2 \cdot Z \cdot F \cdot P_{\mathrm{air}} \cdot V_{lpm(\mathrm{air})} \cdot y\%}. \tag{2.44}$$

In the above equations, $n^{\mathrm{r}}_{\mathrm{H_2}}$ is the relieved hydrogen, and $n^{\mathrm{in}}_{\mathrm{H_2}}$ the hydrogen input, as well as $n^{\mathrm{r}}_{\mathrm{O_2}}$ is the relieved air, and $n^{\mathrm{in}}_{\mathrm{O_2}}$ is the air input, respectively. In addition, R is the gas constant and equals to 8.3145 J/(mol·K), T is the operation temperature, and N is the number of cells.

Parameter Z refers to the number of moving electrons per mole of fuel, i.e., 2 for a single hydrogen$-$oxygen fuel cell reaction, as

$$2\mathrm{H_2} + \mathrm{O_2} \rightarrow 2\mathrm{H_2O},$$

but for multiple reactions it becomes an experimental decimal value, e.g., 2.967 for PEM FC of 6 kW at 45 V in Simulink$^{\mathrm{TM}}$ models [Mathworks, 2013]. Furthermore, F is the Faraday constant, i.e. 96485 A·s/mol, P_{fuel} is the fuel absolute supply pressure (atm), P_{air} is the air absolute supply pressure (atm), $V_{lpm(\mathrm{fuel})}$ is the fuel flow rate (l/min), $V_{lpm(\mathrm{air})}$ is the air flow rate (l/min), x is the percentage of hydrogen in the fuel, and y is the percentage of oxygen in the oxidant.

2.1.10 Brake Resistor and Chopper Plant Model

This section describes a functional modeling approach of a brake resistor and chopper, i.e. a braking unit, in a low capacitance intermediate circuit. Based on the knowledge attained, modeling of a braking-unit in vehicle powertrain systems has not been recently discussed in the literature. However, other possibilities to model the braking-unit would be electrical circuit modeling with either ideal or non-ideal power semiconductor switches, or also by functionally with a constant voltage operation limit.

In any case, the braking-unit modeling method should not affect a system level simulation time-step, and thus, electrical circuit modeling is unviable. A method with only a constant voltage operation limit would assume unlimited power capabilities in the braking-unit, and furthermore, it adds a computational discontinuity due to a state change in an intermediate circuit variable, i.e. the DC-link voltage. Thus, the proposed functional modeling method can be considered as more suitable than the constant value with a state change.

The braking unit is used to prevent an excessive increase of voltage in low capacitance intermediate circuits. Functionality of the braking unit can be described, e.g. as

$$i_{\mathrm{BRK}}(t_{\mathrm{k}}) = \begin{cases} K_{\mathrm{P}} \cdot e_{\mathrm{u}}(t_{\mathrm{k}-1}) + K_{\mathrm{I}} \int_0^t e_{\mathrm{u}}(t_{\mathrm{k}-1}) \cdot \mathrm{d}t, & \dots \\ \quad \dots \text{if} \quad u_{\mathrm{DC}}(t_{\mathrm{k}-1}) > U_{\mathrm{DC}}^{\mathrm{brake}}, \\ \quad 0, \dots \\ \quad \dots \text{if} \quad U_{\mathrm{DC}}^{\mathrm{brake}} \geq u_{\mathrm{DC}}(t_{\mathrm{k}-1}). \end{cases} \tag{2.45}$$

In Eq. 2.45, i_{BRK} is the braking-unit current, e_{u} is the voltage error between $U_{\mathrm{DC}}^{\mathrm{brake}}$ and u_{DC}, as well as K_{P} and K_{I} are due to functional modeling of a braking-unit. Furthermore, a power limitation saturates excessive values of i_{BRK}.

2.1.11 Energy Management Algorithm for the Hybrid Control Mode

This section proposes an indirect primary source power buffering method for use in the active ultracapacitor buffered diesel series-hybrid powertrains. The method was used for validations of plant models in Figs. 2.5...2.6. The indirect power buffering, in this context, means the low capacitance intermediate circuit regulation with the AFE converter, while the DC-DC converter averages the load. On the contrary, the direct power buffering refers to the low capacitance intermediate circuit regulation with the DC-DC converter, while the primary source is controlled based on the averaged load.

A scheme of the proposed series-hybrid powertrain energy management is presented in Fig. 2.17. The control signals and actual values are the speed reference n_{ref} for the VSDG electronic control unit, the DC-link voltage reference for the AFE converter $u_{\mathrm{DC\_ref}}$, the UC pack voltage u_{uc}, the DC-link voltage u_{DC}, the current reference $i_{|\mathrm{ref}|}$ and direction D for the DC-DC converter, as well as the load power p_{LOAD}.

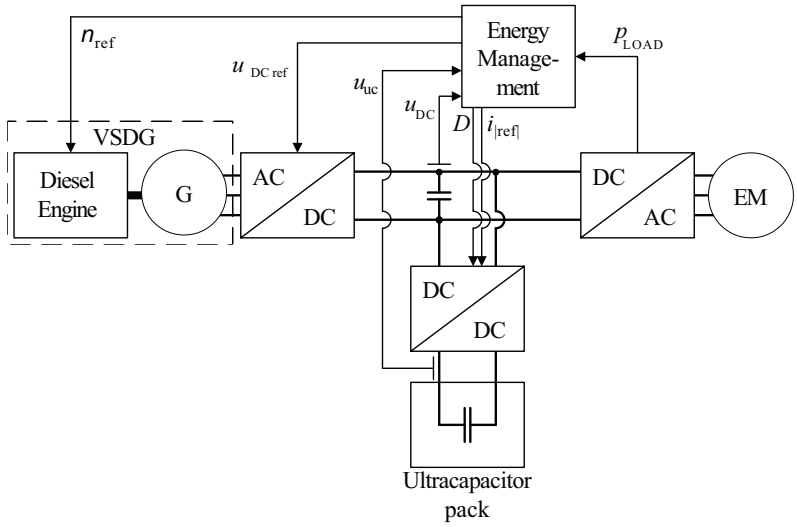

Figure 2.17. Energy management hierarchy of the series-hybrid powertrain with the ultracapacitor pack for power buffering.

Control of the Energy Storage System in the Series-Hybrid Powertrain

In general, the ESS control design can be started on the ESS current to the DC link (i_{ES}), since the DC-link current relation to the energy storage current can be expressed as in Eq. 2.17. Control of ESS depends on

the whole powertrain control strategy and therefore, one general solution does not exist.

Control of the ES System in the Plant Model Validation Experiment

The energy management algorithm has two parallel regulators. First, the P-regulator from the DC-link voltage, as

$$i_{\mathrm{ES'\_1}} = P(u_{\mathrm{DC\_ref}} - u_{\mathrm{DC}}). \tag{2.46}$$

Second, the filter structure based on coefficients ($b_0 ... b_\mathrm{n}$) of a moving average function with values 1/(n + 1), i.e., a discrete-time finite impulse response (FIR) filter. The study uses the 20-second averaging period with 0.1 s time-steps. The output of the FIR filter is, as

$$p_{\mathrm{FIR}}(t_\mathrm{k}) = \sum_{t_\mathrm{i}=t_{\mathrm{k-n}}}^{t_\mathrm{k}} [p_{\mathrm{LOAD}}(t_\mathrm{i})/(n+1)] \tag{2.47}$$

$$u_{\mathrm{FIR}}(t_\mathrm{k}) = 2 - \frac{p_{\mathrm{FIR}}(t_\mathrm{k})}{P_{\mathrm{MAX}}},$$

where t_k is the present time index and t_i refers to time indices of the filter from $t_{\mathrm{k-n}}$ to t_k. $n = 199$ is the amount of unit delays in the filter. P_{MAX} is the tuning parameter of the energy management algorithm which is, e.g., 2...3 times the maximum primary source power. The output of the FIR filter is multiplied with the power reference for the primary source u_P that in the validation case is expressed, as

$$u_\mathrm{P}(t_\mathrm{k}) = P_{\mathrm{MAX}}\left(1 - \frac{u_{\mathrm{uc}}(t_\mathrm{k})}{U_{\mathrm{max}}}\right). \tag{2.48}$$

Furthermore, the filter output p_{filter} is piecewise determined, as

$$p_{\mathrm{filter}}(t_\mathrm{k}) = \begin{cases} u_{\mathrm{FIR}}(t_\mathrm{k}) \cdot u_\mathrm{P}(t_\mathrm{k}), & \text{if } u_{\mathrm{FIR}}(t_\mathrm{k}) \cdot u_\mathrm{P}(t_\mathrm{k}) > 0, \\ 0, & \text{if } 0 \geq u_{\mathrm{FIR}}(t_\mathrm{k}) \cdot u_\mathrm{P}(t_\mathrm{k}). \end{cases} \tag{2.49}$$

This prevents the negative output of the filter. Therefore, all regenerative load power is included in the filter output and subtracted from the actual load power of the DC link. The power regulator output is, as

$$i_{\mathrm{ES'\_2}} = \frac{p_{\mathrm{LOAD}} - p_{\mathrm{filter}}}{u_{\mathrm{DC}}}. \tag{2.50}$$

Thus, the ES system current reference on the DC-link voltage potential can be expressed, as

$$i_{\mathrm{ES'}} = i_{\mathrm{ES'\_1}} + i_{\mathrm{ES'\_2}}. \tag{2.51}$$

The sign of $i_{\mathrm{ES'}}$ determines the current control direction D.

The stability of the ES system control algorithm can be studied by deriving $i_{\mathrm{ES}'}$ with all its inputs. The ES system current reference space on a static state is presented in Fig. 2.18 with the $u_{\mathrm{DC\_ref}}$ value of 650 V, u_{DC} 600 V...700 V, P-regulator coefficient of 2, and p_{LOAD} between P_{MAX} to $-P_{\mathrm{MAX}}$, i.e., 100 kW...−100 kW. The static current reference space is the worst case in sense of the filter output, since the maximum output occurs only if the maximum input lasts long enough.

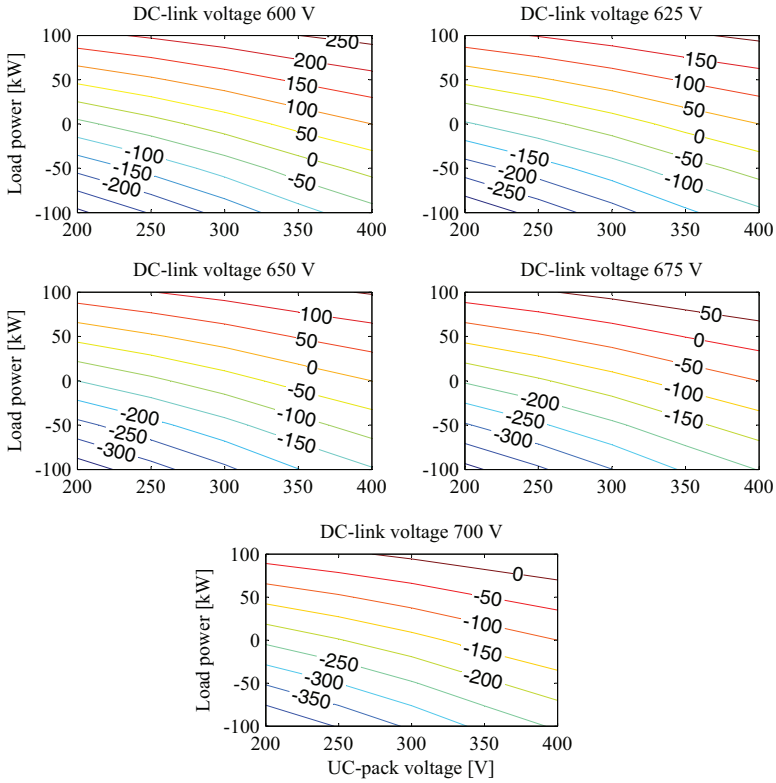

Figure 2.18. Static ES system current reference $i_{\mathrm{ES}'}$ space presented in five piecewise charts with all inputs.

The current reference space shows how parallel regulators affect the ES system current. With the high load, the full energy storage voltage, and the low DC-link voltage, the ES system gets the highest positive reference. On the contrary, the highest negative reference is given with the low ES voltage, the high regenerative load, and the high DC-link voltage. The positive linear function, described in Eq. 2.49, makes impossible negative output values of the filter and therefore, the negative load power weights the current reference towards negative values. The power buffering is performed based on the load power level and the ES voltage with the

weighting depended on the DC-link voltage.

Rule-Based Speed Control for VSDG in the Series-Hybrid Powertrain

The variable speed diesel generator-set can be forced to operate on the minimum fuel consumption per kilowatt-hour area, with co-operation of the VSDG speed control, and the AFE converter control, as Ceraolo et al. [2008] discussed. The rule-based speed control for VSDG can be expressed, e.g. as

$$n_{\text{e\_ref}} = \begin{cases} n_{\text{e\_max}}, & \text{if} \quad p_{\text{AFE}} > P_{\text{lim\_max}}, \\ \vdots & \vdots \\ n_{\text{e\_1}}, & \text{if} \quad P_{\text{lim\_2}} > p_{\text{AFE}} > P_{\text{lim\_1}} + P_{\text{hyst}}, \\ n_{\text{e\_idle}}, & \text{if} \quad P_{\text{lim\_1}} \geq p_{\text{AFE}}, \end{cases} \tag{2.52}$$

which defines engine speed references depending on its load. In Eq. 2.52; $n_{\text{e\_idle}}$, $n_{\text{e\_1}}$, ..., $n_{\text{e\_max}}$ refer to different speed references for the engine; $P_{\text{lim\_1}}$, $P_{\text{lim\_2}}$, ..., $P_{\text{lim\_max}}$ refer to different power limits between speed reference transitions; P_{hyst} is the hysteresis between power transition limits; and p_{AFE} is the AFE converter power, as $i_{\text{AFE}} \cdot u_{\text{DC}}$. Simulated Fig. 2.19 illustrates the operation areas where the VSDG operation can be forced. Crowded operation point areas represent specific static speed ($n_{\text{e\_idle}}, n_{\text{e\_1}}, ..., n_{\text{e\_max}}$) values, and scattered operation points are due to transitions between static speed states.

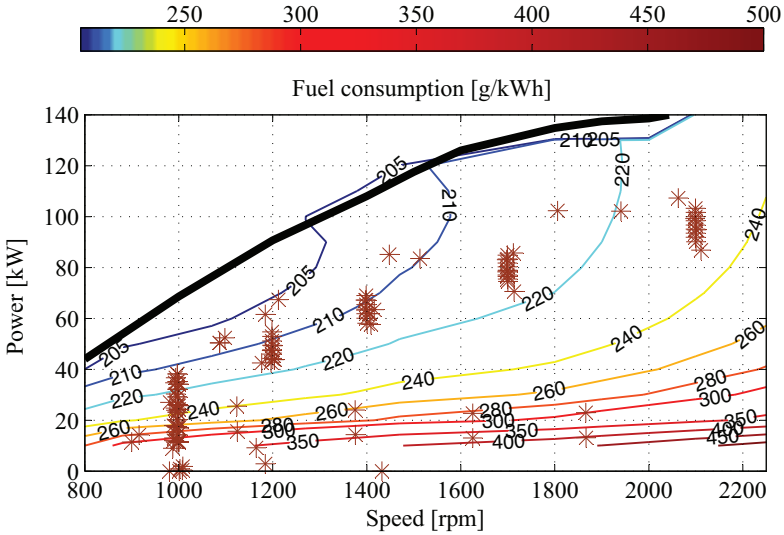

Figure 2.19. Operation points of an engine in the variable speed use on the fuel consumption map. Operation points are marked with stars, and the maximum power limit with a wide line.

The proposed rule-based speed control for an engine is not suitable for all types of loading. For instance, an engine might overload due to an abrupt high load step. Such a load can occur in a vehicle suddenly stopping and re-starting traction while already moving. On the other hand, the proposed engine speed control is suitable for loading which is ramped up during a longer time-period. Fig. 2.20 illustrates changes of operation areas with the proposed rule-based speed controller for an engine. This figure shows how static speed states are changed with high torque values to higher speeds, and, on the contrary, with low or regenerative torque values to lower speeds. Arrows illustrate change directions of speed states.

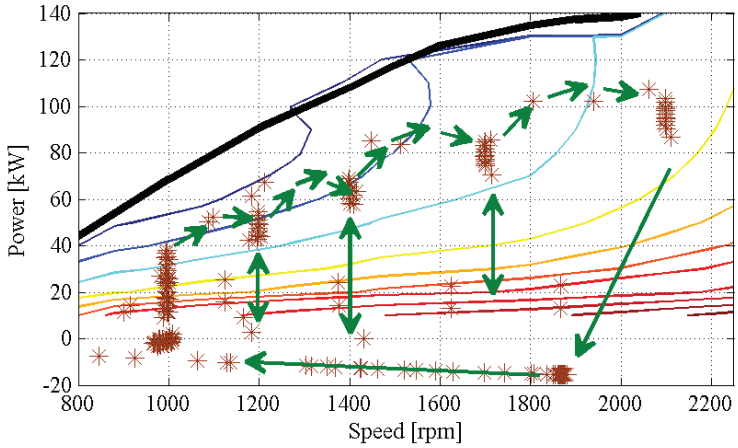

Figure 2.20. Operation principle of an engine with the proposed rule-based speed control.

The context of the proposed speed control is based on an idea of using an engine with predetermined constant speeds on the low fuel consumption area, rather than using an engine with continuously varying speed, e.g., from 1000 rpm to 2100 rpm.

2.2 Dynamic Modeling of Series-Hybrid Powertrains

Dynamic modeling is required for the control and the stability analysis of a system. In power electronics, this means application of nonlinear time-domain models, or small-signal models, which are averaged over a switching cycle of a nonlinear model. Electric circuit models are a usual choice to represent dynamics of energy storages. Primary sources, such as engine and fuel cell, are commonly, in high-power applications, interfaced with power conversion devices, and thus they are often modeled as power electronic devices.

In HP power electronic applications, such as NRMM powertrains, an insulated gate bipolar transistor (IGBT) technology is commonly used. The switching frequency of the IGBT technology is limited due to relatively high switching losses, and therefore it is common that devices using IGBTs operate with low switching frequencies, i.e. 1...20 kHz. Switching-cycle averaged models are valid up to around the switching frequency [Maksimović, 2000] if two samples per switching period are taken, and therefore the switching frequency plays an essential role in the fidelity of other powertrain component models.

Our contribution to the dynamic modeling of series-hybrid powertrains is on a systematic approach for the dynamic modeling of multiport DC buses in power-electronic systems. This approach is valid up to the vicinity of the resonance of the DC-bus capacitor. This resonance frequency is often well above the switching frequency, especially when the IGBT technology is assumed. Thus, this approach is convenient, specifically, for the dynamic modeling of power-electronic systems with the IGBT technology.

Next sections will introduce dynamic modeling of other powertrain components such as load and source models, ultracapacitor models, and battery models. The dynamic modeling of diesel engines and fuel cell sources are not introduced due to wideness of these topics. As stated in forthcoming sections dynamics of sources are applied if the need arises during the development of powertrains.

2.2.1 Load and Source Models

Traditionally, nonlinear models of regulated DC or AC loads have been first averaged over the switching cycle and then linearized for small-signal analysis purposes. The small-signal stability has been studied by means of linearized models, which are typically expressed in a form of state-space

representations or transfer functions. Next sections introduce briefly some aspects of nonlinear time-domain and small-signal modeling.

Nonlinear time-domain models

Three approaches for time-domain models are discussed in following paragraphs. These approaches are a current source, changeover switch, and state-space model of an inverter or switching converter.

A basic approach, used by Sudhoff et al. [1998]; Pietiläinen et al. [2006], is to model a three-phase AC load with a power-controlled current source. Such an approach focuses on the DC-link dynamics and targets to the frequency bandwidth from the tens to hundreds of hertz. However, Sudhoff et al. [1998] states that this approach is intended for explanation purposes and for guidance in designing control algorithms, not for high-fidelity simulation or for the testing of control algorithms. Furthermore, according to Mosskull et al. [2007] this approach assumes the torque control to be perfect and thus leads to false conclusions in some operation points.

A more complex approach is to model a three-phase AC load by three ideal changeover switches. Such a nonlinear time-domain model can be implemented to an electric circuit simulator. This advanced modeling approach becomes complex since the control of the system needs to be strictly implemented, and thus leads to variance in approaches which some are highlighted in following.

In the advanced modeling of drives, the system and control dynamics are usually taken into account into some extent. In the approach of Liutanakul et al. [2010], all dynamics of a drive except delays in the control algorithms of an inverter are taken into account. Mosskull et al. [2007] considers also non-idealities of the control such as the sampling and pulse-width modulator delays. However, Liutanakul et al. [2010] states that non-idealities of the control are often neglected in practical applications, which might be due their low influence and the complexity of implementation. In any case, linearization of these models can proceed with state-space representations or transfer functions.

Maksimović [2000] stated that switching converters could be modeled as analytical models if implemented to switched piecewise linear systems and some simplifying assumptions are considered. The analytical piecewise linear system approach results to a good accuracy at all frequencies, and could be implemented without an electric circuit simulator. Thus, the state-space representation of a circuit is more straightforward to the

small-signal analysis.

Small-signal models

The small-signal stability analysis requires linearized models of a source and load. Usually, the product of the source impedance and the load admittance are assessed with some stability criterion. For instance, the Nyquist criterion have been used to analyze the small-signal stability in Mosskull et al. [2007]; Liutanakul et al. [2010]; and in Wallmark et al. [2012]. Alternatively, the local stability has been analyzed based on the eigenvalues of the linearized system in Sudhoff et al. [1998].

Maksimović [2000] proposes a method for the automated generation of small-signal models based on time-domain models. The reasoning for such a method is that there are often circuit configurations, control methods, or operating modes where appropriate small-signal models are not available or are difficult to derive. Application of this method is demonstrated with use of *PSpice* and *Mathematica*.

Puukko et al. [2011] showed that the inverter dynamics can be predicted with a current-fed boost-type converter model, when the d-axis current, i.e. current transferring the real power, is considered. This simplifies the dynamic small-signal network model of a three-phase inverter from fifteen transfer functions to six.

Wallmark et al. [2012] derived the converter input admittance for salient permanent-magnet synchronous machine drives with the field-oriented current control. Furthermore, time-domain experiments and Nyquist-diagram analysis are presented.

In small-signal analysis, it is common that dynamics of rotating machines, i.e., a generator coupled to an engine or a motor to a wheel, are neglected due to their long time constants caused by inertia [Sudhoff et al., 1998; Wallmark et al., 2012]. However, some work as Liutanakul et al. [2010] are done by considering all dynamics of a drive.

2.2.2 Dynamic Ultracapacitor Models

According to Shi and Crow [2008] three basic ultracapacitor modeling approaches exist, such as mathematical, electric circuit, and other non-electric circuit models, e.g. an artificial neural network model. Electric circuit models are commonly a natural choice of electrical engineers for dynamic modeling. These electric circuit models can be categorized into different types from which four are illustrated in Fig. 2.21.

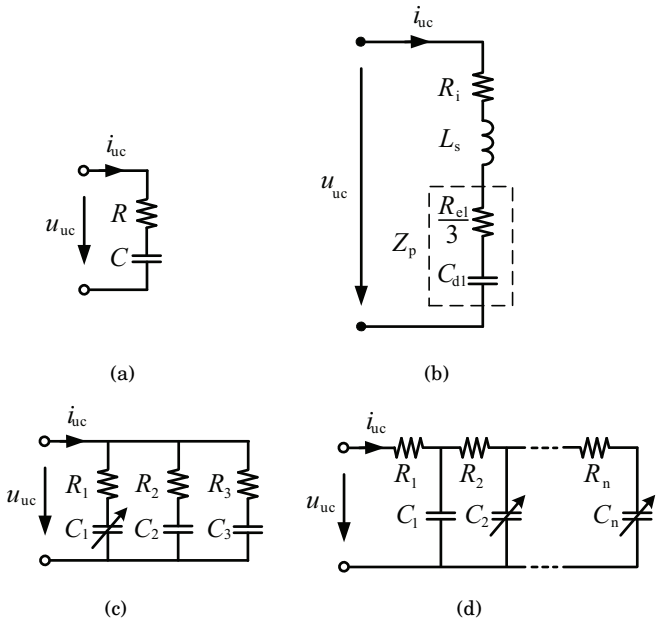

Figure 2.21. (a) Simple series-RC model, (b) impedance model, (c) parallel-RC branches model, (d) RC-transmission line model.

The simple series-RC model approach, in Fig. 2.21(a), describes charge and discharge of UC with constant or varying values of a resistance and capacitance. The advantage of this approach is computational simplicity. However, this approach is not able to capture the nonlinear rise and fall of the UC voltage and the change in voltage after the charging and discharging stops as stated by Zubieta and Bonert [2000].

The simple series-RC model approach can be augmented to the impedance model shown in Fig. 2.21(b) which consists of the ohmic resistance R_i, the series inductance L_s, and the pore impedance Z_p with the double-layer capacitance C_dl and the electrolyte resistance R_el. The impedance model was fitted to measurements in the frequency range of 0.2... 70 Hz, and compared to a drive-cycle long verification measurements with this fitting in Buller [2003]. In his work, the range of 14... 44-% accuracy for the UC-module power dissipation were concluded with the comparison time of 30 minutes, and with fixed environment and target parameters. Furthermore, the voltage accuracy of $\pm$ 0.5 % of the nominal were reported.

The parallel-RC model approach, in Fig. 2.21(c), targets to capture the nonlinear rise and fall of the UC voltage after charge or discharge, and furthermore aims to describe sufficiently the UC voltage in the 30-

minutes period. In approach of Zubieta and Bonert [2000], the parallel-RC model is suggested to be used with three well distinct RC time constants covering the desired time range, such as in Fig. 2.21(c) R_1 and C_1 refer to the fast-term time constant, R_2 and C_2 refer to the medium-term time constant, and R_3 and C_3 refer to the long-term time constant. The shortest time-constant branch is suggested to be realized with a variable capacitance, whereas others are suggested to be constants. In addition, Zubieta and Bonert [2000] suggest a procedure to determine the required model parameters from terminal measurements.

The RC-transmission line model, in Fig. 2.21(d), is based on work by de Levie in the 1960s [Buller, 2003; Shi and Crow, 2008]. This model simulates UCs physical structure and electrochemical characteristics directly. In UC, each pore in a porous electrode can be modeled as a transmission line, thus leading to a ladder network with many RC elements. Lajnef et al. [2007] show that a modification of the RC-transmission line model can be fitted to the UC impedance in the 0.01... 1000-Hz frequency range. In their approach, R_1 in Fig 2.21(d) corresponds to the magnitude of the measured impedance at the resonance frequency. Furthermore, C_1 and $R_2 \ldots R_{\mathrm{n}}$ are constants whereas $C_2 \ldots C_{\mathrm{n}}$ are dependent on voltage. A good fit of the model is suggested to be reached when n is between 4 and 20.

The impedance of UC is purely capacitive only with low frequencies. The phase of the impedance turns from capacitive to inductive in the 0.01... 1000-Hz frequency range [Lajnef et al., 2007], while the resonance frequency is found in the 70... 200-Hz frequency range [Buller, 2003; Lajnef et al., 2007]. Naturally, the exact resonance frequency is dependent on the series inductance of UC, and thereby dimensions of a circuit.

As introduced, there are different electric circuit models for more accurate modeling of an ultracapacitor behavior. However, such models need parameter extraction from experimental tests, and their use might affect system-level simulation time-steps. Implementation and need of these approaches as a part of a system-level model is, on my best knowledge, an open question.

2.2.3 Dynamic Battery Models

Fig 2.22 illustrates two main categories for the dynamic modeling of a battery. These approaches, Thevenin and impedance-based electric circuit models, are discussed in next sections.

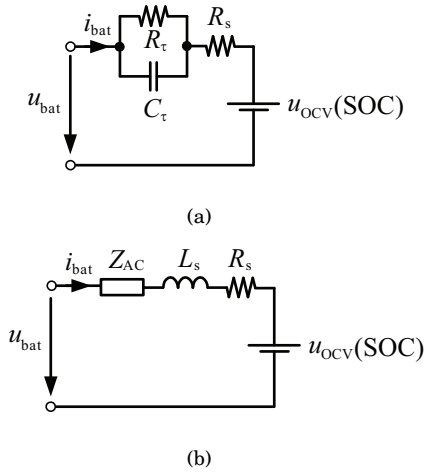

Figure 2.22. (a) Thevenin, (b) impedance-based electric circuit battery models.

Thevenin-based Model

A generic Thevenin-based electric circuit model is shown in Fig. 2.22(a), where the voltage-controlled voltage source $u(\mathrm{SOC})$ represents the open-circuit voltage (OCV) as function of SOC, R_s is the series resistance, and R_τ and C_τ are the transient resistance and capacitance, respectively.

Thevenin-based models can predict the battery voltage during a relevant discharge cycle with the accuracy range of 1.5...5.0 % [Chen and Rincón-Mora, 2006; Einhorn et al., 2013]. The Thevenin circuit with an additional series RC-branch introduces the AC response to the battery model, thus improving the transient response of voltage with respect to the circuit with OCV and series resistance. The accurate use of these models assumes knowledge of OCV dependency on SOC, temperature condition, and current rate.

According to Einhorn et al. [2013] use of more than one RC-branch for transients will not introduce any significant benefit to the modeling of the voltage, if static operation conditions of a battery are assumed to be known. Furthermore, this approach models the capacitive transient behavior of a Li-ion battery from 1 Hz to the 0.3...2.0-kHz range [Dong et al., 2011; Buller, 2003].

Naturally, a more accurate transient fit on this medium frequency region affects to the whole drive-cycle simulation time.

Impedance-based Model

A generic impedance-based electric circuit model is shown in Fig. 2.22(b), where L_s is the series inductance and Z_AC is the AC impedance. Usually,

this AC impedance consists of complex RC networks whose parameters are extracted by the electrochemical impedance spectroscopy technique [Buller, 2003; Dong et al., 2011].

This approach enables fit of the battery impedance to a model e.g. from 0.1-mHz to 65-kHz frequency region, i.e., the approach augments the impedance to low frequencies below 1 Hz and to high frequencies over the 0.3...2.0-kHz frequency region. However, the battery impedance is dependent on, at least, factors such as SOC and battery current [Buller, 2003], and therefore the impedance measurement of a battery to various stationary states becomes a very time consuming task.

The introduction of an inductive part of the battery impedance, i.e., the frequency region over 0.3...2.0-kHz, is not suitable for the whole drive cycle simulations. Instead, this modeling approach has value in stability analyses of a system.

2.3 Error Analysis

This section introduces calculation of the maximum error values with the partial differential equation. Then, the partial differential equation is used to solve the efficiency mapping accuracy of the DC-DC converter, and cumulative maximum errors of the multi-stage modeling method that is introduced in Section 2.1. Finally, gained knowledge is applied to the parameter sensitivity analysis based on the Monte Carlo method.

2.3.1 Maximum Measurement Error

Generally, the maximum error of a variable ΔF can be calculated with the partial differential equation, as

$$\Delta F = \left|\frac{\delta F}{\delta x_1}\right|\Delta x_1 + \left|\frac{\delta F}{\delta x_2}\right|\Delta x_2 \ldots + \left|\frac{\delta F}{\delta x_\mathrm{n}}\right|\Delta x_\mathrm{n}, \tag{2.53}$$

where F is the function of the variable, x_n is the n^{th} factor of the function F, and Δx_n is the error value for the n^{th} factor.

Discussions of Accuracies in DC-DC Converter Efficiency Mapping
Eq. 2.53 can be written to describe the maximum error of the efficiency measurement $\Delta\eta$, as

$$\Delta\eta = \left|\frac{\delta\eta}{\delta u_\mathrm{out}}\right|\Delta u_\mathrm{out} + \left|\frac{\delta\eta}{\delta i_\mathrm{out}}\right|\Delta i_\mathrm{out} + \left|\frac{\delta\eta}{\delta u_\mathrm{in}}\right|\Delta u_\mathrm{in} + \left|\frac{\delta\eta}{\delta i_\mathrm{in}}\right|\Delta i_\mathrm{in}, \tag{2.54}$$

where

$$\eta = \frac{u_\mathrm{out}\cdot i_\mathrm{out}}{u_\mathrm{in}\cdot i_\mathrm{in}},$$

thus

$$\Delta\eta = \frac{i_\mathrm{out}}{u_\mathrm{in}\cdot i_\mathrm{in}}\Delta u_\mathrm{out} + \frac{u_\mathrm{out}}{u_\mathrm{in}\cdot i_\mathrm{in}}\Delta i_\mathrm{out} + \frac{u_\mathrm{out}\cdot i_\mathrm{out}}{u_\mathrm{in}^2\cdot i_\mathrm{in}}\Delta u_\mathrm{in} + \frac{u_\mathrm{out}\cdot i_\mathrm{out}}{u_\mathrm{in}\cdot i_\mathrm{in}^2}\Delta i_\mathrm{in}.$$

In these equations, the out and in subscripts refer to variables on different sides of a DC-DC converter.

In efficiency measurements, the used power analyzer was *Norma D6100* (LEM) with its triaxial shunts for 6...300 A currents. The measuring accuracy for voltage channels in the 0...15-Hz frequency range is ± (0.15 + 0.03) % for reading and range, respectively. The measuring accuracy for current shunts in the 0...100-kHz frequency range is ± 0.1 %. Furthermore, measurements were taken at the 70-kHz sampling frequency, and averaged over the time-period of one second. Table 2.3 illustrates voltage measurement accuracies depending on the operation point of ESS.

Table 2.3. Voltage measurement maximum errors in different operation points.

	reading [V]	range [V]	error [V]	error [%]
u_{es}:	200	340	$\pm$ 0.402	$\pm$ 0.201
u_{es}:	380	670	$\pm$ 0.771	$\pm$ 0.203
u_{DC}:	650	670	$\pm$ 1.176	$\pm$ 0.181

Table 2.4 illustrates efficiency measurement accuracies on four operation points. This table shows the measured values of current and voltage, and based on this table we can conclude that the total maximum error of the efficiency mapping is in the range of $\pm$ 0.47... 0.52 %, cf. error values with superscripts a. The total maximum error is a value for a case when all error components cumulate to the same direction.

Table 2.4. Efficiency measurement maximum errors in different operation points.

u_{out} [V]	i_{out} [A]	u_{in} [V]	i_{in} [A]	$\Delta\eta$ [%]
254.8	29.2	650.4	12.2	$\pm$ 0.505
379.7	29.57	650.4	17.99	$\pm$ 0.467[a]
256.7	194.4	650.3	79.5	$\pm$ 0.519[a]
369.3	194.6	650.2	113.3	$\pm$ 0.478

In practice, the efficiency mapping needs a look-up table with a high number of cells, e.g. 531 cells in our use. Thus, it is common to fit a polynomial function to represent such a data set as the efficiency mapping. However, the measured efficiency mapping is nonlinear, and therefore, introduction of a polynomial function for the efficiency surface creates an RMS error. The introduced error is dependent on the degree of a polynomial function which can be expressed, e.g., for the efficiency of the DC-DC converter, as

$$\begin{aligned}\eta(i_{\mathrm{es}}, u_{\mathrm{ratio}}) \;=\; & p_{00} + p_{10}\cdot i_{\mathrm{es}} + p_{01}\cdot u_{\mathrm{ratio}} \\ & + p_{20}\cdot i_{\mathrm{es}}^2 + p_{11}\cdot i_{\mathrm{es}}\cdot u_{\mathrm{ratio}} + p_{02}\cdot u_{\mathrm{ratio}}^2 \\ & + \ldots \\ & + p_{\mathrm{i}0}\cdot i_{\mathrm{es}}^{\mathrm{i}} + p_{(\mathrm{i}-1)(\mathrm{j}-1)}\cdot i_{\mathrm{es}}^{\mathrm{i}-1}\cdot u_{\mathrm{ratio}}^{\mathrm{j}-1}\ldots \\ & \ldots + p_{(\mathrm{i}-1)(\mathrm{j}-2)}\cdot i_{\mathrm{es}}^{\mathrm{i}-1}\cdot u_{\mathrm{ratio}}^{\mathrm{j}-2} + \ldots \\ & \ldots + p_{(\mathrm{i}-2)(\mathrm{j}-1)}\cdot i_{\mathrm{es}}^{\mathrm{i}-2}\cdot u_{\mathrm{ratio}}^{\mathrm{j}-1} + p_{0\mathrm{j}}\cdot u_{\mathrm{ratio}}^{\mathrm{j}}.\end{aligned} \tag{2.55}$$

In Eq. 2.55, p_{ij} refers to a coefficient of the polynomial function, and in-

dices i and j define the degree of the surface function.

Table 2.5 illustrates decrease of the root-mean-square error (RMSE), and increase of the coefficient number, as functions of degree numbers of the surface polynomial. A RMS value closer to zero indicates a fit that is more useful for predictions. RMSE is defined, as

$$\mathrm{RMSE} = \sqrt{\mathrm{E}\Big((\hat{\eta} - \eta)^2\Big)}, \tag{2.56}$$

where $\mathrm{E}(X)$ is the mean of X that is a group of values, $\hat{\eta}$ is the estimated efficiency with a polynomial function, and η is the measured efficiency. $\hat{\eta}$ and η refer to various points of surfaces.

Table 2.5. Polynomial fittings for the efficiency surface within u_{ratio} of 0.07 ... 0.59.

RMS error [%]	coefficients	i	j
1.27	3	1	1
1.15	5	2	1
0.92	5	1	2
0.76	6	2	2
0.60	9	2	3
0.55	12	2	4
0.53	15	2	5
0.44	14	3	4
0.41[a]	18[b]	3	5
0.39	20	4	5
0.39	21	5	5

Furthermore, introduced RMS errors change if a polynomial function is defined only for a bounded region where most of converter operation occurs, i.e., a linear region of the efficiency map. These errors are illustrated in Table 2.6 within the voltage conversion range of 0.3. . .0.59.

Table 2.5 highlights that the introduced RMS error by a polynomial function is, e.g., 0.4 % if the whole efficiency surface is estimated, cf. the RMS error with the superscript a. Table 2.6 highlights that this error decreases to the 0.08-% range if only the linear region of the mapping is estimated, cf. a. These values refer to the cases with 12 and 18 coefficients for the definition of the polynomial function, cf. b in both tables.

To conclude, an efficiency mapping, if measured only once, has the total maximum error of $\pm$ 0.47. . . 0.52 %. In practice, the total error limits would decrease if efficiency measurements would be repeated. Furthermore, if the whole efficiency mapping would be estimated with the sur-

Table 2.6. Polynomial fittings for the efficiency surface within u_{ratio} of 0.3 ... 0.59.

RMS error [%]	coefficients	i	j
0.59	3	1	1
0.33	5	2	1
0.59	5	1	2
0.33	6	2	2
0.16	9	3	2
0.33	9	2	3
0.078[a]	12[b]	4	2
0.073	15	5	2

face polynomial function, then the total maximum error would increase, for instance, to $\pm$ 0.9 %, as stated in Table 2.5, or to $\pm$ 0.55...0.6 % (Table 2.6) if only the linear region of the mapping is estimated.

Thus, in the early phase of research it is convenient to use only a look-up table based efficiency mapping for the plant model of a DC-DC converter. If measurements of the DC-DC converter efficiency would be repeated, then, for instance, a surface polynomial function for the linear region of the mapping could be considered as an option to target a low total maximum error, e.g., in the range of $\pm$ 0.2 %. This would mean the target of $\pm$ 0.122 % for the efficiency measurement accuracy.

In addition, the average of RMS errors between charge and discharge modes in a specific operation point is $\pm$ 0.3 %, when the efficiency data is compared in the current i_{es} range of 30... 196 A and the voltage ratio u_{ratio} of 0.2... 0.6. The average RMS error becomes $\pm$ 0.2 % when u_{ratio} is within 0.3...0.6. Thus, for more accurate energy transfer calculations, there is a need for different mappings of the charge and discharge modes. The parameter sensitivity analysis, in Section 2.3.5, can be used to conclude the importance of efficiency measurements to powertrain variables.

Cumulative Maximum Errors of the Proposed Modeling Method

The concept of the maximum error calculation can be extended for calculation of cumulative maximum errors of the modeling method. This, however, is noticed to be more complex than analyzing only one data mapping, or analyzing variable errors in a system with, e.g., Monte Carlo method, see sections 2.3.2... 2.3.5.

The target is to achieve an accurate fuel consumption estimate, as $\Delta \dot{m}$. Therefore, the proposed model is piecewise differentiated in relation to all

conceivable parameters. Strictly speaking, the presented accuracy analysis considers only the static-state accuracies, and neglects accuracies in transients. The target to concentrate on the static accuracy gives an assumption that all errors for variables controlled with an integral term become equal to a measurement error.

Depending on the starting point of the simulation, the static error analysis begins either on p_{mech} or p_{LOAD}. If p_{mech} is chosen, then speed and torque of traction motors are considered to be known accurately. If p_{LOAD} is considered to be known, then the starting point is on intermediate circuit side variables of hoist and traction drives.

According to Eq. 2.53, the accuracy of an electric drive efficiency mapping η_{ED} can be written, as

$$\Delta\eta_{\mathrm{ED}} = \left|\frac{\delta\eta_{\mathrm{ED}}}{\delta\boldsymbol{\tau}_{\mathrm{EM}}}\right|\Delta\boldsymbol{\tau}_{\mathrm{EM}} + \left|\frac{\delta\eta_{\mathrm{ED}}}{\delta\omega_{\mathrm{EM}}}\right|\Delta\omega_{\mathrm{EM}} + \left|\frac{\delta\eta_{\mathrm{ED}}}{\delta u_{\mathrm{in}}}\right|\Delta u_{\mathrm{in}} + \left|\frac{\delta\eta_{\mathrm{ED}}}{\delta i_{\mathrm{in}}}\right|\Delta i_{\mathrm{in}}, \quad (2.57)$$

where

$$\eta_{\mathrm{ED}} = \frac{\boldsymbol{\tau}_{\mathrm{EM}} \cdot \omega_{\mathrm{EM}}}{u_{\mathrm{in}} \cdot i_{\mathrm{in}}},$$

thus

$$\Delta\eta_{\mathrm{ED}} = \frac{\omega_{\mathrm{EM}}}{u_{\mathrm{in}} \cdot i_{\mathrm{in}}}\Delta\boldsymbol{\tau}_{\mathrm{EM}} + \frac{\boldsymbol{\tau}_{\mathrm{EM}}}{u_{\mathrm{in}} \cdot i_{\mathrm{in}}}\Delta\omega_{\mathrm{EM}} + \frac{\boldsymbol{\tau}_{\mathrm{EM}} \cdot \omega_{\mathrm{EM}}}{u_{\mathrm{in}}^2 \cdot i_{\mathrm{in}}}\Delta u_{\mathrm{in}} + \frac{\boldsymbol{\tau}_{\mathrm{EM}} \cdot \omega_{\mathrm{EM}}}{u_{\mathrm{in}} \cdot i_{\mathrm{in}}^2}\Delta i_{\mathrm{in}}.$$

Table 2.7 gives accuracies for the efficiency mapping sensors. The accuracy of the torque sensor is the datasheet value of *Dataflex 42 / 1000* (KTR). The speed encoder in the measurement was *CKS36-PFBPROGR* with 1024 pulses per revolution. The speed measurement has the accuracy of $\pm$ 0.01 % of reading, according to *Norma D6100* (LEM) datasheet, for a measuring period over 30 ms. Electrical measurement accuracies are based on the *Norma D6100* (LEM) datasheet. The accuracy of u_{in} is according to reading and range accuracies for 650 V. The accuracy of i_{in} is according to the basic accuracy of external triaxial shunts.

Table 2.7. Measurement sensor accuracies for the efficiency mapping of an electric drive.

$\boldsymbol{\tau}_{\mathrm{EM}}$ error [Nm]	n error [%]	u_{in} error [%]	i_{in} error [%]
$\pm$ 5	$\pm$ 0.01	$\pm$ 0.181	$\pm$ 0.1

Table 2.8 illustrates measurement accuracies of the efficiency mapping of ED with low speed (30 rpm) at 1.0 kW shaft power, and with high speed (3000 rpm) at 100 kW shaft power.

Table 2.8. Efficiency mapping accuracies of an electric drive with low and high speeds, and motoring and regenerative powers.

τ_{EM} [Nm]	ω_{EM} [rad/s]	u_{in} [V]	i_{in} [A]	$\Delta\eta_{\mathrm{ED}}$ [%]
+ 318.3	+ 3.141	+ 650	+ 7.692	$\pm$ 0.372
− 318.3	+ 3.141	+ 650	− 0.308	$\pm$ 9.31[a]
+ 318.3	+ 314.1	+ 650	+ 181	$\pm$ 1.58[b]
− 318.3	+ 314.1	+ 650	− 130.8	$\pm$ 2.19[b]

Maximum errors of the efficiency mapping remain high, due to a high error in torque measurement which covers approximately 84 % of the maximum error, cf. with Eq. 2.57 and values of Tables 2.7 and 2.8. The worst presented error in efficiency mapping accuracies is $\pm$ 9.31 %, cf. the value with the superscript a in Table 2.8, and it refers to the case when low mechanical power is transferred to the intermediate circuit. Impact of this is negligible, since the high error at low powers has low impact to the full cycle cumulative error value because cumulating of small powers results to small energies. In other words, more dominant maximum error value examples during the full drive cycle analysis are, e.g., $\pm$ 1.58 % and $\pm$ 2.19 %, cf. values with superscripts b.

The cumulative error in energy losses of ED is,

$$\Delta E_{\mathrm{losses\_ED}} = \int_0^t \Delta\eta_{\mathrm{ED}} \cdot p_{\mathrm{mech}} \mathrm{d}t, \tag{2.58}$$

thus, integral of $\Delta\eta_{\mathrm{ED}}$ determines directly the error percentage in $E_{\mathrm{losses\_ED}}$.

The accuracy of p_{LOAD} can be written, as

$$\Delta p_{\mathrm{LOAD}} = \left| \frac{\delta p_{\mathrm{LOAD}}}{\delta \eta_{\mathrm{ED}}} \right| \Delta\eta_{\mathrm{ED}} = \begin{cases} p_{\mathrm{mech}} \cdot \Delta\eta_{\mathrm{ED}} \Big/ \eta_{\mathrm{ED}}^2, & \text{if} \quad p_{\mathrm{mech}} > 0, \\ p_{\mathrm{mech}} \cdot \Delta\eta_{\mathrm{ED}}, & \text{if} \quad p_{\mathrm{mech}} < 0. \end{cases} \tag{2.59}$$

Table 2.9 presents accuracies of p_{LOAD} with motoring and regenerating powers, both, with low speed at 1.0 kW power, and with high speed at 100 kW power. The results illustrate that the absolute error values of p_{LOAD} are dependent on the p_{mech} magnitude, and therefore, the relative errors change depending on the sign of the load power.

The worst presented relative error $\Delta p_{\mathrm{LOAD}}/p_{\mathrm{LOAD}}$ is high $\pm$ 46.5 %, highlighted with the superscript c, as the absolute error Δp_{LOAD} deriving from the efficiency mapping is high in contrast to p_{LOAD}. However, the relative error with low power has a minor impact on the full cycle

Table 2.9. Accuracy of p_{LOAD} when the starting point of modeling is mechanical power.

p_{mech} [kW]	p_{LOAD} [kW]	Δp_{LOAD} [W]	$\Delta p_{\mathrm{LOAD}}/p_{\mathrm{LOAD}}$ [%]
+ 1.0[a]	+ 5.0	± 93.1	± 1.86
− 1.0[a]	− 0.20	± 93.1	± 46.5[c]
+ 100[b]	+ 118	± 2190	± 1.86[d]
− 100[b]	− 85.0	± 2190	± 2.58[d]

[a] At 30 rpm, [b] at 3000 rpm.

cumulative error in which error values close to the nominal power are dominant, cf. superscripts d.

Some deductions are needed, in order to extend the analysis further from Δp_{LOAD}. In the assessed powertrain case, the intermediate circuit voltage is controlled with the PI-regulator, thus the actual value of u_{DC} is a constant. Therefore, the static error of $\Delta i_{\mathrm{LOAD}}/i_{\mathrm{LOAD}}$ equals to $\Delta p_{\mathrm{LOAD}}/p_{\mathrm{LOAD}}$. Furthermore, the PI-regulator ensures that,

$$i_{\mathrm{LOAD}} = i_{\mathrm{ES}} + i_{\mathrm{AFE}}, \tag{2.60}$$

in the static-state.

Due to EMS, the current of ESS i_{ES} can be solved. Fig. 2.23 illustrates error paths that exist in the system under assessments. The primary sources of error in simulations are efficiency mappings η_{ED} and $\eta_{\mathrm{DC/DC}}$, as well as measurements i_{es}, u_{uc}, and u_{DC}.

According to Eq. 2.53, the accuracy of the ESS current is dependent on i_{es}, u_{es}, u_{DC}, and $\eta_{\mathrm{DC/DC}}$, as

$$\Delta i_{\mathrm{ES}} = \left|\frac{\delta i_{\mathrm{ES}}}{\delta i_{\mathrm{es}}}\right|\Delta i_{\mathrm{es}} + \left|\frac{\delta i_{\mathrm{ES}}}{\delta u_{\mathrm{es}}}\right|\Delta u_{\mathrm{es}} + \left|\frac{\delta i_{\mathrm{ES}}}{\delta u_{\mathrm{DC}}}\right|\Delta u_{\mathrm{DC}} + \left|\frac{\delta i_{\mathrm{ES}}}{\delta \eta_{\mathrm{DC/DC}}}\right|\Delta \eta_{\mathrm{DC/DC}}. \tag{2.61}$$

This can be written, while discharging, as

$$\frac{u_{\mathrm{es}} \cdot \eta_{\mathrm{boost}}}{u_{\mathrm{DC}}}\Delta i_{\mathrm{es}} + \frac{i_{\mathrm{es}} \cdot \eta_{\mathrm{boost}}}{u_{\mathrm{DC}}}\Delta u_{\mathrm{es}} + \frac{u_{\mathrm{es}} \cdot i_{\mathrm{es}} \cdot \eta_{\mathrm{boost}}}{u_{\mathrm{DC}}^2}\Delta u_{\mathrm{DC}} + \frac{u_{\mathrm{es}} \cdot i_{\mathrm{es}}}{u_{\mathrm{DC}}}\Delta \eta_{\mathrm{boost}}, \tag{2.62}$$

and while charging, as

$$\frac{u_{\mathrm{es}}}{u_{\mathrm{DC}} \cdot \eta_{\mathrm{buck}}}\Delta i_{\mathrm{es}} + \frac{i_{\mathrm{es}}}{u_{\mathrm{DC}} \cdot \eta_{\mathrm{buck}}}\Delta u_{\mathrm{es}} + \frac{u_{\mathrm{es}} \cdot i_{\mathrm{es}}}{u_{\mathrm{DC}}^2 \cdot \eta_{\mathrm{buck}}}\Delta u_{\mathrm{DC}} + \frac{u_{\mathrm{es}} \cdot i_{\mathrm{es}}}{u_{\mathrm{DC}} \cdot \eta_{\mathrm{buck}}^2}\Delta \eta_{\mathrm{buck}}.$$

In Eqs. 2.62, known error values are Δu_{es}, Δu_{DC}, $\Delta \eta_{\mathrm{boost}}$, and $\Delta \eta_{\mathrm{buck}}$. Accuracies of Δu_{es} and Δu_{DC} are chosen to equal the overall accuracy of the voltage transducer Δu_{meas} *AV100-750* (LEM), which changes from ± 0.7 %

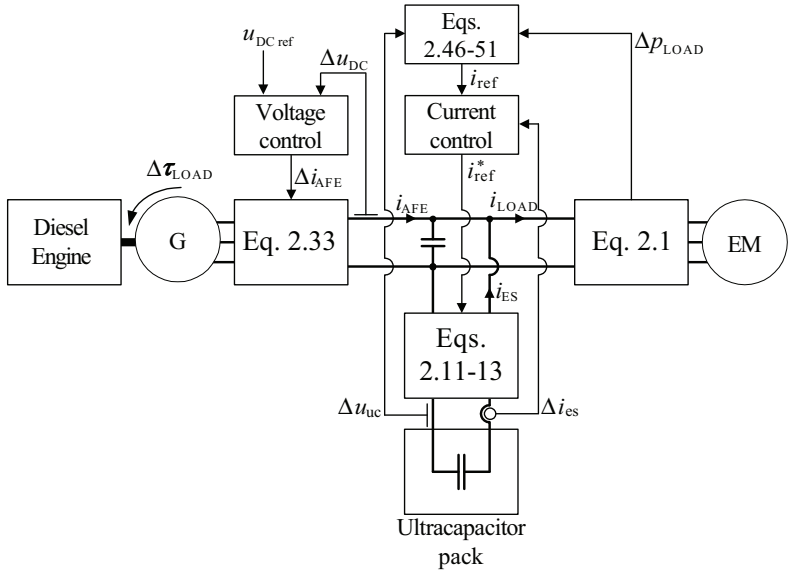

Figure 2.23. Error paths of the model-based design for the diesel-electric powertrain with an active UC buffering.

to $\pm$ 1.7 % at nominal voltage of 750 V depending on the considered temperature range, either constant +25 °C, or $-40 \ldots +85$ °C. The accuracies of efficiency mappings, i.e. η_{boost} and η_{buck}, were derived to $\pm$ 0.5 % with look-up table data, and to $\pm$ 0.9 % based on a polynomial function. The accuracies of efficiency mappings do not consider temperature dependencies in any means. The unknown Δi_{es} is dependent on control algorithms, as described in Section 2.1.11. Furthermore, the Δu_{es} is a function of i_{es}, and thus errors have a cross coupling. Therefore, Δu_{es} is simplified to the neighborhood of u_{es} together with the overall measurement accuracy Δu_{meas}, as

$$\Delta u_{\mathrm{es}} = \Delta u_{\mathrm{uc}} = \Delta u_{\mathrm{uc1}} + \Delta u_{\mathrm{uc2}} = R_{\mathrm{uc}} \cdot \Delta i_{\mathrm{es}} + \Delta u_{\mathrm{meas}}, \tag{2.63}$$

and the integral part of Eq. 2.18 determines the charge-discharge frequency error, as

$$\Delta d = \frac{(1/C_{\mathrm{uc}}) \cdot \int_0^t \Delta i_{\mathrm{es}} \mathrm{d}t}{2 \cdot (U_{\mathrm{max}} - U_{\mathrm{min}})}. \tag{2.64}$$

Thus, the error value Δi_{es} determines errors in both energy storage voltage and charge-discharge frequency.

Moreover, energy storage voltage affects to Δi_{es} due to feedback in control algorithms. However, the effect of Δu_{uc1} on Δi_{es}, cannot be taken into consideration, because of an existing algebraic loop. Thus, error Δi_{es} is considered to accumulate measurement accuracies of variables u_{es}, p_{LOAD}, and error Δi_{meas} as the offset in the PI-control of the converter current.

The error in u_{DC} is neglected. The error analysis considers the accuracy of the current measurement Δi_{meas} to equal with the overall accuracy of the current transducer *CT 50-T* (LEM), which is $\pm$ 0.1 % at the nominal current of 50 A within the $-25\ldots+70$ °C temperature range. Therefore, Δi_{es} is determined, as

$$\Delta i_{\mathrm{es}} = \left|\frac{\delta i_{\mathrm{es}}}{\delta u_{\mathrm{uc}}}\right| \Delta u_{\mathrm{uc}} + \left|\frac{\delta i_{\mathrm{es}}}{\delta p_{\mathrm{LOAD}}}\right| \Delta p_{\mathrm{LOAD}} + \Delta i_{\mathrm{meas}}. \tag{2.65}$$

In Eq. 2.65, the first partial derivative in respect of u_{uc} can be derived, as

$$\left|\frac{\delta i_{\mathrm{es}}}{\delta u_{\mathrm{uc}}}\right| \Delta u_{\mathrm{uc}} = \left|\frac{\delta[P \cdot (u_{\mathrm{DC\_ref}} - u_{\mathrm{DC}}) \cdot u_{\mathrm{DC}}/u_{\mathrm{uc}} + (p_{\mathrm{LOAD}} - p_{\mathrm{filter}})/u_{\mathrm{uc}}]}{\delta u_{\mathrm{uc}}}\right| \Delta u_{\mathrm{uc}},$$

in which the difference of $u_{\mathrm{DC\_ref}}$ and u_{DC} becomes zero, and the parallel controller, as

$$\left|\frac{p_{\mathrm{LOAD}}}{u_{\mathrm{uc}}^2} - \left(2 \cdot P_{\mathrm{MAX}} - \sum_{t_{\mathrm{i}}=t_{\mathrm{k-n}}}^{t_{\mathrm{k}}} [p_{\mathrm{LOAD}}(t_{\mathrm{i}})/(n+1)]\right) \Big/ u_{\mathrm{uc}}^2\right| \Delta u_{\mathrm{uc}}.$$

Then, the partial derivative in respect of load power gives,

$$\left|\frac{\left[p_{\mathrm{LOAD}}(t_{\mathrm{k}}) + \sum_{t_{\mathrm{i}}=t_{\mathrm{k-n}}}^{t_{\mathrm{k}}} [p_{\mathrm{LOAD}}(t_{\mathrm{i}})/(n+1)] \cdot (1 - u_{\mathrm{uc}}/U_{\mathrm{max}})\right] \Big/ u_{\mathrm{uc}}}{\delta p_{\mathrm{LOAD}}}\right| \Delta p_{\mathrm{LOAD}},$$

$$= \frac{\Delta p_{\mathrm{LOAD}}(t_{\mathrm{k}}) + \sum_{t_{\mathrm{i}}=t_{\mathrm{k-n}}}^{t_{\mathrm{k}}} [\Delta p_{\mathrm{LOAD}}(t_{\mathrm{i}})/(n+1)] \cdot (1 - u_{\mathrm{uc}}/U_{\mathrm{max}})}{u_{\mathrm{uc}}}.$$

Table 2.10 illustrates energy storage current error values depending on considered error sources. Eight different operation points with variance in p_{LOAD} value, power direction, and energy storage voltage are used to give an overview of variance in error values. Five different error values for each of the operation points are presented, which refer to different error sources as: $\Delta i_{\mathrm{es1}}/i_{\mathrm{es}}$ considers $\Delta u_{\mathrm{uc}} = 0.7$ % and $\Delta p_{\mathrm{LOAD}} = 0.0$ %, $\Delta i_{\mathrm{es2}}/i_{\mathrm{es}}$ considers $\Delta u_{\mathrm{uc}} = 1.7$ % and $\Delta p_{\mathrm{LOAD}} = 0.0$ %, $\Delta i_{\mathrm{es3}}/i_{\mathrm{es}}$ considers $\Delta u_{\mathrm{uc}} = 0.0$ % and $\Delta p_{\mathrm{LOAD}} =$ Table 2.9, $\Delta i_{\mathrm{es4}}/i_{\mathrm{es}}$ considers $\Delta u_{\mathrm{uc}} = 0.7$ % and $\Delta p_{\mathrm{LOAD}} =$ Table 2.9, and $\Delta i_{\mathrm{es5}}/i_{\mathrm{es}}$ considers $\Delta u_{\mathrm{uc}} = 1.7$ % and $\Delta p_{\mathrm{LOAD}} =$ Table 2.9. In all cases, Δi_{meas} is considered to be 0.1 %.

The results of Table 2.10 show that an error may be significant at low loads, but decreases remarkably, when high loads are transferred. In the worst error cases, highlighted with superscripts a, the regenerative power magnitude is negligible, i.e. $-$ 0.2 kW, which is not possibly transferred to the ES system at all. Therefore, a realistic i_{es} maximum error with low loads is in the range of $\pm$ 53... 134 %, cf. superscripts b, and with high

loads in the range of $\pm$ 0.35... 5.8 %, cf. superscripts c. Furthermore, as stated before, high error values with low loads have a small impact on the full cycle cumulative error value in which error values close to the nominal power are dominant.

Five different cases of ES current errors with different assumptions of the present situation are explained in next paragraphs.

Case 1 refers to either the system modeling beginning from the intermediate circuit load p_{LOAD}, or control error in the real system in which p_{LOAD} is measured accurately. The temperature is assumed to be +25 °C. In such a case, i_{es} error at a high load is in the range of $\pm$ 0.52 %, and with a low load at $\pm$ 53 %.

Case 2 is equal to Case 1 except that an assumption of temperature is changed to -40...+85 °C. In Case 2, comparable error values are $\pm$ 1.1 % with high, and $\pm$ 130 % with low-loads, respectively.

Case 3 assumes errors of p_{LOAD} will be realized due to inaccuracies in the efficiency mapping of an electric drive. However, the energy-storage voltage measurement is considered ideal. In the third case, i_{es} error values vary within $\pm$ 4.7 % with high and low-loads, respectively.

The fourth case assumes all measurement errors to realize in +25 °C ambient temperature, and thus, error values at a high load is in the range of $\pm$ 5.2 % and with a low load at $\pm$ 58 %.

The fifth case is similar to Case 4 with a difference in the ambient temperature range which is -40...+85 °C. Then, error values were within $\pm$ 5.8 %, and $\pm$ 134 %, respectively.

The moving average in Eq. 2.65, approximately halves ramp-up p_{LOAD} signals, and passes long-time constant p_{LOAD} signals by multiplying those with a coefficient of one. The assumption of the ramp-up p_{LOAD} refers to acceleration of a vehicle from zero speed, and the period of constant power refers to acceleration or deceleration of a vehicle with some initial speed. Table 2.10 presents error values referring to the long-time constant p_{LOAD} case. Furthermore, it is assumed that half of the positive load power is taken from the ES system and half from the primary source. On the contrary, all the regenerative power is charged to the ES system. An effect of this assumption can be seen in the differences between motoring and regenerating i_{es} accuracies with high loads as, e.g., regenerative error values are smaller. In addition, this evaluation assumes U_{max} to be 390 V, and U_{min} to 200 V, respectively.

The maximum error of the energy storage voltage based on Eq. 2.63 and

Table 2.10. Accuracies of the energy storage current.

p_{LOAD} [kW]	u_{uc} [V]	i_{es} [A]	$\Delta i_{\mathrm{es1}}/i_{\mathrm{es}}$ [%]	$\Delta i_{\mathrm{es2}}/i_{\mathrm{es}}$ [%]	$\Delta i_{\mathrm{es3}}/i_{\mathrm{es}}$ [%]	$\Delta i_{\mathrm{es4}}/i_{\mathrm{es}}$ [%]	$\Delta i_{\mathrm{es5}}/i_{\mathrm{es}}$ [%]
+ 5.0	390	+ 6.4	$\pm$ 53[b]	$\pm$ 130	$\pm$ 3.8	$\pm$ 57	$\pm$ 133
+ 5.0	295	+ 8.5	$\pm$ 53[b]	$\pm$ 130	$\pm$ 4.7	$\pm$ 58	$\pm$ 134[b]
− 0.2	200	− 1.0	$\pm$ 700[a]	$\pm$ 1700[a]	$\pm$ 70[a]	$\pm$ 770[a]	$\pm$ 1770[a]
− 0.2	295	− 0.70	$\pm$ 700[a]	$\pm$ 1700[a]	$\pm$ 60[a]	$\pm$ 760[a]	$\pm$ 1750[a]
+ 118	390	+ 150	$\pm$ 0.52	$\pm$ 1.1	$\pm$ 3.8	$\pm$ 4.2	$\pm$ 4.8
+ 118	295	+ 200	$\pm$ 0.52	$\pm$ 1.1	$\pm$ 4.7	$\pm$ 5.2	$\pm$ 5.8[c]
− 85	200	− 430	$\pm$ 0.35[c]	$\pm$ 0.7	$\pm$ 3.9	$\pm$ 4.2	$\pm$ 4.5
− 85	295	− 290	$\pm$ 0.35[c]	$\pm$ 0.7	$\pm$ 3.3	$\pm$ 3.6	$\pm$ 3.9

Table 2.10 becomes $\pm$ 1.4... 3.3 V, for an UC module with capacitance of 17.8 F, R_{uc} of 65 mΩ, and $U_{\max}$ of 390 V. The corresponding Hardware-in-the-Loop experiments resulted to $\pm$ 1.0 V... 3.0 V accuracy in mean values. The lower voltage error value refers to modeling with a variable capacitance, and the higher error to constant capacitance, respectively. It can be noticed that experimented mean error values are within the theoretically calculated maximum error value of the ES voltage.

Then, the error of the ES system current on the intermediate circuit as functions of Δi_{es}, Δu_{es}, Δu_{DC}, and $\Delta \eta_{\mathrm{DC/DC}}$, described in Eq. 2.62, can be calculated. Furthermore, the error of the AFE converter current is the sum of the load current and ES system current errors. The results are presented in Table 2.11 with two different cases, when Δi_{es} uses the values of Cases 1 and 4 from Table 2.10, u_{DC} is 650 V with accuracy of Δu_{meas}, and $\Delta \eta_{\mathrm{DC/DC}}$ is $\pm$ 0.5 %.

Table 2.11. Energy storage system current Δi_{ES} and AFE converter current Δi_{AFE} accuracies on the intermediate circuit.

u_{uc} [V]	i_{es} [A]	$\eta_{\mathrm{DC/DC}}$ [%]	$\Delta i_{\mathrm{es}}/i_{\mathrm{es}}$ [%]	$\Delta i_{\mathrm{ES}}/i_{\mathrm{ES}}$ [%]	$\Delta i_{\mathrm{AFE}}/i_{\mathrm{AFE}}$ [%]
390	+ 6.4	95.6	$\pm$ 53... 57	$\pm$ 55... 59	$\pm$ 57... 61
295	+ 8.5	94.3	$\pm$ 53... 58	$\pm$ 55... 60	$\pm$ 57... 62
200	− 1.0	93.3	$\pm$ 699... 768[a]	$\pm$ 701... 770[a]	$\pm$ 750... 820[a]
295	− 0.70	94.3	$\pm$ 699... 757[a]	$\pm$ 701... 759[a]	$\pm$ 750... 810[a]
390	+ 150	97.5	$\pm$ 0.52... 4.2	$\pm$ 2.4... 6.3	$\pm$ 4.3... 8.1
295	+ 200	96.9	$\pm$ 0.52... 5.2	$\pm$ 2.5... 7.3	$\pm$ 4.3... 9.2
200	− 430	95.8	$\pm$ 0.35... 4.2	$\pm$ 2.3... 6.7	$\pm$ 4.9... 9.3
295	− 290	97.0	$\pm$ 0.35... 3.6	$\pm$ 2.3... 5.7	$\pm$ 4.9... 8.3

Note: variation in $\Delta i_{\mathrm{es}}/i_{\mathrm{es}}$, $\Delta i_{\mathrm{ES}}/i_{\mathrm{ES}}$, and $\Delta i_{\mathrm{AFE}}/i_{\mathrm{AFE}}$ refers to the cases 1 and 4 in accuracies of the energy storage current i_{es}.

Maximum error values in Table 2.11 refer to cases in which all partial

errors are realized with their maximum values in the same direction. The minimum values refer to cases where the system loading were considered electrical, and the maximum values refer to mechanical starting points of the modeling, respectively. Ambient temperature have been assumed to +25 °C. Considered error sources are efficiency mapping of an electric drive, ES current and voltage measurement errors for control of the ES system. In addition, this assessment included the DC-DC converter plant-model realization inaccuracies consisting of maximum errors in ES current and voltage, DC-link voltage, and efficiency mapping of the DC-DC converter. Resulted values are pessimistic, and for more descriptive error values, the sensitivity analysis should be used.

Furthermore, the highest error values in Tables 2.10 and 2.11, highlighted with superscripts a, can be neglected, because such small powers are most likely not delivered through an ES system. In practice, auxiliary loads in the intermediate circuit are higher than those regenerative powers in question, and thus in those cases, power control would not necessarily react at all.

The error in charge-discharge frequency bases on Eq. 2.64 which can be further derived to

$$\frac{\Delta d}{d} = \int_0^t \frac{\Delta i_{\mathrm{es}}}{i_{\mathrm{es}}} \mathrm{d}t. \tag{2.66}$$

Thus, the maximum error of d for low power operation is within $\pm$ 53. . . 58 %, and for high power operation within $\pm$ 0.35. . . 5.2 %, based on i_{es} values in Table 2.11.

Finally, load torque of an engine $\boldsymbol{\tau}_{\mathrm{load}}$ can be solved, which is based on the AFE-converter current i_{AFE} and efficiency mapping of an electric drive η_{ED}. An error in generator speed is considered zero due to the speed PI-controller for an engine. Load torque can be derived, as

$$\Delta\boldsymbol{\tau}_{\mathrm{load}} = \left|\frac{\delta\boldsymbol{\tau}_{\mathrm{load}}}{\delta i_{\mathrm{AFE}}}\right| \Delta i_{\mathrm{AFE}} + \left|\frac{\delta\boldsymbol{\tau}_{\mathrm{load}}}{\delta \eta_{\mathrm{ED}}}\right| \Delta\eta_{\mathrm{ED}}, \tag{2.67}$$

thus

$$\Delta\boldsymbol{\tau}_{\mathrm{load}} = \frac{u_{\mathrm{DC}}}{\eta_{\mathrm{ED}} \cdot \omega_{\mathrm{G}}} \Delta i_{\mathrm{AFE}} + \frac{u_{\mathrm{DC}} \cdot i_{\mathrm{AFE}}}{\eta_{\mathrm{ED}}^2 \cdot \omega_{\mathrm{G}}} \Delta\eta_{\mathrm{ED}}, \text{ when } i_{\mathrm{AFE}} > 0,$$

and

$$\Delta\boldsymbol{\tau}_{\mathrm{load}} = \frac{u_{\mathrm{DC}} \cdot \eta_{\mathrm{ED}}}{\omega_{\mathrm{G}}} \Delta i_{\mathrm{AFE}} + \frac{u_{\mathrm{DC}} \cdot i_{\mathrm{AFE}}}{\omega_{\mathrm{G}}} \Delta\eta_{\mathrm{ED}}, \text{ when } i_{\mathrm{AFE}} < 0.$$

The AFE-converter-generator combination efficiency mapping accuracies are based on sensor accuracies in Table 2.7, and derived for two different

Table 2.12. Efficiency mapping accuracies of the generator electric drive in considered operations points.

u_{DC} [V]	i_{AFE} [A]	ω_{EM} [rad/s]	$\boldsymbol{\tau}_{\mathrm{EM}}$ [Nm]	$\Delta\eta_{\mathrm{ED}}$ [%]
+ 650	+ 3.85	+ 314.1	+ 16.0	$\pm$ 63.4
+ 650	+ 90.5	+ 314.1	+ 220	$\pm$ 3.01

motoring operation points based on Eq. 2.57. Results are presented in Table 2.12.

Then, Eq. 2.67 with the positive i_{AFE} results to relative errors of $\pm$ **180 . . . 190** % for low loads, and to $\pm$ **7.9 . . . 13** % for high loads, respectively. Finally, relative errors of fuel consumption are available, if

$$\frac{\Delta\dot{m}}{\dot{m}} \approx \frac{\Delta\boldsymbol{\tau}_{\mathrm{load}}}{\boldsymbol{\tau}_{\mathrm{load}}}, \tag{2.68}$$

is assumed. Smaller error values correspond to cases with electrical load as the starting point, and maximum values refer to the mechanical starting point, respectively. The values assume ambient temperature to be in the range of +25 °C. Considered error sources are efficiency mappings of all power electronics devices and electric machines, current and voltage measurement errors for control of the system, and inaccuracies in realization of the DC-DC converter plant model. After all, presented accuracies still neglect the fuel consumption mapping accuracy of an engine, due to lack of completed measurements. Inclusion of errors due to an engine model to this analysis is a convenient direction for the research.

Although, the relative error values for variables become high due to a cumulation of errors. It should be remarked that error values represent the maximum errors in which all errors are realized in the same direction, and thus, are the worst-case values. More representative error values could be attained with sensitivity analysis that is the direction where the error analysis is proceeding on next section.

Proposed sub-system models were in the beginning targeted to mean values with the 20-Hz bandwidth. Highlighted experiments and simulations in Fig. 2.6 show that low-frequency operation behavior can be predicted with proposed models. Furthermore, the error analysis gives the theoretical maximum error value for the predicted fuel consumption in static states, which could be complemented by the error analysis of transient states. The presented maximum error values in fuel consumption are high due to a cumulation of errors in different sub-systems. Maximum

error values can be decreased by use of several measurement rounds e.g. in efficiency mappings.

The target of the proposed models was to predict system behavior in the 20-Hz bandwidth, which has been proven to some extent. Thus, proposed models enable design of EMSs only within this bandwidth; and faster behaviors, i.e. small-signal behaviors, are most likely not predicted with appropriate accuracy. Furthermore, the proposed modeling approach may not be used as the precision tool for fuel consumption predictions, as noticed in the error analysis, although correctly directed results may be achieved. Thus, the proposed simulation models are proper for the design of different energy management hierarchies by the Model- and Hardware-in-the-Loop principles, and e.g., for comparison studies between powertrain topologies.

The analysis of maximum errors of the proposed simulation method illustrates that small individual error values cumulate to a high total maximum error value in fuel consumption of the studied system. Thus, based on this type of an analysis, it is unclear what would be a sufficient accuracy of a sub-system model. For instance, an increase in an error of the DC-DC converter efficiency mapping from $\pm$ 0.5 % to $\pm$ 0.9 % has a greater influence on fuel consumption error than on interface variables of the converter. Therefore, other methods for error analyses are needed, as the Monte Carlo method that has traditionally been used for analysis and design of complex systems. Systematic use of the Monte Carlo method in the error analysis leads to knowledge of required accuracies in sub-system models and to knowledge of achievable accuracies in full-system models.

The error analysis based on the partial differentiation is laborious, as can be noticed from this section. On the other hand, such maximum error analysis increases insight of the errors in the system, and thus becomes valuable to fulfill.

2.3.2 Monte Carlo Method

The Monte Carlo method is a numerical method of solving mathematical problems by means of random sampling [Sobol, 1975].

The birth of the Monte Carlo method is regarded to the paper of Metropolis and Ulam [1949] [Sobol, 1975], although some claim the concept of Monte Carlo to exist already in the times of the Old Testament [Dimov and McKee, 2007]. The reinvention seems natural, since this method could not be used on any significant scale before the advent of electronic

computers [Sobol, 1975].

The Monte Carlo algorithms are currently widely used for such problems that the deterministic algorithms break down. These problems are, e.g., high-dimensional integration, integral and integro-differential equations of high dimensions, boundary-value problems for differential equations in domains with complicated boundaries, simulation of turbulent flows, studying chaotic structures, etc. [Dimov and McKee, 2007].

There are two main directions in the development and study of Monte Carlo algorithms. The first of these is *Monte Carlo simulation* and the second is *Monte Carlo numerical* algorithms. In the first case, the algorithms just follow the corresponding physical, chemical or biological processes under consideration. In such simulations, the Monte Carlo method is used as a tool for choosing one of many different possible outcomes of a particular process. Thus, the Monte Carlo simulation could be considered as a method for solving probabilistic problems using some kind of simulations of random variables, as in Sobol [1975, pp. 44-46]. In the second case, it is used for solving deterministic problems by modeling random variables. In this case, the main idea is to construct an artificial random process that equals to the mathematical expectations of the actual process. [Dimov and McKee, 2007]

In next sections, the Monte Carlo simulation, Sobol [1975, pp. 44-46], is used to assess the robustness of the energy management scheme, as well as relevancies of electrical quantity measures and plant parameter errors.

2.3.3 Monte Carlo Simulation

The first step in conducting a Monte Carlo simulation experiment, according to Mooney [1997], is to define those parameters that are deterministic and those that are stochastic. Changes of variables should be based on substantive theories, although practical and experimental design considerations can be taken into account.

In the following experiment of a sensitivity analysis, substantive theories of variable changes are explained in Section 2.1, deterministic parameters are given in Table 2.13, and stochastic parameters are introduced in the following.

A stochastic variation is applied to some of electrical quantity measures and plant parameters: the load power measurement accuracy η_{ED1}, the offset in the current control accuracy i_{uc}, the UC voltage measurement

for the energy management u_{uc}, the DC-link voltage measurement for the energy management u_{DC}, the efficiency mapping accuracy of the converter plant model $\eta_{\mathrm{DC/DC}}$, and the efficiency mapping accuracy of the AFE-generator plant model η_{ED2}. These measures and parameters are chosen due to interest of their effect on the energy management and to modeled variables. The number of varied parameters needs to be limited in order to avoid exhaustive amount of Monte Carlo simulations for the determination of sensitivity indices

These stochastic parameters are varied with randomly changing coupling coefficients. A random coupling coefficient has a unity average and is uniformly distributed within maximum error limits, as already suggested by Metropolis and Ulam [1949]. These maximum error limits are: ± 2.6 % for η_{ED1}, ± 0.1 % for i_{uc}, ± 1.7 % for u_{uc}, ± 1.7 % for u_{DC}, ± 0.9 % for $\eta_{\mathrm{DC/DC}}$, and ± 3.0 % for η_{ED2}. These error limits base on values presented in Section 2.3.1. The uniform distribution of stochastic parameters introduces higher deviation than the normal deviation based on the three-sigma rule [Sobol, 1975, p. 46]. The uniform distribution is used since there was no knowledge available how these parameters vary within the maximum error limits.

The conclusions of the error analysis are interpreted from mean values of standard deviations. The standard deviation, when applied to the same instantaneous moments of various simulation rounds, is defined as

$$\sigma(t) = \left(\frac{1}{n-1} \sum_{i=1}^{n} (y_i(t) - \bar{y}(t))^2 \right)^{\frac{1}{2}}, \tag{2.69}$$

where n is the number of simulation rounds, y_i refers to the modeled variable of the i^{th} simulation round, and $\bar{y}$ to the mean of that variable of all samples, i.e.

$$\bar{y}(t) = \frac{\sum_{i=1}^{n} y_i(t)}{n}. \tag{2.70}$$

The mean of the standard deviation is calculated, as

$$\bar{\sigma} = \frac{\sum_{t=t_1}^{t_k} \sigma(t)}{k}, \tag{2.71}$$

where k is the amount of time indices.

The random parameter set θ refers to any of the stochastic parameters η_{ED1}, i_{uc}, u_{uc}, etc. The deterministic variable set is described with X, which has a relation f to the random variable set, as

$$Y = f[X_1(\theta), \ldots, X_M(\theta)]. \tag{2.72}$$

Y becomes variable due to the stochastic θ. In this context Y refers to the assessed variables in Tables 2.14...2.16, i.e. p_{LOAD}, p_{uc}, p_{VSDG}, etc. In the situation when all stochastic parameters are varied, the mean of the standard deviation is denoted with $\bar{\sigma}[Y(\theta)]$.

The standard deviation shows how much variation exists in contrast to the mean of the variable. Fig. 2.24 illustrates cumulative probabilities within bands of the standard deviation. The band from the mean μ to σ contains 34.1 % of a population, the band $\sigma \ldots 2\sigma$ contains 13.6 %, etc.

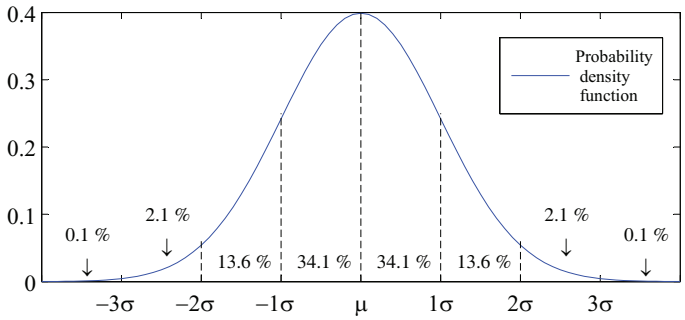

Figure 2.24. Normal distribution where each band has width of the standard deviation. The midpoint of the x-axis is on the mean of a variable.

The sensitivity indices are calculated from the mean standard deviations of each- and all-stochastic parameters. The mean standard deviation due to variation of one stochastic parameter is described by $f(X_M(\theta))$. Therefore, the mean of the sensitivity index for one stochastic parameter and multiple deterministic parameters can be described, e.g., by

$$\bar{S} = \left(\frac{\bar{\sigma}[f(X_1, X_2 \ldots, X_M(\theta), X_{M+1}, \ldots)]}{\bar{\sigma}[Y(\theta)]} \right)^2 . \tag{2.73}$$

The subscripts of $\bar{S}$ refers to the variable that is varied, such as $\bar{S}_{\eta_{\mathrm{ED1}}}$, $\bar{S}_{i_{\mathrm{uc}}}$, etc. This notation is used while presenting results in Section 2.3.5.

2.3.4 Global Sensitivity Indices

According to Sobol [2001], global sensitivity indices for rather complex mathematical models can be efficiently computed by Monte Carlo (or quasi-Monte Carlo) methods. These indices, described in Section 2.3.3, are used for estimating the influence of individual variables or groups of variables on the model output. Furthermore, according to Dimov and Georgieva [2010], these indices show which of the input variables has to be known more accurately to reduce the output variance. This section introduces interpretation of results based on these sensitivity indices.

According to Sobol [2001], three types of problems can be studied with the aid of global sensitivity indices. These are: ranking of variables in $f(X_1, \ldots, X_M)$, fixing of unessential variables in $f(X_1, \ldots, X_M)$, and deleting of high order members based on the variable ranking. The simplest approach to rank variables is by the first order indices $S_1, \ldots, S_M$. However, the ranking based on the first order indices becomes inaccurate if the sum of $S_1 + \ldots + S_M$ is much less than one. In such case, the higher order indices have to be taken in the evaluation.

Generally, relevancy of a parameter can be categorized based on total sensitivity indices which are sums of the first and higher order interactions of a parameter to an output function, i.e., a higher total sensitivity index value means a higher importance of a parameter [Sobol, 2001; Dimov and Georgieva, 2010].

In the interpretation of the results the most informative sensitivity indices are the extreme values, such a way that the zero value means that a variable does not depend on this parameter, and the one value means that a variable depends on this parameter only. There also exists other classification criteria, in which parameter is considered, e.g., as very important if $S_M > 0.8$, important if $0.8 > S_M > 0.5$, unimportant if $0.5 > S_M > 0.3$, and irrelevant if $0.3 > S_M$ [Sobol, 2001; Dimov and Georgieva, 2010]. This, however, seems to give one-sided conclusions due to dominance of single stochastic parameter in the results. Therefore, the following analysis categorizes parameter influences as major when $S_M \geq 0.76$, significant when $0.23 \geq S_M \geq 0.13$, minor when $0.038 \geq S_M \geq 0.0026$, and negligible when $0.0011 \geq S_M$.

In our sensitivity analysis, the first order interactions explain almost all variations in the assessed variables, and thus parameter importance can be concluded with the small risk of an error.

2.3.5 Results of Sensitivity Analysis

The evaluated powertrain topology case and energy managements are the same as described in Section 2.1.11, and used for the error analysis in Section 2.3.1. The deterministic parameters are given in Table 2.13, and the results in Tables 2.14. . . 2.16 as well as illustrated in Figs. 2.25. . . 2.27 with subsequent explanations.

Table 2.13 presents parameters that enable reproduction of a similar work.

The results, in Tables 2.14. . . 2.16, illustrate variations of power vari-

Table 2.13. Deterministic parameters for realization of the sensitivity analysis.

Parameters	Value	Unit
DC link		
Capacitance C_{DC}	20	mF
Resistance R_{DC}	0.2	mΩ
Initial voltage $U_{\mathrm{DC\_initial}}$	650	V
AFE-converter		
Control delay τ_{AFE}	3.0	ms
Integral coefficient K_{I}	0.2	
Proportional coefficient K_{P}	4	
DC/DC-converter		
Control delay $\tau_{\mathrm{DC/DC}}$	10.0	ms
Maximum current limit I_{max}	400	A
Minimum current limit I_{min}	0	A
Ultracapacitor		
Capacitance C_{uc}	31.5	F
Resistance R_{uc}	34.9	mΩ
Initial voltage $U_{\mathrm{uc\_initial}}$	490	V
Variable speed diesel generator-set		
Inertia of the shaft J_{tot}	1	$\mathrm{kg \cdot m^2}$
Speed controller K_{P}	0.5	
Speed reference change rate limiter	$\pm$ 50	rpm
Speed reference $n_{\mathrm{e\_idle}}$	1000 rpm @ 0…30 kW	
Speed reference $n_{\mathrm{e\_1}}$	1200 rpm @ 12…50 kW	
Speed reference $n_{\mathrm{e\_2}}$	1400 rpm @ 30…70 kW	
Speed reference $n_{\mathrm{e\_3}}$	1700 rpm @ 50…90 kW	
Energy Management		
Tuning parameter P_{MAX}	$1.5 \cdot 10^5$	W
P-controller for voltage P	2	
Maximum voltage of the UC pack $U_{\mathrm{uc}}^{\mathrm{max}}$	500	V
Limitation high voltage of the UC pack $U_{\mathrm{uc}}^{\mathrm{high}}$	490	V

ables: p_{LOAD}, p_{uc}, p_{VSDG}, p_{BRK}; current variables: i_{LOAD}, i_{ES}, i_{AFE}, i_{BRK}, i_{uc}; and miscellaneous variables: u_{DC}, τ_{load}, u_{uc}, n_{VSDG}, $\dot{m}_{\mathrm{VSDG}}$, during the ECE-15 based load cycle. Variations of output variables are caused by the stochastic parameters η_{ED1}, i_{uc}, u_{uc}, u_{DC}, $\eta_{\mathrm{DC/DC}}$, and η_{ED2}. These results are calculated with n simulation rounds, such that the mean standard deviation with all stochastic parameters has $n = 1000$, and calculation of the sensitivity indices have $n = 100$. These n values are small, because of a long computation time of one simulation, and they result to the total calculation time of approximately 7…70 hours with duo central processing

unit (CPU) at 2.0 GHz with 3.45 GB of random-access memory (RAM). Following paragraphs interpret results based on knowledge given in Section 2.3.4.

Table 2.14. Sensitivity analysis results for powers. Standard deviations and first order Sobol indices.

	p_{LOAD}	p_{uc}	p_{VSDG}	p_{BRK}
$\bar{\sigma}[Y(\theta)]$	0.55 kW	3.0 kW	2.8 kW	0.55 kW
$\bar{S}_{\eta_{\mathrm{ED1}}}$	9.4e−1[a]	1.8e−2[c]	2.0e−2[e]	2.6e−3
$\bar{S}_{i_{\mathrm{uc}}}$	7.9e−27[a]	1.8e−5	2.1e−5	1.3e−6
$\bar{S}_{u_{\mathrm{uc}}}$	7.9e−27[a]	2.0e−2[c]	2.2e−2[e]	5.9e−3
$\bar{S}_{u_{\mathrm{DC}}}$	8.0e−27[a]	9.3e−1[b]	8.5e−1[d]	1.0e+0[f]
$\bar{S}_{\eta_{\mathrm{DC/DC}}}$	8.0e−27[a]	1.1e−4	1.1e−3	3.8e−5
$\bar{S}_{\eta_{\mathrm{ED2}}}$	8.0e−27[a]	5.2e−10	2.7e−2[e]	2.5e−9
$\Sigma\bar{S}_{\theta}$	9.4e−1	9.7e−1	9.3e−1	1.0e+0[f]

Table 2.14 indicates that p_{LOAD} depends only on the accuracy of η_{ED1}, i.e. the load power measurement accuracy, cf. indices with superscripts a. The major influence on p_{uc} is with u_{DC}, cf. b, minor influences are with η_{ED1} and u_{uc}, cf. c, and other influences are negligible. Similarly, the major impact to p_{VSDG} is with u_{DC}, cf. d, minor influences are with η_{ED1}, u_{uc}, and η_{ED2}, cf. e, and other error factors are negligible. p_{BRK} depends only on u_{DC}, cf. f.

Table 2.15. Sensitivity analysis results for currents. Standard deviations and first order Sobol indices.

	i_{LOAD}	i_{ES}	i_{AFE}	i_{BRK}	i_{uc}
$\bar{\sigma}[Y(\theta)]$	0.24 A	4.7 A	4.0 A	0.78 A	7.3 A
$\bar{S}_{\eta_{\mathrm{ED1}}}$	1.8e−2[b]	1.8e−2[b]	2.1e−2[b]	2.6e−3[b]	2.0e−2[b]
$\bar{S}_{i_{\mathrm{uc}}}$	1.5e−5	1.8e−5	2.3e−5	1.3e−6	1.9e−5
$\bar{S}_{u_{\mathrm{uc}}}$	1.5e−2[b]	2.0e−2[b]	2.3e−2[b]	5.9e−3[b]	7.9e−3[b]
$\bar{S}_{u_{\mathrm{DC}}}$	9.1e−1[a]	9.3e−1[a]	9.1e−1[a]	1.0e+0[a]	9.6e−1[a]
$\bar{S}_{\eta_{\mathrm{DC/DC}}}$	4.2e−4	8.9e−4	1.1e−3	3.8e−5	9.4e−5
$\bar{S}_{\eta_{\mathrm{ED2}}}$	1.1e−9	5.4e−10	3.4e−10	2.5e−9	4.3e−10
$\Sigma\bar{S}_{\theta}$	9.5e−1	9.6e−1	9.6e−1	1.0e+0	9.9e−1

Table 2.15 shows that although the load power depends only on the accuracy of η_{ED1}, still i_{LOAD} is mostly affected by u_{DC}, and has also minor

impacts from η_{ED1} and u_{uc}. Generally, the DC-link voltage has a major influence on each of Table 2.15 currents, cf. indices with superscripts a. Minor impacts to these currents are with η_{ED1} and u_{uc}, cf. b. Altering of parameters i_{uc}, $\eta_{\mathrm{DC/DC}}$, and η_{ED2} have negligible importance.

Table 2.16. Sensitivity analysis results for miscellaneous variables. Standard deviations and first order Sobol indices.

	u_{DC}	τ_{load}	u_{uc}	n_{VSDG}	$\dot{m}_{\mathrm{VSDG}}$
$\bar{\sigma}[Y(\theta)]$	2.4 V	23 Nm	9.4 V	51 rpm	0.53 kg/h
$\bar{S}_{\eta_{\mathrm{ED1}}}$	6.6e−3	4.9e−2[c]	3.1e−3	1.3e−1[h]	3.1e−2[j]
$\bar{S}_{i_{\mathrm{uc}}}$	5.0e−6	2.1e−5	1.2e−6	1.7e−6	2.0e−5
$\bar{S}_{u_{\mathrm{uc}}}$	6.7e−3	6.5e−2[c]	2.1e−1[e]	2.3e−1[h]	3.8e−2[j]
$\bar{S}_{u_{\mathrm{DC}}}$	9.8e−1[a]	8.6e−1[b]	7.6e−1[d]	9.2e−1[g]	8.7e−1[i]
$\bar{S}_{\eta_{\mathrm{DC/DC}}}$	2.0e−4	9.0e−4	2.7e−6	1.5e−4	1.1e−3
$\bar{S}_{\eta_{\mathrm{ED2}}}$	1.1e−9	2.8e−2[c]	7.4e−11	2.5e−4	2.4e−2[j]
$\Sigma\bar{S}_{\theta}$	9.9e−1	1.0e+0	9.8e−1	1.3e+0[f]	9.6e−1

Table 2.16 suggests that the variance in the DC-link voltage is mainly caused by the voltage regulator measurement of the same voltage, i.e. the measurement of u_{DC}, cf. index with the superscript a. The load torque variation of an engine is also mainly caused by variation on u_{DC}, cf. b, although η_{ED1}, u_{uc}, and η_{ED2} have their minor impacts on this variable, cf. c. The ultracapacitor voltage is affected mostly by the measurement of u_{DC}, cf. d, and also with a significant effect by the measurement of u_{uc}, cf. e. The speed of VSDG becomes problematic due to an over one sum of the sensitivity indices, cf. f. Reasons for this are a relatively low amount of simulation rounds, i.e. 100, and the rule-based speed control with different speed modes, as described in Eq. 2.52 and seen in Fig. 2.27, which is not a smooth function and thus introduces higher uncertainty to the time when a threshold of the speed-state change is passed. In any case, the major impact to n_{VSDG} is with u_{DC}, cf. g, and significant impacts are with η_{ED1} and u_{uc}, cf. h. Finally, the fuel quantity is mostly affected by u_{DC}, cf. i, and minor impacts are on η_{ED1}, u_{uc}, and η_{ED2}, cf. j.

Based on the shown sensitivity analysis, the most influential factor to simulation results is with the DC-link voltage measurement of the energy management algorithm, i.e. Eqs. 2.46…2.52. Other influential sources of an error are η_{ED1}, u_{uc}, and η_{ED2}, which refer to the power measurement and efficiency mapping accuracies as well as to the accuracy of the UC

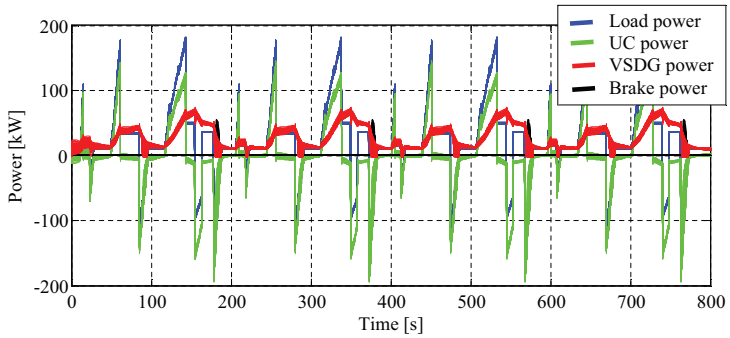

Figure 2.25. Illustration of the deviations in the power variables depending on an operation point of the powertrain with random changes in input parameters.

pack voltage measurement. Low importance to simulation results were noticed with variations of i_{uc} or $\eta_{\mathrm{DC/DC}}$

Therefore, the ranking of variables with given error limits beginning from the most important is: 1. u_{DC}, 2. η_{ED1} and u_{uc}, 3. η_{ED2}, and 4. i_{uc} and $\eta_{\mathrm{DC/DC}}$. This work could be continued by deleting variation in parameters of the group 4, and either lowering error limits of u_{DC} or assuming it to be known accurately. This could be done in order to study relevancies of the groups 2 and 3 more carefully. Furthermore, the look-up table of $\eta_{\mathrm{DC/DC}}$ could be replaced with a polynomial function, due to a minor importance of the error in $\eta_{\mathrm{DC/DC}}$.

The meaning for the high sensitivity of u_{DC} in the assessed control algorithm is such that there cannot be significant difference in the u_{DC} feedback between Eqs. 2.28, 2.46, and 2.50. Thus, according to this sensitivity analysis the AFE converter and ESS should be placed in the immediate proximity, and to the same feedback of u_{DC}.

Fig. 2.25 presents power variables of 100 simulation trials, and thus illustrates deviations in different operation points. The energy management scheme operates as planned, despite of all aforementioned variations in parameters. Mean standard deviations, in Tables 2.14…2.16, together with instantaneous power variables in Fig. 2.25 assert the robustness of this energy management scheme. It can be argued that the multi-stage approach with given time-domain simulation and sensitivity analysis are good manners for the series-hybrid powertrain design.

Fig. 2.25 shows that depending on the stochastic parameters the powertrain has some deviation in its operation. For instance, at decelerations to stop, the VSDG power either goes to zero or charges ESS. The VSDG power goes to zero, if regenerative power increases the DC-link voltage to

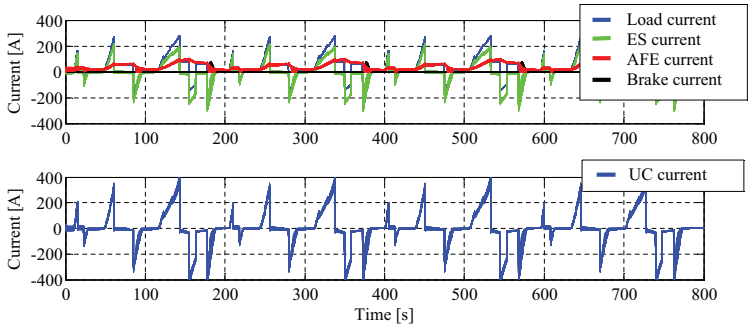

Figure 2.26. Illustration of the deviations in the current variables depending on an operation point of the powertrain with random changes in input parameters.

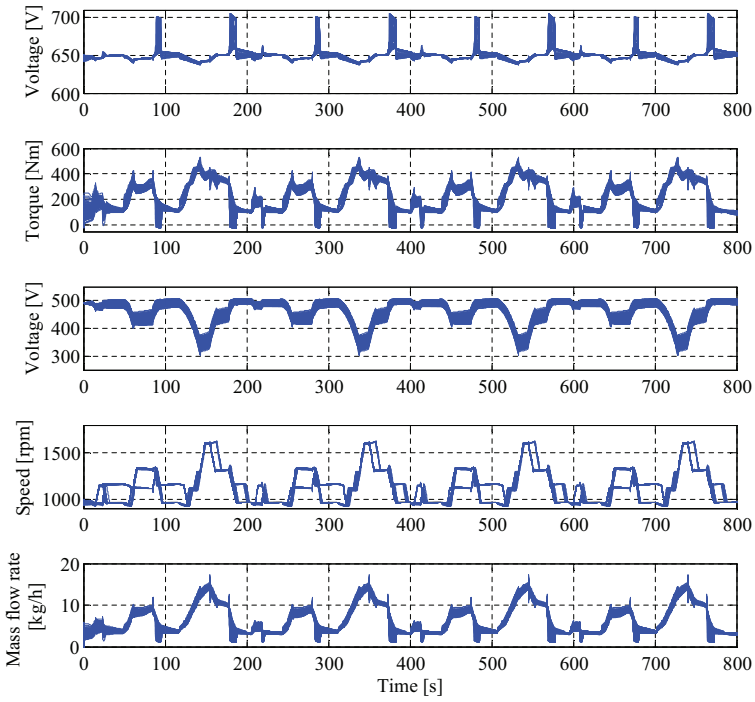

Figure 2.27. Illustration of the deviations in the miscellaneous variables depending on an operation point of the powertrain with random changes in input parameters. Variables beginning from the top: u_{DC}, τ_{load}, u_{uc}, n_{VSDG}, and $\dot{m}_{\mathrm{VSDG}}$.

the brake-unit limit, which is due to the full charge in ESS. Waveforms that refer to this kind of operation can be seen in Figs. 2.26 and 2.27.

Fig. 2.26 shows powertrain DC currents on the DC-link voltage potential and the UC current on the UC voltage potential.

Fig. 2.27 illustrates other variables. The DC-link voltage can be seen,

in some cases, to meet the braking voltage limit at 700 V. The load torque seems to be somewhat smooth, although there are 'spikes' at ends of accelerations and beginnings of decelerations. The UC voltage limits to the maximum value of 500 V, although the dispersion at the ends of accelerations becomes high, approximately 60 V. The speed-state changes of VSDG become somewhat non-deterministic due to variation of the VSDG power. The fuel consumption rate is alike to the load torque, although less dispersed.

It is worth noticing that almost all variation in modeled variables are within 3σ from the mean, i.e. the three-sigma rule [Sobol, 1975], which is remarkable absolute value in τ_{load}, u_{uc}, n_{VSDG}, and $\dot{m}_{\mathrm{VSDG}}$. This issue can be partly explained by the stepwise speed control of VSDG, which disperses the moments of the speed-state transitions of VSDG in the time domain. Naturally, this affects to instantaneous torque, speed, and fuel consumption.

3. Summary of Publications

This dissertation is divided into two parts. Publications I. . . VI discuss the design of series-hybrid powertrains with the proposed multi-stage modeling approach. Publication VII concentrates on the dynamic modeling of multiport DC-buses in power-electronic systems. The dynamic modeling is an essential part in the design of new controllers that belong to series-hybrid powertrains.

3.1 Publication I

Power bus control for series hybrid heavy-duty vehicles. *World Electric Vehicle J.*, 3(1), May 2009.

A hierarchy for a series-hybrid powertrain energy management is proposed. This hierarchy consists of reactive and predictive control methods from which the reactive methods are contributed in this dissertation.

In this hierarchy, the energy management is divided into three segments based on primary, secondary, and tertiary objectives. These objectives are prioritized in the same order. The idea is to augment the system control to the secondary and further to tertiary objectives if objectives with higher priorities are accomplished.

It was shown with simulations that the voltage control of the DC link, i.e. one of the reactive control methods, has to be on the device layer. In addition, the power system and strategic layers are proposed, which differ from each other by their reaction times. The strategic layer is suggested to consist of predictive control methods.

As results, it was concluded that a combination of the DC-bus voltage and load based reactive methods return the most regenerative energy for further use. The second best solution was the predictive control imple-

mented into five sub-cycles that are proposed to be controlled with applicable energy managements. Other control methods with less benefits were based either on load power or DC-bus voltage.

3.2 Publication II

Low-pass filtered power-flow control in series hybrid electric vehicle. In *Proc. 24th Elect. Veh. Symp.*, May 2009.

A model-based design of an energy management strategy is presented for the diesel-electric powertrain with the active UC buffering. The proposed energy management is validated in Publication III, reviewed structure presented in Section 2.1.11, and the error analysis is given in Section 2.3.

The indirect primary source power buffering method is investigated for the active UC buffered diesel series-hybrid powertrains. The background for low-level controls of the proposed energy management was on the existing hardware, the current controlled DC-DC converter and the voltage controlled active rectifier. The advantage of this EMS approach is on the incremental change from the diesel-electric powertrain, i.e., an electric powertrain with an active rectifier and low capacitance intermediate circuit.

The paper presented correctly directed simulation results for the powertrain operation with the ECE-15 driving cycle. The simulation study illustrated the VSDG decrease potential to be within 50...72 % of the original, while an ES system operates in a proper efficiency area. The decrease ratio depends on the drive cycle, and the sizing of the UC pack as well as the DC-DC converter. Furthermore, energy losses in the UC system with different configurations were derived.

Requirement for the UC pack energy was concluded to the range of 0.5...1.0 kWh with given vehicle specifications, i.e., the ECE-15 driving cycle with the vehicle weight of 10 t, and with the proposed energy management algorithms. As a comparison, Burke [2007] reported the 75...150-Wh energy storage to be reasonable for mild hybrid vehicles with weight of 1100...1600 kg.

The problematic nature of controlling power was noticed with this energy management algorithm during unacceptably high loads. This lead to the implementation of derations for the control algorithms, as described

in Eq. 2.16.

3.3 Publication III

Validation of quasi-static series hybrid electric vehicle simulation model. In *Proc. IEEE Veh. Power and Propulsion Conf.'10*, Sept. 2010.

The paper presents results of the validation experiments for the designed series-hybrid powertrain plant models. In addition, the focus is on the modeling and energy management of the UC buffered diesel-electric powertrain.

Information is gained on the accuracies and restrictions of the designed simulation models. The experiments illustrate that the designed energy management in Publication II operates as intended. Essential operation behaviors are highlighted with figures. According to simulations, it was reported that the proposed energy management interface enables all operation modes of a hybrid powertrain. Based on the information gained, precise descriptions of energy management algorithm interfaces have not been covered for all powertrain topology cases.

3.4 Publication IV

Analysis of the ultracapacitor module in power buffering. In *Proc. 4th European Symp. on Super Capacitors and Applicat.*, Oct. 2010.

This paper presents the experiments of two different power-buffering cases with the active control of an UC pack. The methods for the peak power cutting, as well as the method for the acceleration assistance and regenerative energy recuperation are described.

The paper also introduces efficiency maps of a single power conversion through a DC-DC converter, single power conversion through an UC pack, and ES system cycle efficiency through twice a DC-DC converter and twice an UC pack. Such efficiency maps are rare or cannot be found from the earlier literature. The variance of UC capacitance is presented as a map, which the newest articles present in less informative way, e.g., as Table data in few operation points like Burke and Miller [2011]. In this work, efficiency and fuel consumption maps are used for illustrations of the pro-

posed control algorithms.

The power control methods were applied to simulations of the diesel-electric powertrain with the active UC buffering. The simulations illustrate the operation areas and time-domain behaviors of the diesel engine and the ES system in these cases. Effects of the derations of the DC-DC converter control to the system operation were highlighted. Based on our understanding, this type of system-level assessments has not been presented before for this series-hybrid powertrain case.

3.5 Publication V

Feasibility study of fuel cell-hybrid powertrains in non-road mobile machineries. *Automation in Construction*, 35(1):296-305, Nov. 2013.

The article presents a mutual comparison of different powertrain topologies for a harbor straddle carrier. The comparison evaluates five of relevant fuel cell-hybrid topologies with different active and passive connections of a battery, UC or the both. Evaluated characteristics in the comparison are size, weight, cost, and efficiency.

The article also presents mathematical descriptions of plant models to improve the repeatability of similar work and illustrates power flows of different powertrain cases with figures. Section 2.1 further contributes to the improvement of the repeatability.

The attained knowledge of mutual differences between powertrain cases enables optimization of a duty vehicle powertrain for a specific purpose. For instance, a different topology optimizes a powertrain in respect to weight and size, than which optimizes a powertrain in respect to cost or efficiency. Furthermore, attained results can be generalized to give targets of hybridizations for other primary source options as well.

In the end, the choice of a powertrain depends on the valuation of different characteristics in powertrains.

3.6 Publication VI

Design of an energy management scheme for a series-hybrid powertrain. In *Proc. IEEE Transportation Electrification Conf. and Expo*, June 2012.

The paper presents dimensioning of a powertrain with time-domain simulations. The powertrain with the actively coupled FC, passive high-energy battery and active UC was chosen based on the comparison in Publication V. Also feasibilities of other topologies are discussed considering use of the high-energy and high-power batteries.

The dimensioning with time-domain simulations need energy management algorithms and dimensioning rules, which were described with the energetic macroscopic representation (EMR) technique [Chan et al., 2010] and mathematical descriptions. These together with plant models enable rapid selection of powertrain components. It was reported that this energy management maximizes use of the battery, UC, and FC-source.

As results, the design space for components of this powertrain is illustrated and feasible design areas with the different optimization targets such as size, weight, and cost are highlighted. The feasibility of the EMR technique with mathematical descriptions is noted and an improvement to the EMR technique is suggested.

3.7 Publication VII

Modeling of multiport DC busses in power-electronic systems. In *Proc. IEEE Int. Conf. on Ind. Tech.*, Feb. 2013.

Multiport DC buses are applied in emerging applications, such as industrial and household DC distribution systems, different vehicle applications, such as powertrains of electrified automotive systems, diesel-electric rail vehicles, heavy-duty and off-road vehicles, and more-electric aircraft. The risk of instability in a cascade-connected system consisting of a DC source, an *LC* filter, and a regulated load is well known.

This paper proposes a systematic dynamic modeling approach for multiport DC-buses in power-electronic systems. It is needed to predict the resonance behavior of the bus while design of controllers. This approach was validated up to resonance frequencies of the DC-bus capacitors. The model of the DC-bus can be applied in both time-domain simulations and small-signal analysis.

The small-signal stability of the system can be assessed, if the impedance of the DC-bus model is augmented with load admittances. This yields minor loop gains that can be used to evaluate the stability margins for the system in order to guarantee robust control. Besides the controller

design, this approach can be used to derive the maximum lengths of the DC-bus cabling, as well as the minimum values and distributions of the DC-bus capacitances.

4. Conclusions

This Chapter presents main results of this dissertation, evaluates the scientific importance of this work, and proposes directions for the work in the future.

4.1 Main Results

This dissertation merges different methodologies for development of series-hybrid powertrains to non-road mobile machineries. In sense of the system-level analysis, merging means application of powertrain component models in a suitable way, while concerning what will be the introduced accuracy of the particular approach. Due to practical reasons, such as the manageability and computing time, the powertrain design is separated to large and small-signal methods. The large signal method, termed as the multi-stage approach, is targeted to enable an analysis, dimensioning, and comparison of system-level designs. On the contrary, the small-signal approach is for the specific design of controllers of a system. Error analysis methods are demonstrated for the accuracy assessments of modeling analyses, as well as for solving accuracy requirements of input parameters.

This dissertation introduces the multi-stage modeling approach for the series-hybrid powertrain design. This approach is used in Publications I...VI. It differs from other simulators as ADVISOR or QSS by the need to model the low capacitance DC buses and current control loops. This is due to the development of UC to become an option for the peak power buffering, especially in the NRMM application field, which introduces these low-capacitance DC buses to vehicles. This leads to increased computation time of this approach with respect to ADVISOR and QSS, which often assume passive energy storages in DC buses.

Publication I compares different energy management strategies such as: DC-bus voltage control, load power control, peak power shaving control, combined voltage and load power control, and vehicle state predictive control in the diesel electric powertrain with active UC. The combined voltage and load power control that was developed in Publication II, gave promising results for the energy recuperation. Therefore, it was further assessed in Publications III. . . IV.

The introduced multi-stage modeling approach is used systematically for the design of the diesel-electric powertrain with the indirect power buffering by the active ultracapacitor in Publications II. . . IV, and the error analysis is given in Section 2.3. Based on the careful analyses, such a powertrain with the described energy management is viable. This energy management was validated in distinct test setups with one-tenth of full power.

Publication III presented comparisons of experiments to simulations that provided knowledge of achievable accuracies and restrictions of the multi-stage approach. These comparisons are the first or amongst the first, which can be found from the literature for the studied powertrain case. They highlight essential operation behaviors with figures that together with the presented accuracies are valuable for engineers and scientists working with the same or similar series-hybrid powertrain systems.

Publication V compared feasibilities of different fuel cell powertrains for an NRMM application with the help of the multi-stage modeling approach. As results, mutual relations of size, weight, cost, and efficiency of powertrains were obtained. This work is a basis for the choice between powertrain topologies. This application-specific choice depends on the valuation of different characteristics of the assessed topologies.

The most interesting powertrain case of the comparison in Publication V was chosen under further assessments in Publication VI. The chosen powertrain was the actively coupled fuel cell source with the passive HE battery and active UC. Dimensioning of this powertrain case with the proposed energy management and dimensioning rules was described with the help of the energetic macroscopic representation and mathematical descriptions. The design space for components of this powertrain case was introduced and feasible design areas with the different optimization targets such as size, weight, and cost were highlighted. This assessment is needed for a rapid selection of powertrain components.

Small-signal methods come into question when the specific controller

design needs to be done. Therefore, Publication VII introduces a systematic approach for the dynamic modeling of multiport DC-buses in power-electronic systems. This work enables designs of load and source converter controllers. In addition, this approach can be used to derive the maximum lengths of the DC-bus cabling, as well as the minimum values and distributions of the DC-bus capacitances.

This dissertation has a momentum to the development of different series-hybrid powertrains to NRMMs. It is valuable for practicing powertrain engineers, scholars, and students. This work has been ongoing during increasing interest of the NRMM industry to hybridize powertrains.

4.2 Scientific Importance of Author's Work

This dissertation contributes to a topical subject, i.e., methodologies for development of series-hybrid powertrains to non-road mobile machineries. The hybridization of NRMM powertrains lags around ten years with respect to the hybridization of passenger vehicles that has been ongoing since the 1990's.

The main scientific importance of this dissertation is on the management of the complex entity, i.e., the design of complete series-hybrid powertrains. Implementation of new designs require design principles that, generally, do not exist. The degrees of freedom in series-hybrid powertrain design arise because of several energy storage options and their combinations, the sizing of energy sources and storages, the energy source and storage interface options, e.g. active or passive, and the control of active interfaces. Thus, feasibilities, design procedures and tools need to be thoroughly researched.

This dissertation introduces concepts, approaches, and algorithms, which have been missing from the modern literature.

For instance, concepts such as different options in series-hybrid powertrain design have not been extensively compared. Such comparisons are contributed in this dissertation in various levels as comparing algorithms, full topologies, and choices within one topology. Furthermore, promising concepts are contributed towards viable powertrain cases, as the diesel-electric powertrain with the indirect power buffering by the active UC, and the actively coupled fuel cell source with the passive battery and active UC.

Completion of, e.g., comparisons between topologies to mutual relations

with concrete characteristics as size, weight, and cost give essential knowledge to decision-makers for investments. Knowledge of performing comparisons and their results are usually not publicly available, to which problems this dissertation responses.

This dissertation introduces different modeling approaches such as the multi-stage approach for the large-signal modeling, and the dynamic modeling approach for multiport DC-buses in power-electronic systems, which is a small-signal modeling method. These together form an approach to the complete design of controllers in different series-hybrid powertrain systems. Both approaches are targeting to controller designs from different perspectives.

The multi-stage modeling approach makes a compromise between the fidelity of the system model with respect to manageability and computing time. The target of this approach is on the 20-Hz bandwidth. It enables the analysis, dimensioning, and comparison of system-level designs. Contributions have been made to evaluate accuracies, restrictions, and parameter sensitivities of this approach.

The dynamic modeling approach for multiport DC-buses in power-electronic systems have been validated up to the resonance frequency of the DC-bus capacitors. This approach can be augmented with load models in order to predict operation of power-electronic systems up to around switching frequencies, i.e., from one to tens of kilohertz. This systematical approach enables the specific controller design for these systems.

Both of these approaches are needed by practicing powertrain engineers, scholars, and students.

This dissertation demonstrates maximum error and sensitivity analysis methods to assess errors in modeling analyses. The maximum error analysis bases on partial differentiation of equations of the system model. The sensitivity analysis bases on the Monte-Carlo method that is used to apply randomness to input parameters of the system model. Both approaches are valuable for scientists and engineers. The sensitivity analysis can be used as a systematic tool to solve impacts of input parameter variations to output parameters, and thereby to solve requirements for input parameters in order to achieve demands of output parameters.

Series-hybrid powertrains need energy management algorithms if active controls of sources are used. A comparison of different powertrain cases is depended on energy management algorithms that should be rigorously described in order to achieve comprehensive comparisons. This

dissertation contributes such work for the promising powertrain cases due to the lack of exact energy management descriptions in the modern literature.

4.3 Proposals for Future Work

The multi-stage and dynamic modeling approaches should be used hand in hand in order to introduce and optimize feasible series-hybrid powertrain concepts for non-road mobile machineries, and to other vehicle applications. This kind of work needs still extensive contributions.

Contributions could be made for different vehicle cases with different series-hybrid powertrains, energy management strategies and algorithms. Promising options should be contributed towards viable choices for implementation, and then tested extensively following the reported conclusions. The work like this leads to knowledge of characteristics between topologies in a real application.

For instance, dynamics of power-electronic systems with multiple loads and sources acting simultaneously should be modeled, analyzed, and experimented. The foundation for that work is given in Publication VII, which validates the multiport DC-bus model of power-electronic systems.

The sensitivity analysis with Monte Carlo simulations should be continued for the diesel-electric powertrain with the indirect power buffering by the active UC. These assessments could continue by deleting or lowering error limits in certain stochastic parameters. This systematic work leads to the knowledge of requirements in accuracies in those parameters.

In the multi-stage modeling comparisons to experiments, more information is achieved, if i_{ES} is compared instead of i_{es}. This includes the accuracy of the DC-DC converter plant model into the comparison.

The indirect power buffering for the diesel-electric powertrain should be implemented to the full powertrain test setup and evaluated with full power.

Feasibilities of the reactive control methods in different actions of NRMM should be evaluated in order to avoid the complexity of design an energy management with several modes. For example, suitable reactive control methods for each action of a straddle carrier as described in Publication I should be clearly defined.

The evaluation of the proper sizing of UC and VSDG in the powertrain with the indirect power buffering with different EMS should be continued.

Further evaluations could be made in a similar way as Publication VI assesses the sizing of a powertrain. In Publication IV, different EMSs are evaluated. However, their impacts to the sizing, if small transients of the primary source are favorable, and if sizes of UC and VSDG would be freely chosen, were not considered.

Error analyses could be continued by inclusion of errors due to an engine model to the error analysis of static states. Furthermore, the error analysis of static states could be complemented by error analyses of transient states.

Bibliography

Åhman, M. (2001). Primary energy efficiency of alternative powertrains in vehicles. *J. Energy*, 26(11):973–989.

Baalbergen, F., Bauer, P., and Ferreira, J. A. (2009). Energy storage and power management for typical 4Q-load. *IEEE Trans. Ind. Electron.*, 56(5):1485–1498.

Bernard, J., Delprat, S., Büchi, F. N., and Guerra, T. M. (2009). Fuel-cell hybrid powertrain: toward minimization of hydrogen consumption. *IEEE Trans. Veh. Technol.*, 58(7):3168–3176.

Bogosyan, S., Gokasan, M., and Goering, D. J. (2007). A novel validation and estimation approach for hybrid serial electric vehicles. *IEEE Trans. Veh. Technol.*, 56(4):1485–1497.

Brenneisen, J., Futterlieb, E., Muller, E., and Schulz, M. (1973). A new converter drive system for a diesel electric locomotive with asynchronous traction motors. *IEEE Trans. Ind. Appl.*, IA-9(4):482–491.

Broy, M., Krüger, I. H., Pretschner, A., and Salzmann, C. (2007). Engineering automotive software. *Proc. IEEE*, 95(2):356–373.

Buller, S. (2003). *Impedance-based simulation models for energy storage devices in advanced automotive power systems*. PhD thesis, Institute for Power Electronics and Electrical Drives, Aachen, Germany. url: http://www.isea.rwth-aachen.de/dissertations/en.

Burke, A. and Miller, M. (2011). The power capability of ultracapacitors and lithium batteries for electric and hybrid vehicle applications. *J. Power Sources*, 196(1):514–522.

Burke, A. F. (2007). Batteries and ultracapacitors for electric, hybrid, and fuel cell vehicles. *Proc. IEEE*, 95(4):806–820.

Camara, M. B., Gualous, H., Gustin, F., and Berthon, A. (2008). Design and new control of DC/DC converters to share energy between supercapacitors and batteries in hybrid vehicles. *IEEE Trans. Veh. Technol.*, 57(5):2721–2735.

Camara, M. B., Gualous, H., Gustin, F., Berthon, A., and Dakyo, B. (2010). DC/DC converter design for supercapacitor and battery power management in hybrid vehicle applications–polynomial control strategy. *IEEE Trans. Ind. Electron.*, 57(2):587–597.

Ceraolo, M., di Donato, A., and Franceschi, G. (2008). A general approach to energy optimization of hybrid electric vehicles. *IEEE Trans. Veh. Technol.*, 57(3):1433–1441.

Chan, C. C. (2007). The state of the art of electric, hybrid, and fuel cell vehicles. *Proc. IEEE*, 95(4):704–718.

Chan, C. C., Bouscayrol, A., and Chen, K. (2010). Electric, hybrid, and fuel-cell vehicles: architectures and modeling. *IEEE Trans. Veh. Technol.*, 59(2):589–598.

Chen, M. and Rincón-Mora, G. A. (2006). Accurate electrical battery model capable of predicting runtime and *I-V* performance. *IEEE Trans. Energy Convers.*, 21(2):504–511.

Cook, B. (2002). Introduction to fuel cells and hydrogen technology. *Eng. Sci. Educ. J.*, 11(6):205–216.

Dimov, I. and Georgieva, R. (2010). Monte Carlo algorithms for evaluating Sobol' sensitivity indices. *J. Int. Assoc. Math. Comput. Simulation*, 81:271–280.

Dimov, I. T. and McKee, D. (2007). *Monte Carlo Methods for Applied Scientists*. World Scientific, River Edge, NJ.

Dong, T. K., Kirchev, A., Mattera, F., Kowal, J., and Bultel, Y. (2011). Dynamic modeling of Li-ion batteries using an equivalent electrical circuit. *J. Electrochem. Soc.*, 158(3):A326–A336.

Ehsani, M., Gao, Y., Gay, S. E., and Emadi, A. (2005). *Modern Electric, Hybrid Electric, and Fuel Cell Vehicles*. CRC Press, Boca Raton, FL, 1st edition.

Ehsani, M., Gao, Y., and Miller, J. M. (2007). Hybrid electric vehicles: architecture and motor drives. *Proc. IEEE*, 95(4):719–728.

Einhorn, M., Conte, F. V., Kral, C., and Fleig, J. (2013). Comparison, selection, and parameterization of electrical battery models for automotive applications. *IEEE Trans. Power Electron.*, 28(3):1429–1437.

Emadi, A., Rajashekara, K., Williamson, S. S., and Lukic, S. M. (2005). Topological overview of hybrid electric and fuel cell vehicular power system architectures and configurations. *IEEE Trans. Veh. Technol.*, 54(3):763–770.

Feroldi, D., Serra, M., and Riera, J. (2009). Design and analysis of fuel-cell hybrid systems oriented to automotive applications. *IEEE Trans. Veh. Technol.*, 58(9):4720–4729.

Gao, D. W., Mi, C., and Emadi, A. (2007). Modeling and simulation of electric and hybrid vehicles. *Proc. IEEE*, 95(4):729–745.

Gao, W. (2005). Performance comparison of a fuel cell-battery hybrid powertrain and a fuel cell-ultracapacitor hybrid powertrain. *IEEE Trans. Veh. Technol.*, 54(3):846–855.

Gao, Y. and Ehsani, M. (2006). Parametric design of the traction motor and energy storage for series hybrid off-road and military vehicles. *IEEE Trans. Power Electron.*, 21(3):749–755.

Gauchia, L. and Sanz, J. (2010). A per-unit hardware-in-the-loop simulation of a fuel cell/battery hybrid energy system. *IEEE Trans. Ind. Electron.*, 57(4):1186–1194.

Grbovic, P. J., Delarue, P., Moigne, P. L., and Bartholomeus, P. (2011). The ultracapacitor-based controlled electric drives with braking and ride-through capability: overview and analysis. *IEEE Trans. Ind. Electron.*, 58(3):925–936.

Greenwell, W. and Vahidi, A. (2005). Predictive control of voltage and current in a fuel cell-ultracapacitor hybrid. *IEEE Trans. Ind. Electron.*, 54(3):846–855.

Guarnieri, M. (2011a). When cars went electric, part 1. *IEEE Ind. Electron. Mag.*, 5(1):61–62.

Guarnieri, M. (2011b). When cars went electric, part 2. *IEEE Ind. Electron. Mag.*, 5(2):46–53.

Guzzella, L. and Sciarretta, A. (2007). *Vehicle Propulsion Systems, Introduction to Modeling and Optimization*. Springer-Verlag, Berlin Heidelberg, Germany, 2nd edition.

Harnefors, L. and Nee, H.-P. (1998). Model-based current control of AC machines using the internal model control method. *IEEE Trans. Ind. Appl.*, 34(1):133–141.

Harvey, H. F. and Thau, W. E. (1925). Electric propulsion of ships. *Trans. Amer. Inst. Elect. Eng.*, XLIV:497–522.

Hentunen, A., Suomela, J., Leivo, A., Liukkonen, M., and Sainio, P. (2010). Full-scale hardware-in-the-loop verification environment for heavy-duty hybrid electric vehicles. *World Elect. Veh. J.*, 4:119–127.

Hinkkanen, M., Harnefors, L., and Luomi, J. (2007). Control of induction motor drives equipped with small DC-link capacitance. In *Proc. EPE'07*, Aalborg, Denmark. CD-ROM.

Katrašnik, T., Trenc, F., and Oprešnik, S. R. (2007). Analysis of energy conversion efficiency in parallel and series hybrid powertrains. *IEEE Trans. Veh. Technol.*, 56(6):3649–3659.

Kim, S.-M. and Sul, S.-K. (2006). Control of rubber tyred gantry crane with energy storage based on supercapacitor bank. *IEEE Trans. Power Electron.*, 21(5):1420–1427.

Kusko, A. (1968). Off-highway vehicles. *Proc. IEEE*, 56(4):600–604.

Lai, J.-S. and Nelson, D. J. (2007). Energy management power converters in hybrid electric and fuel cell vehicles. *Proc. IEEE*, 95(4):766–777.

Lajnef, W., Vinassa, J.-M., Briat, O., Azzopardi, S., and Woirgard, E. (2007). Characterization methods and modelling of ultracapacitors for use as peak power sources. *J. Power Sources*, 168(2):553–560.

Lidozzi, A. and Crescimbini, F. (2012). Adaptive direct-tuning control for variable-speed diesel-electric generating units. *IEEE Trans. Ind. Electron.*, 59(5):2126–2134.

Lidozzi, A., Solero, L., and Napoli, A. D. (2010). Ultracapacitors equipped hybrid electric microcar. *IET Elect. Power Applicat.*, 4(8):618–628.

Lin, W. S. and Zheng, C. H. (2011). Energy management of a fuel cell/ultracapacitor hybrid power system using an adaptive optimal-control method. *J. Power Sources*, 196(6):3280–3289.

Liutanakul, P., Awan, A.-B., Pierfederici, S., Nahid-Mobarakeh, B., and Meibody-Tabar, F. (2010). Linear stabilization of a dc bus supplying a constant power load: a general design approach. *IEEE Trans. Power Electron.*, 25(2):475–488.

Maksimović, D. (2000). Computer-aided small-signal analysis based on impulse response of dc/dc switching power converters. *IEEE Trans. Power Electron.*, 15(6):1183–1191.

Markel, T., Brooker, A., Hendricks, T., Johnson, V., Kelly, K., Kramer, B., O'Keefe, M., Sprik, S., and Wipke, K. (2002). ADVISOR: a systems analysis tool for advanced vehicle modeling. *J. Power Sources*, 110(2):255–266.

Mathworks (2013). Matlab simulink^{TM} help. Online. url: http://www.mathworks.com/help/toolbox/physmod/powersys/ (Last accessed on 26th of Sept. 2013).

Metropolis, N. and Ulam, S. (1949). The Monte Carlo method. *J. Amer. Statistical Assoc.*, 44(247):335–341.

Miller, A. R., Peters, J., Smith, B. E., and Velev, O. A. (2006). Analysis of fuel cell hybrid locomotives. *J. Power Sources*, 157(2):855–861.

Mooney, C. Z. (1997). *Monte Carlo Simulation*. SAGE Publications Inc., Thousand Oaks, CA.

Moreno, J., Ortúzar, M. E., and Dixon, J. W. (2006). Energy-management system for a hybrid electric vehicle using ultracapacitors and neural networks. *IEEE Trans. Ind. Electron.*, 53(2):614–623.

Mosskull, H., Galić, J., and Wahlberg, B. (2007). Stabilization of induction motor drives with poorly damped input filters. *IEEE Trans. Ind. Electron.*, 54(5):2724–2734.

Oh, S. C. (2005). Evaluation of motor characteristics for hybrid electric vehicles using the hardware-in-the-loop concept. *IEEE Trans. Veh. Technol.*, 54(3):817–824.

Pietiläinen, K., Harnefors, L., Petersson, A., and Nee, H.-P. (2006). DC-link stabilization and voltage sag ride-through of inverter drives. *IEEE Trans. Ind. Electron.*, 53(4):1261–1268.

Powell, B. K., Bailey, K. E., and Cikanek, S. R. (1998). Dynamic modeling and control of hybrid electric vehicle powertrain systems. *IEEE Control Syst. Mag.*, 18(5):17–33.

Puukko, J., Messo, T., Nousiainen, L., Huusari, J., and Suntio, T. (2011). Negative output impedance in three-phase grid-connected renewable energy source inverters based on reduced-order model. In *Proc. IET RPG'11*, Edinburgh, UK.

Rajashekara, K. (1994). History of electric vehicles in general motors. *IEEE Trans. Ind. Appl.*, 30(4):897–904.

Shepherd, C. M. (1965). Design of primary and secondary cells: II. An equation describing battery discharge. *J. Electrochem. Soc.*, 112(7):657–664.

Shi, L. and Crow, M. L. (2008). Comparison of ultracapacitor electric circuit models. In *Proc. IEEE Power and Energy Soc. General Meeting–Conversion and Delivery of Elect. Energy 21st Century*, Pittsburgh, PA.

Shibuya, H. and Kondo, K. (2011). Designing methods of capacitance and control system for a diesel engine and EDLC hybrid powered railway traction system. *IEEE Trans. Ind. Electron.*, 58(9):4232–4240.

Sobol, I. M. (1975). *The Monte Carlo Method*. Mir Publishers, Moscow, Russia, 2 edition.

Sobol, I. M. (2001). Global sensitivity indices for nonlinear mathematical models and their Monte Carlo estimates. *J. Int. Assoc. Math. Comput. Simulation*, 55(1-3):271–280.

Stark, N. (2007). Diesel hybrid rubber-tired gantry crane in service in Canada. Press release. url: http://www.greencarcongress.com/2007/06/diesel_hybrid_r.html (Last accessed on 26th of Sept. 2013).

Sudhoff, S. D., Corzine, K. A., Glover, S. F., Hegner, H. J., and Robey, Jr., H. N. (1998). DC link stabilized field oriented control of electric propulsion systems. *IEEE Trans. Energy Convers.*, 13(1):27–33.

Syed, F. U., Kuang, M. L., Czubay, J., and Ying, H. (2006). Derivation and experimental validation of a power-split hybrid electric vehicle model. *IEEE Trans. Veh. Technol.*, 55(6):1731–1747.

Teago, F. J. (1937). Electric traction. *J. Inst. Elect. Eng.*, 80(482):181–189.

Thounthong, P. and Raël, S. (2009). The benefits of hybridization. *IEEE Ind. Electron. Mag.*, 3(3):25–37.

Tremblay, O., Dessaint, L. A., and Dekkiche, A. I. (2007). A generic battery model for the dynamic simulation of hybrid electric vehicles. In *Proc. IEEE Veh. Power and Propulsion Conf.'07*, pages 284–289, Arlington, TX.

Trummel, M. C. (1983). Development history of the hybrid test vehicle. *IEEE Trans. Veh. Technol.*, VT-32(1):7–14.

Tsai, S.-C. and Goyal, M. R. (1986). Dynamic turbocharged diesel engine model for control analysis and design. Technical Report 860455, Society of Automotive Engineers. doi:10.4271/860455.

v. Helmolt, R. and Eberle, U. (2007). Fuel cell vehicles: status 2007. *J. Power Sources*, 165(2):833–843.

v. Walwijk, M. (2009). Hybrid and electric vehicles—the electric drive establishes a market foothold—progress towards sustainable transportation. Technical Report Annual report 2008, International Energy Agency, Hybrid & electric vehicle implementing agreement, Angers, France.

Wakefield, E. H. (1994). *History of the Electric Automobile: Battery-Only Powered Cars*. Society of Automotive Engineers, Warrandale, PA.

Wallmark, O., Lundberg, S., and Bongiorno, M. (2012). Input admittance expressions for field-oriented controlled salient PMSM drives. *IEEE Trans. Power Electron.*, 27(3):1514–1520.

Wang, L. and Li, H. (2010). Maximum fuel economy-oriented power management design for a fuel cell vehicle using battery and ultracapacitor. *IEEE Trans. Ind. Appl.*, 46(3):1011–1020.

Weiser, E. F. (1947). Braking resistors and control for diesel-electric locomotives. *Trans. Amer. Inst. Elect. Eng.*, 66(1):229–232.

Woonki, N., Taesik, P., Taehyung, K., and Sangshin, K. (2011). Light fuel-cell hybrid electric vehicles based on predictive controllers. *IEEE Trans. Veh. Technol.*, 60(1):89–97.

Yu, Z., Zinger, D., and Bose, A. (2011). An innovative optimal power allocation strategy for fuel cell, battery and supercapacitor hybrid electric vehicle. *J. Power Sources*, 196(4):2351–2359.

Zandi, M., Payman, A., Martin, J.-P., Pierfederici, S., Davat, B., and Meibody-Tabar, F. (2011). Energy management of a fuel cell/supercapacitor/battery power source for electric vehicular applications. *IEEE Trans. Veh. Technol.*, 60(2):433–443.

Zhang, X., Mi, C. C., Masrur, A., and Daniszewski, D. (2008). Wavelet-transform-based power management of hybrid vehicles with multiple on-board energy sources including fuel cell, battery and ultracapacitor. *J. Power Sources*, 185(2):1533–1543.

Zubieta, L. and Bonert, R. (2000). Characterization of double-layer capacitors for power electronics applications. *IEEE Trans. Ind. Appl.*, 36(1):199–205.

Errata

In Publication II:

In Figs. 4 and 6 the y-axis should be:

$$u_{\mathrm{ratio}} = \frac{u_{\mathrm{es}}}{u_{\mathrm{DC}}}.$$

Fig. 7 proposes the DC-DC converter current direction D to be chosen by incorrect way. The correct algorithm structure of Figs. 7 and 8 is given in Section 2.1.11 and used in Publication III.

Hybridization of a powertrain is a conceivable action for non-road mobile machineries (NRMMs) in order to reduce their emissions and energy consumption. NRMMs are a diverse group of vehicles that includes working machinery and equipment in several sectors such as construction, agriculture, forestry, as well as rail and inland waterways transport. This group excludes road vehicles primarily intended for the use of passenger- or goods transport. Computational methodologies ease development and optimization of new powertrains to which this dissertation particularly offers methodologies for development of different topologies of series-hybrid powertrains. The content of this dissertation is relevant due to the interest to electrify powertrains, and it is beneficial for researchers, engineers, as well as for students.

Aalto-DD 157/2013

ISBN 978-952-60-5366-0
ISBN 978-952-60-5365-3 (pdf)
ISSN-L 1799-4934
ISSN 1799-4934
ISSN 1799-4942 (pdf)

Aalto University
School of Electrical Engineering
Department of Electrical Engineering
www.aalto.fi